5-2019

Optical Enhancement in Periodic Plasmonic Gratings for SERS and Metal-Semiconductor-Metal Photodetectors (MSM-PDs) Applications

Ahmad Aziz Darweesh
University of Arkansas, Fayetteville

Optical Enhancement in Periodic Plasmonic Gratings for SERS and Metal-Semiconductor-Metal Photodetectors (MSM-PDs) Applications

A dissertation submitted in partial fulfillment
of the requirements for the degree of
Doctor of Philosophy in Microelectronics-Photonics

by

Ahmad Aziz Darweesh
Al-Mustansiriyah University
Bachelor of Science in Physics, 1999
Al-Mustansiriyah University
Master of Science in Physics, 2001

May 2019
University of Arkansas

This dissertation is approved for recommendation to the Graduate Council.

Joseph B. Herzog, Ph.D.
Dissertation Director

Hameed A. Naseem, Ph.D.
Committee Member

Jingyi Chen, Ph.D.
Committee Member

Rick Wise, Ph.D.
Committee Member

The following signatories attest that all software used in this thesis was legally licensed for use by Ahmad Darweesh for research purposes and publication.

_____	_____
Mr. Ahmad A. Darweesh, Student	Dr. Joseph B. Herzog, Dissertation Director

This dissertation was submitted to http://www.turnitin.com for plagiarism review by the TurnItIn company's software. The signatories have examined the report on this dissertation that was returned by TurnItIn and attest that, in their opinion, the items highlighted by the software are incidental to common usage and are not plagiarized material.

_____	_____
Dr. Rick Wise, Program Director	Dr. Joseph B. Herzog, Dissertation Director

ABSTRACT

This dissertation is aimed to numerically study the effect of plasmonic grating electrodes on the efficiency of metal-semiconductor-metal photodetectors (MSM PDs) and the sensitivity of Surface Enhanced Raman Spectroscopy (SERS). This research can benefit many areas of nanoscience and optics, including plasmonic applications, such as, super lenses, nano-scale optical circuits, optical filters, surface plasmon enhanced photo-detectors solar cells, imaging sensors, charge-coupled devices (CCD), and optical-fiber communication systems. Several parameters, wire widths and thickness, gap space, taper angle, and the incident wavelength and angle, were investigated. The goal of this research is to utilize the plasmonic phenomenon by using plasmonic gratings to develop and improve detectivity of metal-semiconductor-metal photodetectors (MSM-PDs) and sensitivity of SERS.

The dissertation includes the study of the substrate type – SiO_2 and SiO_2/Si for SERS applications, and GaAs substrates for MSM PDs – on the optical enhancement. In addition, the impact of the period of the nanograting, single and dual-width structures, is examined as well. Then, a comparison is conducted between these types to determine the optimum periods. The results show that dual-width structures can improve the incident light two times more than the single-width structures.

The work also introduces a new method, which incorporates the current density of the device when calculating the overall current enhancement in order to model real performance more accurately. Using this method indicates that since plasmonic hot spots align well with areas of large current density, the optical enhancement can play an even larger role in total current improvement.

The impact of taper angles, positive and negative, is also studied in detail. The results

suggest significant optical enhancements can be achieved by using tapered nanoslits instead of vertical sidewall structures. Finally, the effect of the incident wave angle on the enhancements is considered as well. Interestingly, the results show a significant role that incident wave angle can play on both the incident light enhancements.

ACKNOWLEDGMENTS

The first thing I would say is all praises and thanks are due to “Alláh”, the Lord of all that exists.

I would like to show my gratitude to my advisor, Dr. Joseph B. Herzog, for providing me the chance to work in his group. Without his patience and support, it would not be possible for me to accomplish my goal. I have learned a lot from him, not only knowledge but also good manners.

I feel very lucky that I worked in such a nice group where everyone was so helpful. I have learned a lot from them. They were very nice researchers as well as nice friends. Especially, I would like to thank Dr. Stephen J. Bauman, who helped me a lot to improve my writing skills and using lab equipment. A special thank goes out to Dr. Desalegn T. Debu, Zachary Brawley and Dr. David A. French for their constructive comments and collaborative efforts on research and publications that have helped me to go in the right direction of my research.

I would like to thank my mother who did not stop praying for me in every single day and night. I want to show my gratitude and thanks to my wife, soulmate, and close friend, “Balsam” for her continuous support in every aspect of my life. She was my best friend during the six years here in the United States. A special thanks goes out to my family in Iraq, my brothers and sister who provided me full support to be a good person. I never forget to thank my parents-in-law, sister and brother-in-law for their inspirational support to study aboard. A special thanks goes to my best friend Riyadh Hakami, who always supported me through my journey here in the United States.

I am always thankful to my friends at Al-Nahrain and Al-Mustansiriyah Universities in Baghdad, especially Abdul-Jabbar Alfayadh, Dr. Bashar Hamad, Dr. Bilal Jasim, Dr. Ahmed

Aziz, Dr. Rafid Abbas and Amer Abdullh Alshekly for their support.

Finally, I want to express my gratitude to Dr. Rick Wise, Renee Jones-Hearon, committee members, and the other μEP program members and colleagues, Physics department, and the Graduate School at the University of Arkansas, Fayetteville, USA for helping me to achieve my goals.

DEDICATION

This dissertation is dedicated to all of my family members, loved ones, and friends, especially my mother, father (May God have mercy on him), and wife. Without their prayers and support, I would not finish this work.

"Read! In the name of your lord, who has created; has created man from a clot. Read! And your lord is the most generous, who has taught by the pen; has taught man that which he knew not."

– Quran, 96:1-5

TABLE OF CONTENTS

LIST OF FIGURES

Chapter 1.

INTRODUCTION

1.1 Motivation

Pollution (soil, water, and air) is one of the main problems that causes death and lethal diseases; it is a prime problem that threatens the environment. There are many sources of pollution, some of which are power plants, factories, nuclear waste, and chemical waste. Pollution must be detected before it can be treated. Pollutants can be detected by devices that integrate photodetectors. For example, laser photodetectors which operate in the ultraviolet (UV) range can detect solid particulates in air and water. In addition, they can detect some pollutants, such as sulfur dioxide and nitrous oxide. Therefore, enhancing and improving these devices can help rescue the inevitable destruction of the environment and planet.

On the other hand, photodetectors which operate in the IR region are used in fiber-optic communication systems. These types of photodetectors do not require a high sensitivity because the laser provides a huge level of light intensity to the fiber; however, they require a high response. Moreover, photodetectors, which are sensitive to IR, are used for home security systems. They are used to detect the absence or presence of an object.[1,2] For example, photodetectors, which operate in visible and ultraviolet regions are used for safety and monitoring in factories. To illustrate, they are used to give feedback for robotic systems and examine the proper place of work pieces. Furthermore, near-IR photodetectors can be implemented in important military applications including night vision and target acquisition.[3,4] In addition, focusing on this type of device can open the door for different applications such as biomedical imaging and cognitive neuroscience research. [5-6] Astronomy is another field that

considers photodetectors as important devices. The types of photodetectors which operate in this field range from the far-IR to cosmic rays.

Another global problem is the detection of explosives and improvised explosive devices (IEDs). Recently, this problem has increased in many countries. For example, many car bombs are exploded in different places every day. The same problem threatens airports, metros, train stations, and public places. The devices that are used to detect explosives are very expensive and limited. Thus, developing and integrating photodetectors into the technology of these devices can make them cheaper and can diminish the number of victims.

Another problem that concerns the world is squandered energy (electrical and thermal). Squandering energy in many buildings and facilities, such as houses, factories, markets, and streets is a major problem. The squandered energy problem must be reduced to save this planet. Photodetectors can play a main role to minimize this problem; they can be used to control buildings. For example, photodetectors can control the flow of water, electricity, and heat in houses. One can reduce squandering energy by making photodetectors affordable. Thus, developing the metal-semiconductor-metal photodetectors can benefit the devices that integrate photodetectors.

This dissertation work can benefit many areas of nanoscience and nano-optics, including plasmon applications, such as light absorption, scattering, and optical detection devices,[7–13] Surface Enhanced Raman Spectroscopy (SERS),[14–19] super lenses,[20–23] single molecule detection,[19,24–26] optical filters, and surface plasmon polariton enhanced photo-detectors.[27–29] In addition, it can serve several applications such as radiation detection (solar cells, photovoltaics, and photo-diodes),[30–34] imaging sensors,[35–38] biosensing,[39–43] and optical-fiber communication systems.[44–47] This dissertation is aimed to numerically study the effect of plasmonic grating

electrodes and surrounding media on the performance of metal-semiconductor-metal photodetectors (MSM PDs). Several parameters, which can affect the MSM-PD efficiency were investigated. These parameters are wire widths, gap space, wire thickness, incident wavelength, incident wave angle, substrate type, and taper angle of the nanostructures. Only gold metal was used as electrodes in the entire dissertation work. Moreover, the effect of titanium, as an adhesive layer, on the plasmonic enhancements was studied as well.

1.2 Dissertation outline

This dissertation consists of several chapters that guide the reader to understand the steps of the conducted research. Starting from Chapter 1, it includes the motivation of this research and the outline of the dissertation. Chapter 2 discusses the general background of some scientific concepts that are related to the research and used to understand the physics and the engineering behind the photo-detection devices, such as the interaction of light with materials, optical response and surface plasmon polaritons. This chapter includes the techniques of the surface plasmon excitation and transmission enhancements. In addition, this chapter covers the different types of photodetectors and the fabrication steps. Chapter 3 discusses the computational electromagnetic simulation models in the COMSOL Multiphysics software package that are used to design and engineer the device. These models contain two types: Electromagnetic Wave, Frequency Domain (EWFD) and AC/DC Electric current. The first module is used to calculate the optical enhancement of the device, such as near enhanced electric field, absorption, transmission, and reflection; whereas, the second module is used to determine the current density enhancement of the device. The chapter also explains the main steps of building a simulation model. Chapter 4 discusses the optical enhancement results of plasmonic nanograting on SiO_2,

$Ti/SiO_2/Si$ and GaAs substrates. The results include the effect of the nanostructure sizes, shape and surrounding media. Chapter 5 discusses the electrical enhancement, particularly the current density enhancement of the device; it contains the study of the electrode shape effect on the results. Chapter 6 discusses the conclusions of the research and the proposed and future work. The appendices provide Microsoft Project for Ph.D. MicroEP degree plan and all the published, submitted and planned papers.

Chapter 2.

BACKGROUND

Electromagnetic waves can interact with different materials, such as conductors and semiconductors, due to the electrons in a valence band. The strength of the interaction depends on the electromagnetic wavelength and dimensions of material. The interaction can increase when the dimension decreases and vice versa. Thus, the optical properties of materials can be changed by changing the dimensions.

When an electromagnetic wave is incident on a piece of metal, it will cause an oscillation of free electrons. This oscillation of the free electrons is quantized, and the quantization of plasma oscillation is called a plasmon. The oscillations of electrons can generate new waves, which are called surface plasmon polaritons (SPPs), which are electromagnetic waves that decay evanescently and perpendicularly to the interface into the metal and the dielectric. These waves can couple with the incident electromagnetic waves and generate a new electromagnetic field, which is called a local field. The local field can play a prime role in enhancing the incident electric field; thus, optical enhancement can be gained. This phenomenon can be harnessed in several applications such as photodetectors, bio-sensing, and Surface Enhanced Raman Spectroscopy (SERS).

2.1 Interaction of light with materials

Light (electromagnetic wave) is a wave that consists of two fields, electric and magnetic, which propagate perpendicularly to each other and both of which are perpendicular to the direction of the electromagnetic wave. Electric charges are the sources of the electromagnetic

waves. When a charged particle oscillates, it produces oscillating electric and magnetic fields, which are called light. The energy of the produced electromagnetic wave can be determined from the frequency of the oscillating charged particle. As a result, the spectrum of the electromagnetic wave involves a huge range of frequencies that range from below 1 Hz to above 1025 Hz. These waves can propagate in space with a speed of 300,000 km/sec. In addition, they can interact in different degrees with materials such as metals, semiconductors, and insulators. Metals that have bound and free electrons can interact with the electromagnetic field; the strength of the interaction depends on the energy of the wave energy and the number of the electrons in the conduction and valence bands of metals. For example, the electromagnetic waves at low-frequencies (microwave and far-infrared) regime cannot penetrate and interact with metals due to their low energies; thus, metals can be considered as perfect reflectors. Because of this, these types of metals are used as waveguides and resonators at these frequencies. At high frequencies such as near-infrared and visible waves, on the other hand, penetration and interaction of the electromagnetic waves with metals can be taken into consideration due to the high energies. At ultraviolet frequencies (very high energies), for example, electromagnetic waves can interact strongly with the bound and free electrons of metals such as gold or silver, resulting in a strong absorption. A complex dielectric function $\varepsilon(\omega)$ describes the dispersive properties of the interaction (optical properties of metal) between the electrons and the electromagnetic field.

Before delving into the details of the optical response of metals, it is important to give a brief explanation of the basics of electromagnetic wave equations, which are called Maxwell's macroscopic equations, or Maxwell's equations of matter. These equations are represented in the next four differential forms.[48]

$$\nabla \cdot \mathbf{D} = \rho_{\text{ext}} \qquad \text{(Equation 2.1)}$$

$$\nabla \cdot \mathbf{B} = 0 \qquad \text{(Equation 2.2)}$$

$$\nabla \times \mathbf{E} = -\frac{\partial \mathbf{B}}{\partial \mathrm{t}} \qquad \text{(Equation 2.3)}$$

$$\nabla \times \mathbf{H} = \mathbf{J}_{\mathrm{ext}} + \frac{\partial \mathbf{D}}{\partial \mathrm{t}} \qquad \text{(Equation 2.4)}$$

where $\mathbf{D}, \mathbf{B}, \mathbf{E}, \mathbf{H}, \rho_{\mathrm{ext}}$, and $\mathbf{J}_{\mathrm{ext}}$ are dielectric displacement, magnetic flux density, electric field, magnetic field, external charge, and external current density, respectively.

Equation 2.1 is known as Gauss's law; it states that electric charges generate an electric field, and the electric flux comes out from the closed surface, surrounding the charge, is proportional to the charge enclosed. Equation 2.2 is known as Gauss's law for the magnetic field. It states that there is no magnetic monopole since the divergence of magnetic flux is equal to zero. Equation 2.3 is known as Faraday's law; it states that an electric field can be generated or induced when a magnetic field changes with time. The induced electric field is in the opposite direction of the magnetic field. Finally, Equation 2.4 is known as Ampere's law. It states that a magnetic field can be generated as an electric field changes with time.

Both ρ_{tot}, and $\mathbf{J}_{\mathrm{tot}}$ are given by Equation 2.5 and Equation 2.6.

$$\rho_{\mathrm{tot}} = \rho_{\mathrm{ext}} + \rho \qquad \text{(Equation 2.5)}$$

$$\mathbf{J}_{\mathrm{tot}} = \mathbf{J}_{\mathrm{ext}} + \mathbf{J} \qquad \text{(Equation 2.6)}$$

where ρ and $\mathbf{J}$ are the internal charge and current density. ρ_{ext}, and $\mathbf{J}_{\mathrm{ext}}$ drive the system, whereas, ρ and $\mathbf{J}$ respond to ρ_{ext}, and $\mathbf{J}_{\mathrm{ext}}$.

Fields inside a metal can be connected and represented in a linear relationship by polarization $\mathbf{P}$ (Equation 2.7) and magnetization $\mathbf{M}$ (Equation 2.8).[49]

$$\mathbf{D} = \varepsilon_0 \mathbf{E} + \mathbf{P} \quad \text{(Equation 2.7)}$$

$$\mathbf{H} = \frac{\mathbf{B}}{\mu_0} - \mathbf{M} \quad \text{(Equation 2.8)}$$

where ε_0 and μ_0 are the electric permittivity and magnetic permeability of free space, which are given by Equation 2.9 and Equation 2.10, respectively.

$$\varepsilon_0 = 8.85 \times 10^{-12} \frac{\mathrm{F}}{\mathrm{m}} \quad \text{(Equation 2.9)}$$

$$\mu_0 = 4\pi \times 10^{-7} \approx 1.26 \times 10^{-6} \frac{\mathrm{H}}{\mathrm{m}} \quad \text{(Equation 2.10)}$$

Since nonmagnetic materials will be taken into consideration, only Equation 2.7 is used in the calculations. **P** is defined as the total electric dipole moments inside the metal per unit volume. Since they are inside the metal, they are related to the internal charge density and it could be written as Equation 2.11, and the charge conservation is written in Equation 2.12.

$$\nabla \cdot \mathbf{P} = -\rho \quad \text{(Equation 2.11)}$$

$$\nabla \cdot \mathbf{J} = -\frac{\partial \rho}{\partial \mathrm{t}} \quad \text{(Equation 2.12)}$$

A correlation between **J** and **P** can be established from Equation 2.11 and Equation 2.12 and represented in Equation 2.13.

$$\mathbf{J} = \frac{\partial \mathbf{P}}{\partial \mathrm{t}} \quad \text{(Equation 2.13)}$$

Inserting Equation 2.1 into Equation 2.7, the linear correlation between **E** and ρ_{tot} is represented in Equation 2.14.

$$\nabla \cdot \mathbf{E} = \frac{\rho_{tot}}{\varepsilon_0} \quad \text{(Equation 2.14)}$$

In the case of a linear, isotropic and nonmagnetic medium, **D** and **E** can be connected via Equation 2.15.

$$\mathbf{D} = \varepsilon\, \varepsilon_0 \mathbf{E} \quad \text{(Equation 2.15)}$$

B and **H** can be connected via Equation 2.16.

$$\mathbf{B} = \mu\, \mu_0 \mathbf{H} \quad \text{(Equation 2.16)}$$

where ε and μ are relative permittivity (dielectric constant), which can be given by Equation 2.17, and relative permeability, which is equal to 1 for nonmagnetic media, respectively.[50]

$$\varepsilon(\omega) = \frac{\tilde{\varepsilon}(\omega)}{\varepsilon_0} \quad \text{(Equation 2.17)}$$

where $\tilde{\varepsilon}(\omega)$ is the complex permittivity (angular frequency-dependent) of the material. Electric susceptibility (χ) is another term that is used to describe the optical response in quantum mechanical treatments.

$$\mathbf{P} = \varepsilon_0 \chi \mathbf{E} \quad \text{(Equation 2.18)}$$

By substituting Equation 2.7 and Equation 2.18 in Equation 2.15, a new relationship between ε and χ is written in Equation 2.19.[51]

$$\varepsilon(\omega) = \frac{\tilde{\varepsilon}(\omega)}{\varepsilon_0} = 1 + \chi \quad \text{(Equation 2.19)}$$

The other linear relationship between **E** and **J** is given via σ in Equation 2.20.[50, 52]

$$\mathbf{J} = \sigma\, \mathbf{E} \quad \text{(Equation 2.20)}$$

In the case of the linear media without spatial dispersion, the optical response of metals

depends on both frequency (ω) and wave vector (**k**) of the electromagnetic wave. A linear correlation can be generalized and represented in Equation 2.21 and Equation 2.22 when the non-locality in t and **r** are taken into consideration.[49]

$$\mathbf{D}(\mathbf{r},\mathrm{t}) = \varepsilon_0 \int \mathrm{d}\mathrm{t}'\mathrm{d}\mathbf{r}'\varepsilon_\mathrm{r}(\mathbf{r}-\mathbf{r}',\mathrm{t}-\mathrm{t}')\mathbf{E}(\mathbf{r}',\mathrm{t}') \qquad \text{(Equation 2.21)}$$

$$\mathbf{J}(\mathbf{r},\mathrm{t}) = \int \mathrm{d}\mathrm{t}'\mathrm{d}\mathbf{r}'\sigma(\mathbf{r}-\mathbf{r}',\mathrm{t}-\mathrm{t}')\mathbf{E}(\mathbf{r}',\mathrm{t}') \qquad \text{(Equation 2.22)}$$

By applying Fourier transformation on the two previous equations, the fields can be decomposed into plane wave components. These components are functions of **k** and ω, Equation 2.23 and Equation 2.24, respectively.

$$\mathbf{D}(\mathbf{k},\omega) = \varepsilon_0\varepsilon(\mathbf{k},\omega)\mathbf{E}(\mathbf{k},\omega) \qquad \text{(Equation 2.23)}$$

$$\mathbf{J}(\mathbf{k},\omega) = \sigma(\mathbf{k},\omega)\mathbf{E}(\mathbf{k},\omega) \qquad \text{(Equation 2.24)}$$

Equation 2.25 connects both σ and $\varepsilon(\mathbf{k},\omega)$ in a relationship after using Equation 2.7, Equation 2.13, Equation 2.23 and Equation 2.24.

$$\varepsilon(\mathbf{k},\omega) = 1 + \frac{\mathrm{i}\sigma(\mathbf{k},\omega)}{\varepsilon_0\omega} \qquad \text{(Equation 2.25)}$$

Typically, at the ultraviolet, visible, and near infrared frequencies with a limit of a spatially local response, $\varepsilon(\mathbf{k},\omega)$ can be written as $\varepsilon(\mathbf{k}=0,\omega)$ when the light interacts with metal. This condition works when the mean free path of the electrons or the unit cell is shorter than the wavelength in the material. At low frequencies, the incident electric field can affect the bound and the free electrons; thus, $\varepsilon(\mathbf{k},\omega)$ and $\sigma(\mathbf{k},\omega)$ can describe the optical response and the current flow, respectively. Both $\varepsilon(\omega)$ and $\sigma(\omega)$ are complex functions and they can be written as:

$$\varepsilon(\omega) = \varepsilon_1(\omega) + \mathrm{j}\,\varepsilon_2(\omega) \quad \text{(Equation 2.26)}$$

$$\sigma(\omega) = \sigma_1(\omega) + \mathrm{j}\,\sigma_2(\omega) \quad \text{(Equation 2.27)}$$

At the visible range of wavelengths, $\varepsilon(\omega)$ can be calculated by experimentally studying reflectivity by which the complex refractive index ($\tilde{n}$) of the medium can be determined.

$$\tilde{n}(\omega) = n(\omega) + \mathrm{i}\,\kappa(\omega),\ \tilde{n}(\omega) = \sqrt{\varepsilon} \quad \text{(Equation 2.28)}$$

where n and κ are the real refractive index and the extinction coefficient that measures the absorption of a medium at a given frequency, respectively.[49]

$$\varepsilon_1 = n^2 - \kappa^2 \quad \text{(Equation 2.29)}$$

$$\varepsilon_2 = 2\,n\,\kappa \quad \text{(Equation 2.30)}$$

$$n^2 = \frac{\varepsilon_1}{2} + \frac{1}{2}\sqrt{\varepsilon_1^2 + \varepsilon_2^2} \quad \text{(Equation 2.31)}$$

$$\kappa = \frac{\varepsilon_2}{2n} \quad \text{(Equation 2.32)}$$

The extinction coefficient (κ) is connected to Beer's law that measures the reduction of the intensity (I_0) of the incident light on a medium.[53]

$$\mathrm{I}(\mathrm{x_m}) = \mathrm{I_0 e^{-\alpha_{ac} x_m}} \quad \text{(Equation 2.33)}$$

where x_m is the thickness of the medium, I is the attenuated light intensity, and α_{ac} is the absorption coefficient, which is given by Equation 2.34.

$$\alpha_{ac}(\omega) = 1 + \frac{2\,\kappa\,(\omega)\,\omega}{\mathrm{c}} \quad \text{(Equation 2.34)}$$

ε_1 and ε_2 are used to determine the real refractive index (Equation 2.29) and the

absorption inside the material (Equation 2.30), respectively. From Equation 2.3 and Equation 2.4 the wave equation can be extracted in the time (Equation 2.35) and Fourier domains (Equation 2.36), respectively.

$$\nabla \times \nabla \times \mathbf{E} = \mu_0 \frac{\partial^2 \mathbf{D}}{\partial t^2} \qquad \text{(Equation 2.35)}$$

$$\mathbf{k}(\mathbf{k}.\mathbf{E}) - \mathbf{k}^2\mathbf{E} = -\varepsilon(\mathbf{k},\omega)\frac{\omega^2}{c^2}\mathbf{E} \qquad \text{(Equation 2.36)}$$

where $c = \frac{1}{\sqrt{\varepsilon_0 \mu_0}}$ is the speed of light in space, as mentioned above.

Transverse and longitudinal polarizations are two cases of the electric field vector that are taken into consideration. In the case of the transverse wave, $\mathbf{k} \cdot \mathbf{E} = 0$ that results in a dispersion relationship, which connects the wave vector ($\mathbf{k}$) with angular frequency(ω) (Equation 2.37).

$$\mathbf{k}^2 = \varepsilon(\mathbf{k},\omega)\frac{\omega^2}{c^2} \qquad \text{(Equation 2.37)}$$

In the case of the longitudinal wave, the dispersion relationship is given by Equation 2.38.[48]

$$\varepsilon(\mathbf{k},\omega) = 0 \qquad \text{(Equation 2.38)}$$

2.2 Drude-Lorentz model of the optical response

As a starting point, Paul K.L. Drude produced a model that counts the valence electrons (free electrons) of metals act as a gas surrounds the ions as cores.[54] In his model, he assumed that only the free electrons can affect the electromagnetic response of a metal. That means there is no restoring force because the free electrons are not bound. This model was developed with Lorentz model to describe the optical properties of solid materials for both free and bound electrons

contribution.

Figure 2.2.1 shows a model of an electron that is bound with a nucleus within a medium. This model can be treated as a harmonic oscillator.

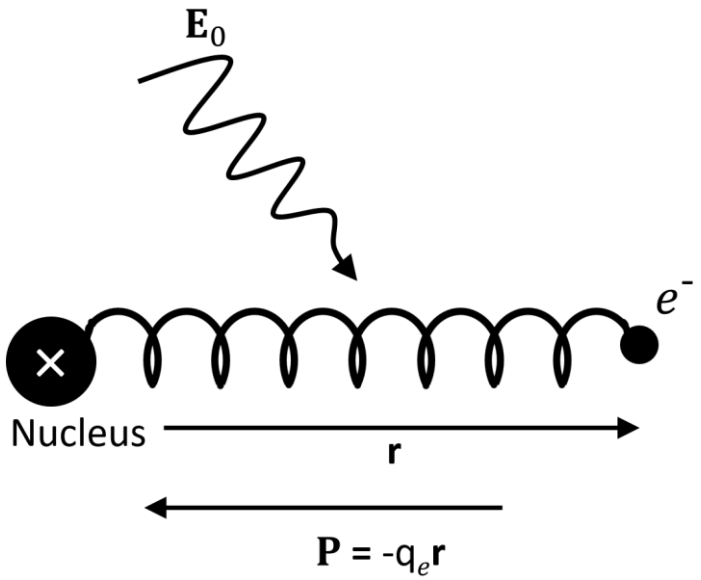

Figure 2.2.1. A harmonic oscillator model for electron.

When an external incident electric field hits the system, it excites the bound electron and makes it oscillate. This excitation shifts the electron farther from the nucleus. This process can generate a so-called "induced electric field", which tries to restore the bound electron to the equilibrium position. By applying Newton's second law, the net forces of the system can be calculated (Equation 2.39).

$$F_{net} = m \cdot a = \mathrm{m_e}\frac{\partial^2 \mathbf{r}(\mathrm{t})}{\partial \mathrm{t}^2} = \sum_{\mathrm{i}} \mathbf{F}_{\mathrm{i}} = \mathbf{F}_{\mathrm{E}}(\mathrm{t}) + \mathbf{F}_{\mathrm{S}}(\mathrm{t}) + \mathbf{F}_{\mathrm{D}}(\mathrm{t}) \quad \text{(Equation 2.39)}$$

$\mathrm{m_e}$ and $\mathbf{r}(t)$, are the effective mass of the electron and the new position of the electron (time-dependent) after shifting from the balanced position, respectively. $\mathbf{F}_{\mathrm{E}}(\mathrm{t})$ is called the local force that comes from the incident electric field; it is given by Equation 2.40.[53]

$$\mathbf{F}_E(t) = q_e \mathbf{E}_0 e^{-j\omega t} \quad \text{(Equation 2.40)}$$

where q_e, $\mathbf{E}_0$, are the charge of the electron and the amplitude of the incident electric field, respectively.

$\mathbf{F}_S(t)$ is the restoration force, which is defined as the force that is exerted by the induced electric field to return the electron at the balanced position; It is proportional to **r** and given by Equation 2.41.

$$\mathbf{F}_S(t) = -q \times \mathbf{r}(t) \quad \text{(Equation 2.41)}$$

The equilibrium position (q) is given by Equation 2.42.

$$q = m_e \omega_0^2 \quad \text{(Equation 2.42)}$$

where ω_0 is the natural frequency of the bound electron. The last part of Equation 2.39 is defined as the damping force $\mathbf{F}_D(t)$, which is given by Equation 2.43.

$$\mathbf{F}_D(t) = -\gamma \left[\frac{\partial \mathbf{r}(t)}{\partial t}\right] \quad \text{(Equation 2.43)}$$

where γ is the damping coefficient in Hertz. By combining Equation 2.40, Equation 2.41 and Equation 2.43, the net forces of the harmonic oscillator of the system can be given in Equation 2.44.

$$m_e \frac{\partial^2 \mathbf{r}}{\partial t^2} + m_e \gamma \frac{\partial \mathbf{r}}{\partial t} + m_e \omega_0^2 \mathbf{r} = q_e \mathbf{E}_0 e^{-j\omega t} \quad \text{(Equation 2.44)}$$

The general solution of (Equation 2.44) for monochromatic electric field is given by Equation 2.45.[49]

$$\mathbf{r}(\omega) = \frac{q_e}{m_e(\omega_0^2 - \omega^2 - j\gamma\omega)} \mathbf{E}(\omega) \quad \text{(Equation 2.45)}$$

Because of the deviation of the bound electron from the balanced position, a dipole moment is generated and the induced polarization density of the total dipoles is given by Equation 2.46.

$$\mathbf{P} = N_e q_e \mathbf{r}(\omega) = \frac{N_e q_e}{m_e(\omega_0^2 - \omega^2 - j\gamma\omega)}\mathbf{E}(\omega) \qquad \text{(Equation 2.46)}$$

where N_e is the electron density per unit volume. By applying Equation 2.19 and Equation 2.46, the equation of the dielectric function of free and bound electrons is given by Equation 2.47.

$$\varepsilon(\omega) = 1 + \frac{\omega_p^2}{(\omega_0^2 - \omega^2 - j\gamma\omega)} \qquad \text{(Equation 2.47)}$$

where ω_p is called the plasma frequency and given by (Equation 2.48).

$$\omega_p^2 = \frac{N_e q_e^2}{m_e \varepsilon_0} \qquad \text{(Equation 2.48)}$$

The real and imaginary parts of the dielectric function (Equation 2.47) can be written as:[55,56]

$$\varepsilon'(\omega) = 1 + \frac{\omega_p^2(\omega_0^2 - \omega^2)}{(\omega_0^2 - \omega^2)^2 + \gamma^2\omega^2)} \qquad \text{(Equation 2.49)}$$

$$\varepsilon''(\omega) = 1 + \frac{\omega_p^2\, \gamma\, \omega}{(\omega_0^2 - \omega^2)^2 + \gamma^2\omega^2} \qquad \text{(Equation 2.50)}$$

Using the last two equations, plots of the real and imaginary parts of the gold permittivity were illustrated in Figure 2.2.2. The plots show the contribution of the free and bound electrons in the permittivity. There is a small mismatch between the calculated and measured curves for the imaginary part. This result might confirm that the Drude-Lorentz model is able to present the close values of the gold permittivity in some frequency regions. However, a close matching

appears between the real parts.

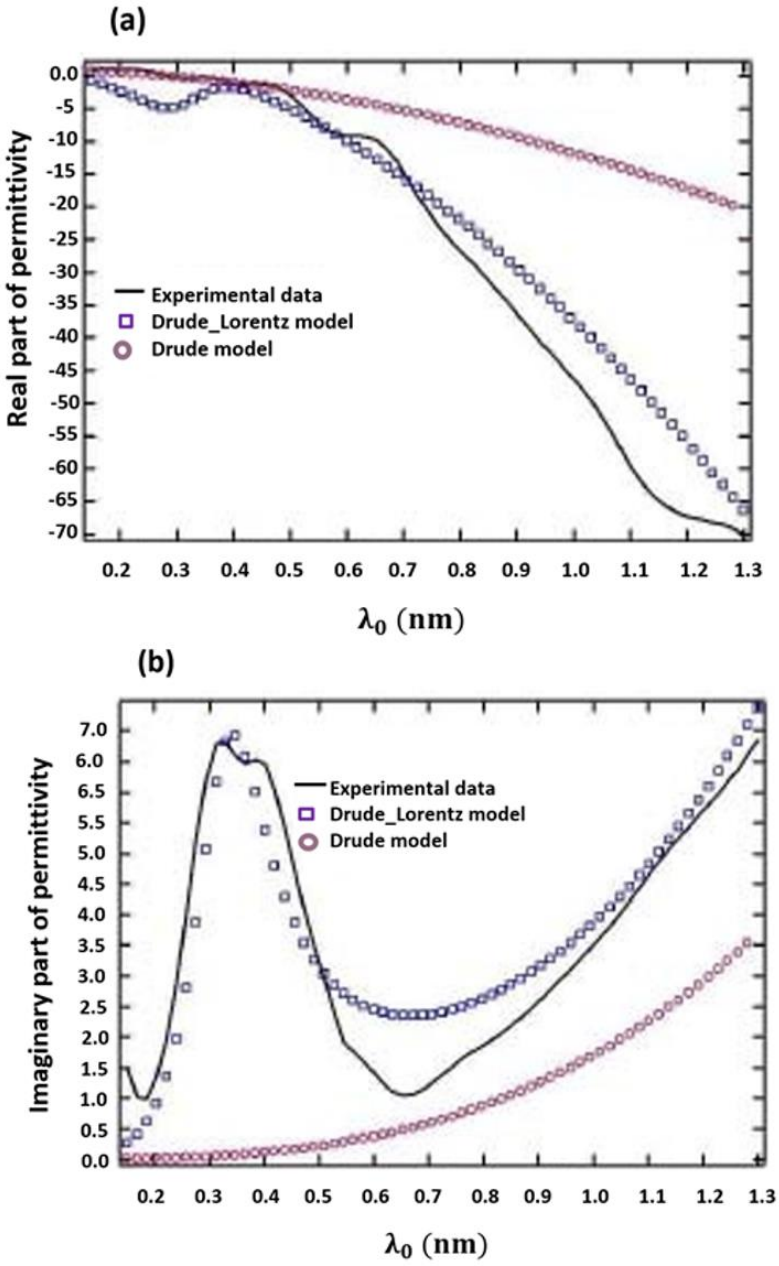

Figure 2.2.2. ε (real and imaginary parts) vs. λ for gold, estimated by the Drude-Lorentz and Drude models and measured data.[57]

So far, the dielectric function of the system that has the free and the bound electrons was presented by the Drude-Lorentz model. However, a special case of this model, including only the

free electron, which is called the Drude model, will be presented in the rest of this section. Including only the free electrons means excluding the restoration force from Equation 2.39 because the conduction electrons freely move, as mentioned above. According to the Drude model, the net forces of the new system can be written as:

$$m_e \frac{\partial^2 \mathbf{r}}{\partial t^2} + m_e \gamma \frac{\partial \mathbf{r}}{\partial t} = -q_e \mathbf{E}_0 e^{-j\omega t} \qquad \text{(Equation 2.51)}$$

Solving the differential equation (Equation 2.51), the displacement **r** of the electron can be obtained in Equation 2.52.

$$\mathbf{r}(t) = \frac{q_e}{m_e(\omega^2 + j\gamma\omega)} \mathbf{E}(\omega) \qquad \text{(Equation 2.52)}$$

The polarization density of the total system per unit volume can be written as:

$$\mathbf{P} = N \times q_e \times \mathbf{r}(\omega) = \frac{N_f \times q_e}{m_e(\omega^2 + j\gamma\omega)} \mathbf{E}(\omega) \qquad \text{(Equation 2.53)}$$

where N_f is the number of free electrons in the metal per unit volume. The dielectric function of the system that has only free electrons is thus obtained:

$$\varepsilon_{Drude}(\omega) = 1 - \frac{\omega_p^2}{\omega^2 + j\gamma\omega} \qquad \text{(Equation 2.54)}$$

Equation 2.54 shows how the free electrons contribute to the dielectric function of the metals. The real and imaginary parts of Equation 2.54 can be written as:[49,58]

$$\varepsilon_{Drude}(\omega) = \varepsilon' + j\varepsilon'' = \left(1 - \frac{\omega_p^2}{\omega^2 + \gamma^2}\right) + j\frac{\omega_p^2 \gamma}{\omega(\omega^2 + \gamma^2)} \qquad \text{(Equation 2.55)}$$

If $\omega >> \gamma$, Equation 2.55 can be simplified to:

$$\varepsilon_{\text{Drude}} \approx 1 - \frac{\omega_p^2}{\omega^2} + j\frac{\omega_p^2\,\gamma}{\omega^3} \qquad \text{(Equation 2.56)}$$

By using Equation 2.55, the permittivity of gold was determined and plotted versus the incident wavelength (200-1200 nm) in Figure 2.2.3. Both the measured and the calculated values for the real parts are unmatched.

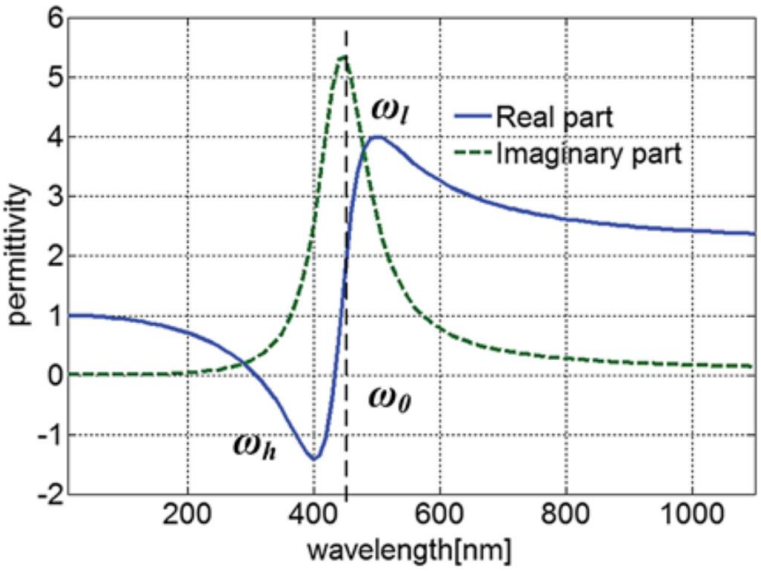

Figure 2.2.3. ε of gold vs. λ_0 for the real and imaginary parts by the Drude model.[57]

For the imaginary part, the curves of the measured and the calculated values at wavelengths greater than 650 nm are close in the trend. In the region below 650 nm, however, the Drude model failed to match the measured data because the bound electrons were not taken into consideration, and this is due to the low energies at this range. As a result, no interaction between the incident electric field and the bound electrons has taken place.

The contribution of only the bound electrons was determined by Equation 2.57.

$$\varepsilon(\omega) = 1 + \frac{\omega_1^2}{\omega_0^2 - \omega^2 - j\gamma\omega} \qquad \text{(Equation 2.57)}$$

where ω_1 is the corresponding frequency of the bound electron. Equation 2.57 was used to calculate the permittivity of gold as a function of wavelength.

2.3 Plasmons and surface plasmon polaritons (SPPs)

The typical band structure of materials such as insulators, semiconductors, and metals is composed of a conduction band, valence band, and energy bandgap. In general, each material has a certain number of electrons in their atomic structure, and these electrons can be divided into two types: interband electrons (bound electrons) and intraband electrons (free conduction electrons). Both types of electrons play a fundamental role to determine the complex dielectric functions which in turn determine the optical properties of materials. Intraband electrons can be excited by low electromagnetic energies and freely moved within materials; however, the interband electrons require electromagnetic energies that are larger than their bandgap energy in order to move and transit from one energy level to another. [59]

In 1956, Pines was the first person to introduce the term "plasmon". He defined plasmon as, "The valence electron collective oscillations resemble closely the electronic plasma oscillations observed in gaseous discharges. The term "plasmon" is introduced to describe the quantum of elementary excitation associated with this high frequency collective motion".[59,60] Briefly, plasmons are collective oscillations of free electrons in the valence band. A photon is a particle, whereas a plasmon is a quasi-particle because plasmons are always lossy and highly interactive.[59–61] In 1957, Ritchie suggested new types of plasma modes in thin metal films. This new kind of plasma corresponds to longitudinal charge density waves propagating at a dielectric/metal interface. In 1959 and in 1960, new types were discovered in an experimental method. These quantized modes were named surface plasmon polaritons (SPPs).[60] SPPs are

electromagnetic waves that decay evanescently perpendicular to the interface into the metal and the dielectric, as illustrated in Figure 2.3.1.

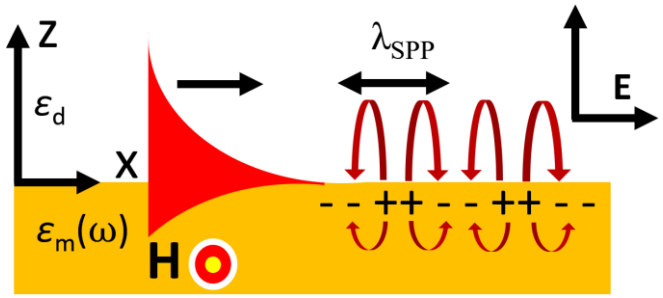

Figure 2.3.1. Surface plasmon polariton (SPP) with its wavelength λ_{SPP}.

SPPs have several peculiarities, one of which is their wave vector that is larger than the wave vector of the photon of the incident light. SPPs have four main length scales that are useful in their applications. First, the wavelength of SPP (λ_{SPP}), considered to be the most important length scale, represents the separation of positions of equal charge on the surface. The wavelength of SPP can be calculated from the real and imaginary parts of the complex dispersion relation as shown in Equation 2.58.[59, 62]

$$\lambda_{SPP} = \lambda_o \sqrt{\frac{\varepsilon_d \varepsilon'_m}{\varepsilon_d + \varepsilon'_m}} \qquad \text{(Equation 2.58)}$$

where ε_d is the dielectric permittivity. Equation 2.59 shows the second length scale of SPP, which is the SPP propagation length (LSPP). LSPP represents the distance traveled by the SPP until its intensity is diminished by e^{-1}.

$$L_{SPP} = \lambda_o \frac{(\varepsilon'_m)^2}{2\pi\varepsilon''_m} \qquad \text{(Equation 2.59)}$$

ε'_m and ε''_m are the real and the imaginary parts of a metal's permittivity, respectively. The two remaining length scales are the penetration depths in dielectric Equation 2.60 and metal

Equation 2.61 that are defined as the field distance in metal and dielectric media before SPP is reduced by e^{-1}.[60,62]

$$\delta_d = \lambda_o \left| \frac{\varepsilon_d + \varepsilon'_m}{\varepsilon_d^2} \right|^{\frac{1}{2}} \quad \text{(Equation 2.60)}$$

$$\delta_m = \lambda_o \left| \frac{\varepsilon_d + \varepsilon'_m}{\varepsilon_m'^2} \right|^{\frac{1}{2}} \quad \text{(Equation 2.61)}$$

Several types of materials such as gold (Au), silver (Ag), copper (Cu), and aluminum (Al) are considered to be very strong plasmonic materials because they have plenty of free electrons in their valence bands. As previously mentioned, two components of waves, p-polarized and s-polarized waves, can be obtained from the solution of Maxwell's equations (Equations 2.1-4). The p-polarized waves mean the electric field is parallel to the incidence plane; however, the s-polarized waves mean the magnetic field is parallel to the incidence plane. From Figure 2.3.1, the considered parallel p-polarized wave in the metal and dielectric media can be written as:

$$\begin{pmatrix} \mathbf{E}_i \\ \mathbf{H}_i \end{pmatrix} = \begin{pmatrix} \mathbf{E}_{x,i} & 0 & \mathbf{E}_{z,i} \\ 0 & \mathbf{H}_{y,i} & 0 \end{pmatrix} e^{j(k_{x,i}\mathbf{x} - \omega t + k_{z,i}\mathbf{z})}, i = m, d \quad \text{(Equation 2.62)}$$

For the dielectric medium, it is written as:

$$\mathbf{E}_d = (\mathbf{E}_{x,d}, 0, \mathbf{E}_{z,d}) e^{j(k_{x,d}\mathbf{x} + k_{z,d}\mathbf{z} - \omega t)} \quad \text{(Equation 2.63)}$$

$$\mathbf{H}_d = (0, \mathbf{H}_{y,d}, 0) e^{j(k_{x,d}\mathbf{x} + k_{z,d}\mathbf{z} - \omega t)} \quad \text{(Equation 2.64)}$$

And for the metal medium, it is written as:

$$\mathbf{E}_m = (\mathbf{E}_{x,m}, 0, \mathbf{E}_{z,m}) e^{j(k_{x,m}\mathbf{x} + k_{z,m}\mathbf{z} - \omega t)} \quad \text{(Equation 2.65)}$$

$$\mathbf{H}_m = (0, \mathbf{H}_{y,m}, 0)e^{j(k_{x,m}\mathbf{x}+k_{z,m}\mathbf{z}-\omega t)} \quad \text{(Equation 2.66)}$$

After several steps of simplification, the dispersion relation of the surface plasmon wave that propagates at the metal-dielectric interface can be given by,

$$\mathbf{k}_{sp}^2 = \mathbf{k}_x^2 = \frac{\varepsilon_d \varepsilon_m}{\varepsilon_d + \varepsilon_m}\mathbf{k}^2 = \frac{\varepsilon_d \varepsilon_m}{\varepsilon_d + \varepsilon_m}\frac{\omega^2}{c^2} \quad \text{(Equation 2.67)}$$

Then, the real and imaginary parts of the wave vector are given by,

$$\mathbf{k}_x = \mathbf{k}_x' + j\mathbf{k}_x'' = \frac{\omega}{c}\sqrt{\frac{\varepsilon_d \varepsilon_m}{\varepsilon_d + \varepsilon_m}} \quad \text{(Equation 2.68)}$$

The real and imaginary parts of the wave vector for noble metals in the visible light and infrared region can be individually written as,

$$\mathbf{k}_x' \approx \frac{\omega}{c}\sqrt{\frac{\varepsilon_d \varepsilon_m}{\varepsilon_d + \varepsilon_m}} \quad \text{(Equation 2.69)}$$

$$\mathbf{k}_x'' = \frac{1}{2}\frac{\omega}{c}\left(\frac{\varepsilon_d \varepsilon_m'}{\varepsilon_d + \varepsilon_m'}\right)^{3/2}\frac{\varepsilon_m''}{(\varepsilon_m')^2} \quad \text{(Equation 2.70)}$$

The normal component of the p-polarized wave can be given by,

$$\mathbf{k}_{z,d}^2 = \left(\frac{\omega}{c}\right)^2 \frac{\varepsilon_d^2}{\varepsilon_d + \varepsilon_m} \quad \text{(Equation 2.71)}$$

$$\mathbf{k}_{z,m}^2 = \left(\frac{\omega}{c}\right)^2 \frac{\varepsilon_m^2}{\varepsilon_d + \varepsilon_m} \quad \text{(Equation 2.72)}$$

Inserting Equation 2.26 into Equation 2.71 and Equation 2.72, the dispersion relation is written as,

$$\mathbf{k}_{z,i} = \pm j\frac{\omega}{c}\sqrt{\mathbf{k}_x^2 - \varepsilon_i\left(\frac{\omega}{c}\right)^2}, i = m, d \qquad \text{(Equation 2.73)}$$

From Equation 2.68, one required condition must be applied to obtain the propagated SP at the metal-dielectric interface. This condition is,

$$\frac{\varepsilon_d\varepsilon_m}{\varepsilon_d + \varepsilon_m} > 0 \qquad \text{(Equation 2.74)}$$

This means

$$\begin{cases}\varepsilon_d(\omega) + \varepsilon_m(\omega) < 0 \\ \varepsilon_d(\omega) \cdot \varepsilon_m(\omega) < 0\end{cases} \qquad \text{(Equation 2.75)}$$

One of the permittivities must be negative and its absolute value must be greater than the other permittivity, which means,

$$\varepsilon'_m(\omega) < -\varepsilon'_d(\omega) \qquad \text{(Equation 2.76)}$$

In the case of $|\varepsilon'_m| >> \varepsilon''_m$, Equation 2.70 can be neglected and according to the Drude model, the dielectric function of a bulk metal can be given by,

$$\varepsilon_m = 1 - \left(\frac{\omega_p}{\omega}\right)^2 \qquad \text{(Equation 2.77)}$$

Inserting Equation 2.77 into Equation 2.68 and making $\varepsilon_m \rightarrow -\varepsilon_d$, the angular frequency can be written as,

$$\omega_{sp} \approx \omega_p/\sqrt{2} \qquad \text{(Equation 2.78)}$$

Equation 2.78 connects the frequencies of the SP and the plasma; it indicates that the energy of SP waves is independent from the incident wave vector.

2.4 Surface plasmon excitation and light transmission enhancement techniques

Figure 2.4.1 shows the dispersion relations of light (dashed line) and SPP (solid line). The region on the right side of the light line represents the non-radiative region. SPP belongs to this region and it never interacts with the light line. Because of this, a momentum deviation **L** between the two lines is generated at the same frequencies.

$$\mathbf{k}_{sp} = \mathbf{k}_{in} + \mathbf{L} \qquad \text{(Equation 2.79)}$$

where $\mathbf{k}_{in}$is the wave vector of the incident light. This means SPP cannot be directly excited by the incident wave. However, to solve this momentum mismatch, an additional momentum must be presented. Several excitation techniques such as evanescent waves, prism, corrugated grating, and near field can be used to generate the additional momentum **L** and excite SPP.

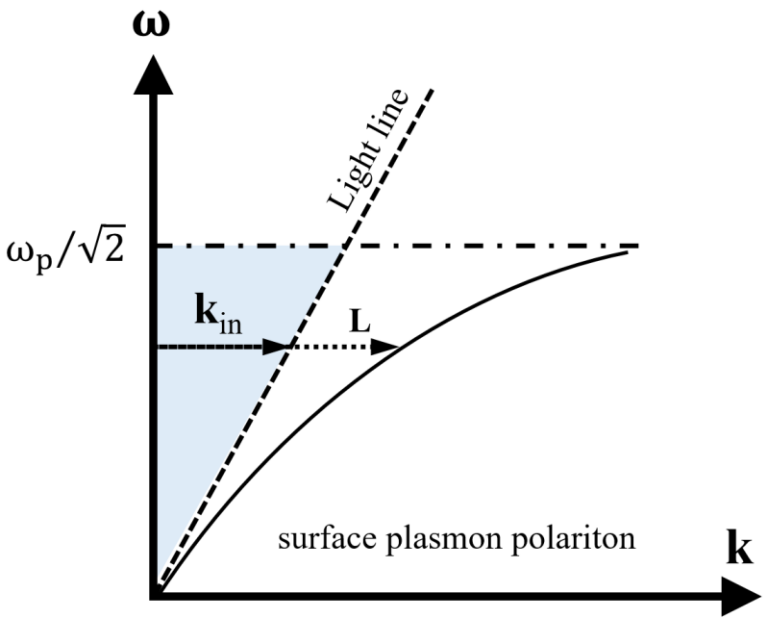

Figure 2.4.1. Dispersion relation of SPP and light.

$$\mathbf{k}_{x,m} = \mathbf{k}_{x,d} = \sqrt{\varepsilon_d}\left(\frac{\omega}{c}\right)\sin(\alpha_{in}) \qquad \text{(Equation 2.80)}$$

According to Equation 2.80, the incident angle factor of an electromagnetic wave on a

metal surface can generate the so-called evanescent waves at the metal-dielectric interface. By changing the incident angle, the wave vector decomposes into two components in the x and z directions, Figure 2.4.2. Both components are a function of the incident angle. The reduced horizontal component of the incident wave vector at an angle larger than the critical angle ($\alpha_c = \sqrt{\varepsilon_m/\varepsilon_d}$) can match the wave vector of SP. As a result, it would be possible for the incident light to couple with the SPPs. There is another mechanism that can be used to coincide the wave vectors of the incident light and SPPs. This mechanism is called the attenuated total reflection (ATR) or the Kretschmann configuration, see Figure 2.4.3 (a).

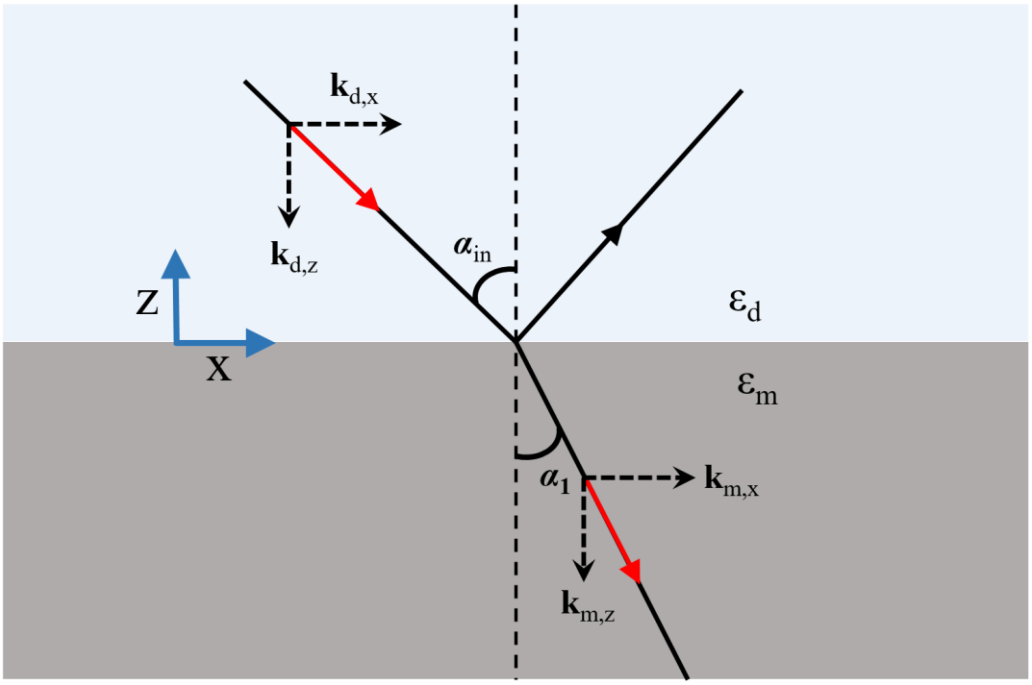

Figure 2.4.2. Reflected and refracted light waves between two media.

In this method, an optically dense medium, such as a prism, is used to create the evanescent waves at the metal-air interface when a thin gold layer is deposited on the top of a prism. This means, instead of using air as a dielectric medium (ε_d), the prism (ε_p) can be used in this case; thus, Equation 2.80 can be modified and written as,

$$\mathbf{k}_{x,m} = \mathbf{k}_{x,d} = \sqrt{\varepsilon_p}\left(\frac{\omega}{c}\right)\sin(\alpha_{in}) \qquad \text{(Equation 2.81)}$$

where ε_p is the permittivity of the prism material, Figure 2.4.3 (a).

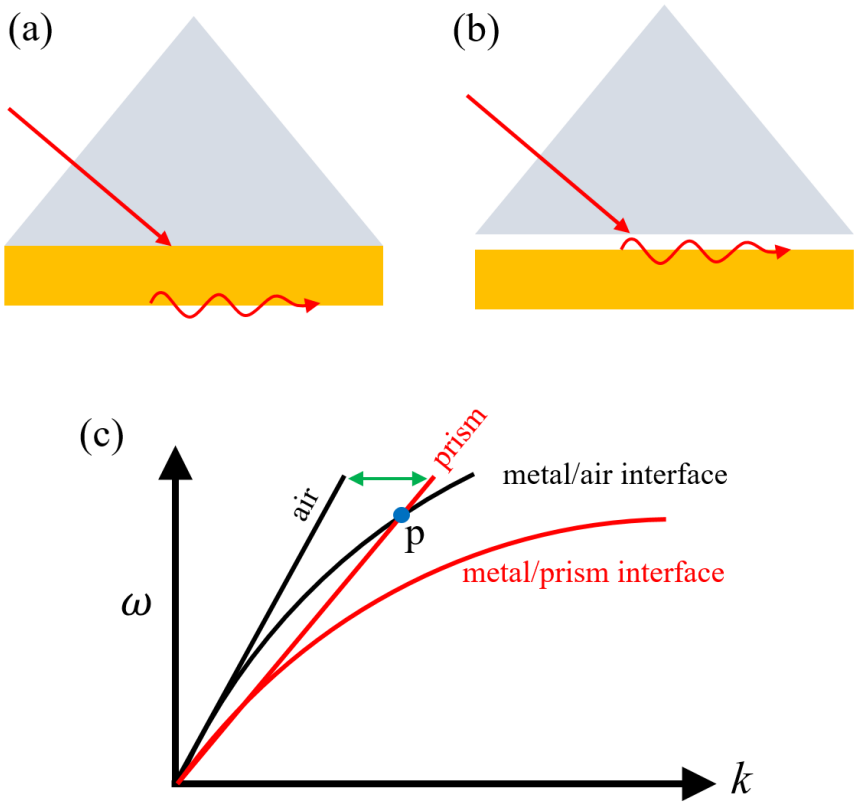

Figure 2.4.3. Coupling mechanisms for SPPs and dispersion relation.

However, the evanescent waves could propagate on the top metal-air interface when a very small thin layer of dielectric medium is inserted between the prism and the metal layer. This mechanism is called the Otto configuration, Figure 2.4.3 (b). By using the Kretschmann or Otto configuration, a cross at point p between the prism and the SP lines occurs. This means both the energies and the momentums of the incident light and the SPPs are coincident at the same frequency, Figure 2.4.3 (c).

The next mechanism of exciting SPPs is called the near-field excitation. This mechanism

could unintentionally take place due to the surface corrugations, such as surface roughness. This could happen in the sample fabrication as shown in Figure 2.4.4.

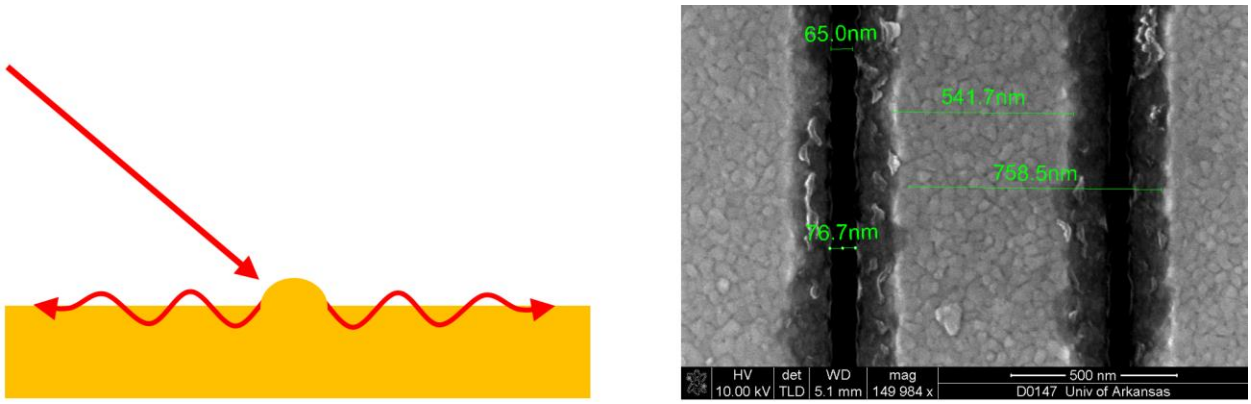

Figure 2.4.4. Scattering by surface roughness.

The last mechanism that can be used to eliminate the momentum mismatch between the incident light and the SPPs is called the grating excitation, Figure 2.4.5. This dissertation work completely depends on this mechanism. Generally, the diffraction grating equation is given by Equation 2.82:

$$n_{\mathrm{sub}} \sin(\beta_{\mathrm{m}}) = n_{\mathrm{sup}} \sin(\alpha_{\mathrm{in}}) \pm m\lambda_{\mathrm{o}}/P \qquad \text{(Equation 2.82)}$$

where $m = 0, \pm1, \pm2 \ldots$ is the order of the diffracted wave and P is the period of the grating. n_{sub} and n_{sup} are the refractive indexes of the transmitted medium (substrate) and the incident medium (superstrate), respectively. β_{m} and α_{in} are the diffraction and light angles in the incident medium, respectively.[63,64] According to Equation 2.82, several mechanisms could take place that can play a central role in transmitting the incident light through the grating. At $\beta m = 90°$, for example, a so-called Rayleigh's anomaly appears, causing a change in the transmission spectrum of the incident light through the grating.[65,66] This can be attributed to the diffracted wave that propagates parallel to the grating.

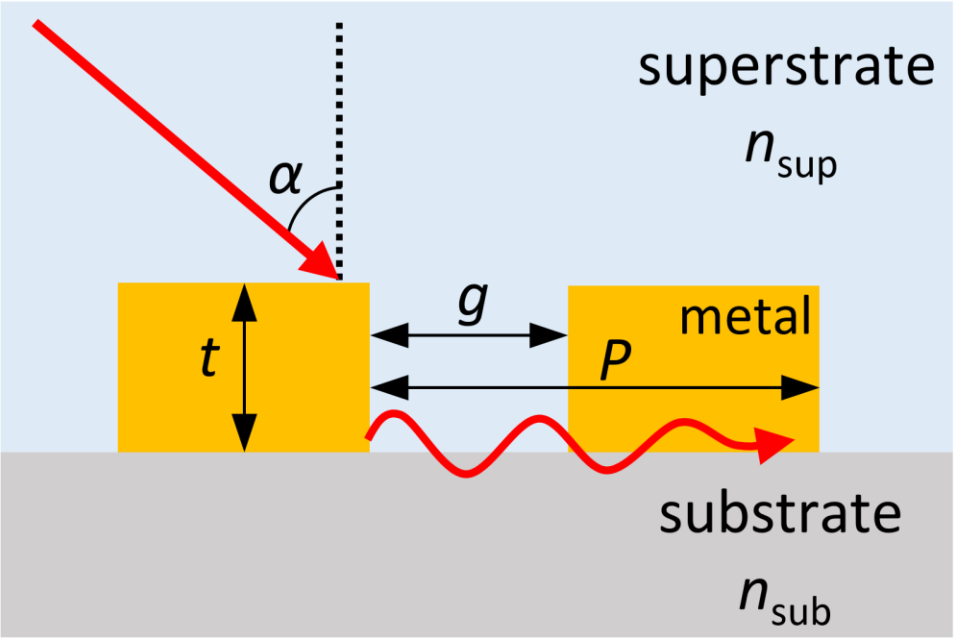

Figure 2.4.5. Scattering by nanograting structure.

Then, Equation 2.82 at the normal incidence can be written as:

$$P = m\lambda_0/n_{sub} \quad \text{(Equation 2.83)}$$

A zeroth diffraction order or higher order can be seen when $P < |m\lambda_0/n_{sub}|$ or $P > |m\lambda_0/n_{sub}|$, respectively. Equation 2.83 shows that at a particular wavelength, which is called "Rayleigh's wavelength", a diffracted wave emerges and propagates tangentially to the grating surface; it shows the dependence of this type of anomaly on three factors: P, λ_0, and n_{sub}.

A special case of SPPs supported by the periodicity of the metallic grating is called "Wood's anomaly" or "surface wave anomaly". This phenomenon can take place under one condition, which is given by Equation 2.84:

$$\mathrm{Re}(\mathbf{k}_{spp}) = \mathbf{k}_0 \sin(\alpha_{inc}) \pm mD \quad \text{(Equation 2.84)}$$

where $\mathrm{Re}(\mathbf{k}_{spp})$ and $D = 2\pi/P$ are the real values of the SPP and the grating wavenumbers, respectively.[67–71] Wood's condition becomes:

$$P = m\lambda_0/[(\varepsilon_{sub}\varepsilon_{metal})/(\varepsilon_{sub} + \varepsilon_{metal})]^{1/2} \quad \text{(Equation 2.85)}$$

where ε_{sub} and ε_{metal} are the permittivities of the dielectric and the metal, respectively. Abrupt trough and peaks in the transmittance spectrum versus the incident wavelength or the period at a particular angle of incidence can be noticed at both Rayleigh's and Wood's anomalies.[72]

Another mechanism that can enhance the transmission through the nanograting is called Fabry-Perot-like resonance. When the light hits a metallic nanostructure, opposite dipoles are generated at the top and bottom edges of the nanowires. These dipoles radiate wavelets inside the nanoslits; then, at particular wavelengths and wire thicknesses, a standing wave will form, causing dips in the reflection spectrum. Mainly, Fabry-Perot resonance depends on the depth of the grating (wire thickness, t) and the incident wavelength according to the Fabry-Perot resonance condition ($\lambda_N = 2t/N_{ro}$), where N_{ro} is the resonance order.[73–76]

The next transmission mechanism is called nanofocusing or funneling. This mechanism can support both SPPs and Fabry-Perot resonances. It works when the sidewalls of the nanostructure make an angle with the normal. It, in other words, works when the top opening slit of the nanostructure is greater than the bottom opening slit, Figure 2.4.6 (a).

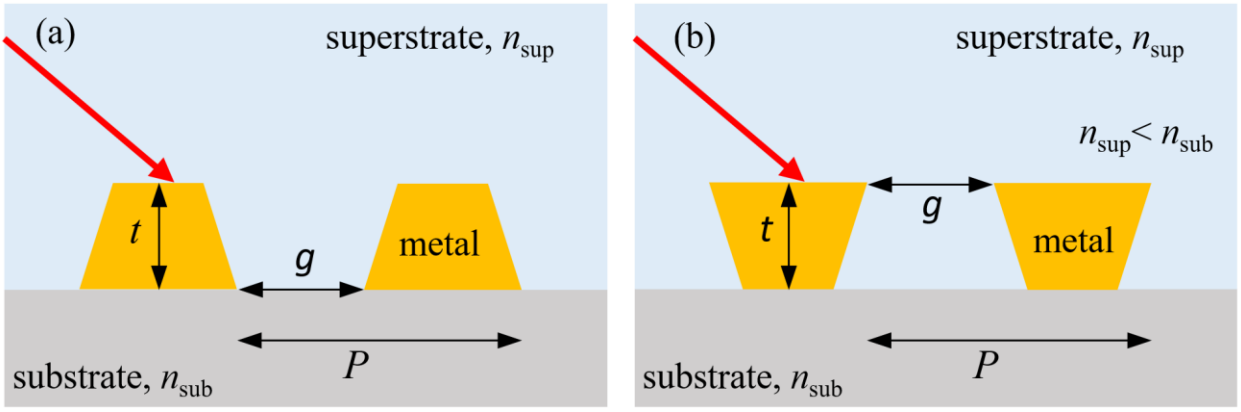

Figure 2.4.6. Taper angle nanograting, showing (a) the nanofocusing and (b) the impedance matching mechanisms.

The idea of this mechanism is that this type of taper angle can collect more light and funnel, focus, and confine it within a very small exit aperture (the bottom opening slit). This mechanism can enhance both the local electric field and the transmission.[77–81] The last mechanism of light transmission enhancement is called impedance matching. This mechanism occurs between the guided waves in the ultra-narrow linear nanoslits and the incident wave; it totally depends on the so-called Brewster angle (α_B), a particular incident wave angle at which total transmission can take place in the case of using dielectric nanograting or partial transmission in the case of using metallic nanograting. It could take place also when the taper angle structure is considered, Figure 2.4.6 (b). The figure shows that the small opening slit is located in the low refractive index medium and the large opening slit is located in the high refractive index medium. This mechanism very weakly depends on λ_0 and t; however, it may achieve a total transmission of a broadband light at α_B.[82–86]

2.5 Photodetectors types

Photodetectors (PDs) are devices that convert light into electrical signals. So, these devices can detect electromagnetic waves that range from gamma-ray to radio waves. Each region has a special type of photodetector that depends on the energy of the detected electromagnetic wave. This work focuses on the photodetectors which operate in the visible and infrared ranges (IR). Strictly speaking, most of the dissertation focuses on 875 nm of wavelength. Many types of photodetectors, such as p-i-n, avalanche, heterojunction, and MSM photodetectors can be used to detect the IR region, particularly at 875 nm.

In general, the devices that absorb light and generate electrical signals can be classified into two types: semiconductor and thermal photodetectors. In the thermal PDs, the absorbed light

increases the temperature of the material and hence the temperature is transferred via thermocouple phenomena into an electrical signal.[87] In the semiconductor PDs, however, the absorbed light interacts with electrons in the material and generates an electric current. Semiconductor PDs can be divided into two types: intrinsic and extrinsic PDs. In intrinsic PDs (pure semiconductors), photons are absorbed when their energies equal or exceed the energy gap of the semiconductor. Thus, electron-hole pairs, which produce a photocurrent after applying an external voltage, are generated. In extrinsic PDs, where semiconductors are doped with some impurities to increase the conductivity, photons are absorbed even if their energies are less than the energy gap of the semiconductor.[88]

Several types of optical PDs are used in various applications. For example, p-i-n PDs, avalanche photodiodes, heterojunction PDs, and metal-semiconductor-metal PDs (MSM-PDs) are the most widely used in communication systems.[87]

This section includes a very brief review of the first three types and a more detailed review for the last one. First, the p-i-n PD is a reverse biased p-n semiconductor junction. It consists of three regions: p-type, n-type, and intrinsic type between the n and p types. The advantage of the intrinsic region is to extend the electric field region (depletion region) that is generated by the p-junction and n-junction. Therefore, the depletion region will be elongated. The number of electron-hole pairs will increase because of an increase in the exposed substrate area. Second, is the avalanche PD that operates at high reverse-bias voltages. The quantum efficiency and response speed of these types of PDs are similar to those for non-avalanching PDs, but the major difference from the others is less noise. The APD is very sensitive and its sensitivity is ten times more than the sensitivity of the p-i-n PD. Third, is the heterojunction PD that consists of three layers of different kinds of semiconductors. The middle layer has a narrow-

bandgap, such as InGaAs, whereas the other layers have a wide-bandgap, such as InP. One of the most important advantages of these devices is the quantum efficiency, which is independent of the distance of the junction from the surface. On the other hand, the main disadvantage of the heterojunction PDs is the accumulation of charges at the interface that makes the device slow.

The last type is MSM-PD that is composed of two back-to-back connected Schottky diodes; one of the diodes is forward biased and the other is reverse biased, see Figure 2.5.1. A Schottky diode is composed of two metals deposited on a semiconductor substrate. Sugeta et al. in 1979 were the first who proposed the metal-semiconductor-metal photodetector (MSM-PD),[89] and the first fabricated MSM-PD was reported by Figueroa et al.[90] and Slayman et al.[91] and Wei et al. in 1981.[92] MSM-PD has many advantages. First, the cost of fabrication, which is considered as an important factor, is less than the other PDs. Moreover, since MSM-PD does not require doping, it is a high-speed device that has a low capacitance and low dark current.[92,93] In addition, MSM PD has low resistance that makes its time-constant RC extremely low. MSM PDs are important devices in fiber optic communication systems because of their characteristics compared with the other PDs. MSM PD is a planar device consisting of two pads and interdigital fingers that represent an active area with a semiconductor substrate, as shown in Figure 2.5.1 (c). Carrier generation, carrier transport, and contribution photocurrent in the external output signal are the three main steps that represent the operation of MSM PD.[94] When incident light hits the PD, the carriers (electron-hole pairs) are generated in the depletion region. The applied voltage makes the electrons and holes travel in opposite directions (opposite electrodes). The electrons and holes contribute to the current that flows into the circuit. Different types of substrates such as Si, SiO_2, and GaAs were used in this dissertation work, but the most focus was on GaAs. Gallium arsenide (GaAs) is the best compound semiconductor (group III-V) compared with other

semiconductors. GaAs has a wide direct bandgap of 1.4 eV.

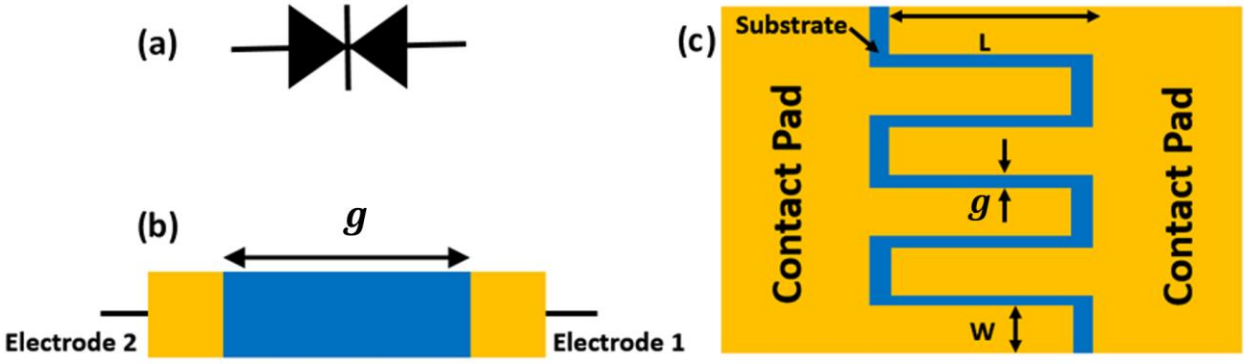

Figure 2.5.1. The basic structure of an MSM-PD.

In addition, GaAs has superb electron and hole transport properties that make it the major semiconductor in high-speed devices in communication systems. Moreover, GaAs operates in high response times. In PD devices, there is an important factor called the saturation velocity, which is the maximum velocity of the charge carriers (electron and hole) in a semiconductor. For GaAs, the saturation velocity is about 2×10^7 cm/s, which is very high compared to silicon and germanium semiconductors. Thus, GaAs is the best semiconductor substrate used in MSM PD fabrication.[60]

Nusir et al. (2015) reported that electrode spacing (d) of near-infrared based GaAs metal-semiconductor-metal photodetector has a significant effect on the optical intensity enhancement and photocurrent.[95] Although the electrodes were in microscale, one can notice a small effect of plasmons in the optical and electrical measurements compared with the nanoscale. Figure 2.5.2 (a) shows a relationship between the incident wavelength and the spectral response, S_R, for different d. In addition, Figure 2.5.2 (b)-(c) illustrate the relationship for both the experimental normalized peak of S_R and calculated photocurrent (I_{ph}) at wavelength = 875 nm. When d decreased, both the normalized S_R and I_{ph} have the same trend. Furthermore, the authors proved

that I_{ph} was five orders bigger than the dark current at a 5-volt bias. Finally, they showed that S_R depends on the polarization of the incident light by which plasmonic effects can be generated, Figure 2.5.3 (a)-(b).

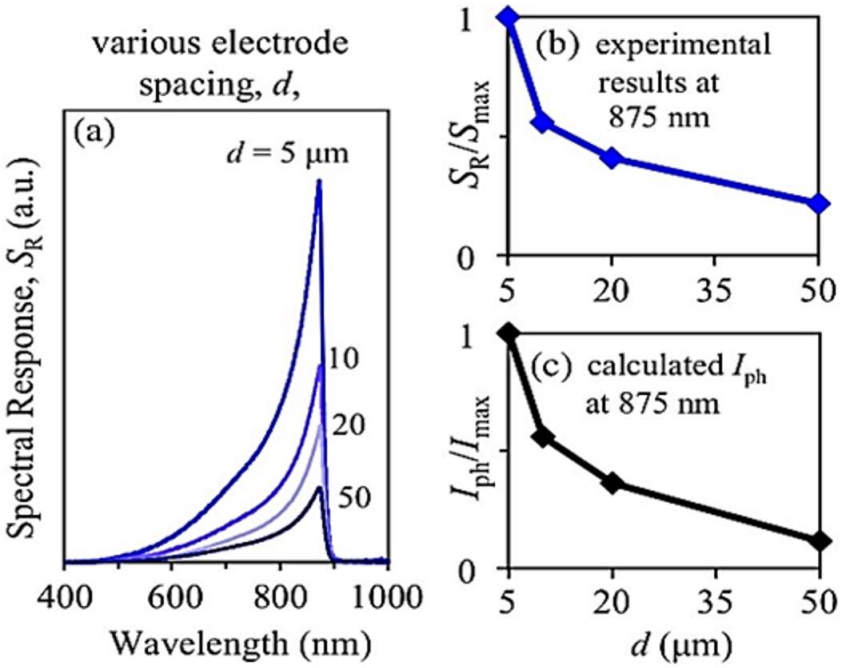

Figure 2.5.2. Experimental and computational spectral response vs. gap space and wavelength.[95]

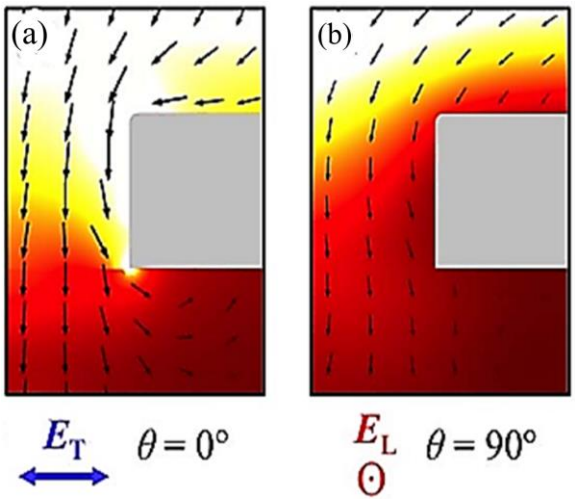

Figure 2.5.3. Computational electric field distributions under different light polarization.[95]

Karar et al. (2013) proposed a metal nanograting for a high plasmonic-based GaAs metal-

semiconductor-metal photodetector responsivity.[96] In addition, the authors demonstrated that the transmission enhancement of the incident light for this type of photodetector increased by plasmonic effects, which were generated by the coupling between the incident light and surface plasmon polaritons. The enhancement was seven times more than the enhancement in the conventional MSM-PDs at similar dimensions but less bias voltage (0.3 V).

Das et al. (2011) reported that the absorption enhancement factor of MSM-PD depends not only on the gap width between the nanogratings, but also on the shape of the grating.[97] Figure 2.5.4 and Figure 2.5.5 show various grating shapes, with different absorption enhancement factors.

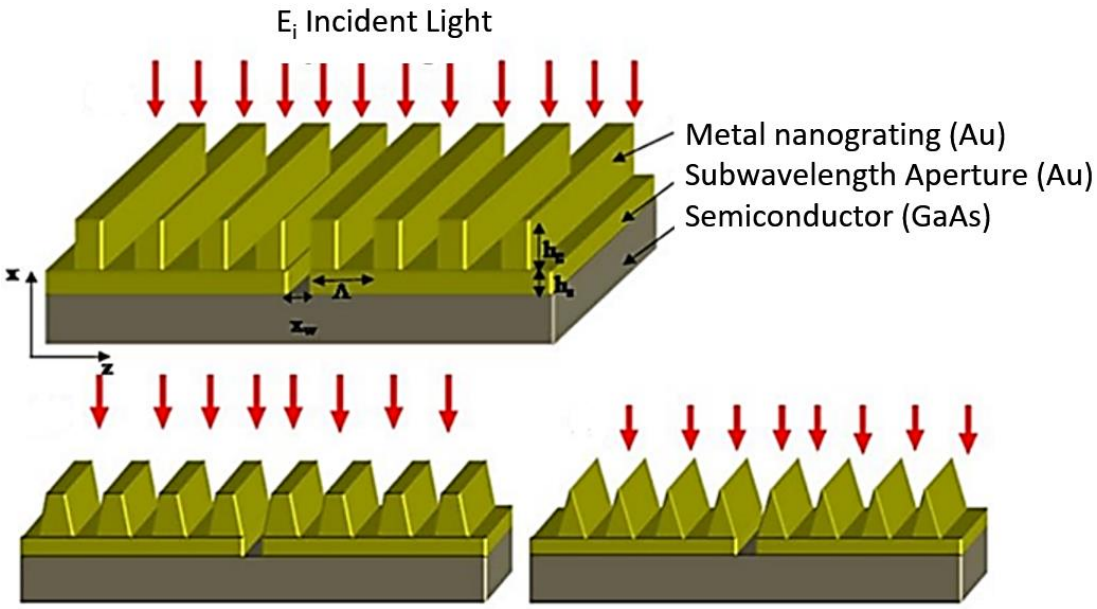

Figure 2.5.4. Different nanograting structures on GaAs and light absorption vs. wavelength.[97]

The authors investigated a rectangular-shaped and trapezoid-top to base length ratio nanograting. They found the rectangular-shaped nano-grating is better. Comparing with the conventional MSM-PD, the rectangular-shaped can increase the absorption enhancement factor to almost 50 times, but trapezoid-shaped can increase it over 30 times when the aspect ratio is

0.9. Furthermore, the enhancement factor significantly decreased with decreasing the aspect ratio (Figure 2.5.5).

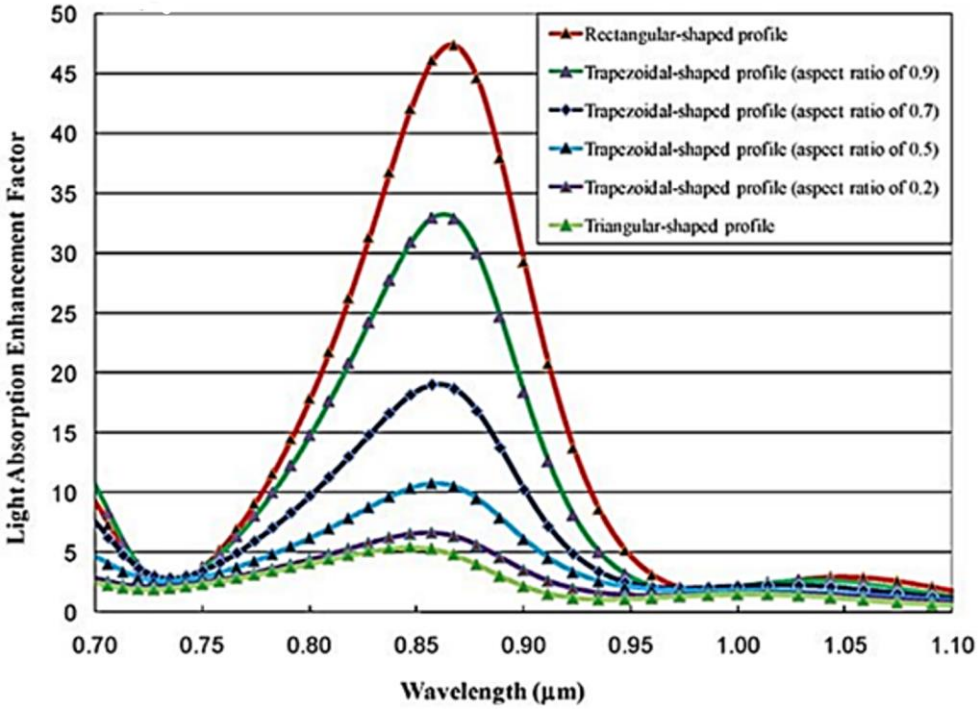

Figure 2.5.5. Absorption vs. wavelength for different aspect ratios.[97]

Tan et al. (2010) demonstrated that the optical enhancement of MSM-PD can be increased by employing double plasmonic nanograting structures.[98] This enhancement could reach to 25 times when compared to MSM-PD that have only a subwavelength gap and 1.6 times compared to the single subwavelength nanograting structure. The improved absorption factor is attributed to the bottom grating that distributes enhanced light through the subwavelength gap to a larger area substrate and metal interface.

Chapter 3.

METHODS

3.1 Electromagnetic models

All simulation models use a finite element method (FEM).[99] Two modules are used to design the models. These modules are Electromagnetic Wave, Frequency Domain (EWFD) and AC/DC Electric Current. Each module is accountable to conduct a specific calculation that relates to the desired output. EWFD, for example, is used to engineer and design the device and calculate the optical enhancements, such as local or near electric field, absorption, transmission, and reflection. However, AC/DC Electric Current is accountable to determine the electrical enhancement, such as the current density distributions. Figure 3.1.1 (a) shows an example of the designed model entities that were broken into very small mesh points, the finite elements of the method. The electric field at these mesh points is the calculated result of the model and is plotted in Figure 3.1.1 (b).

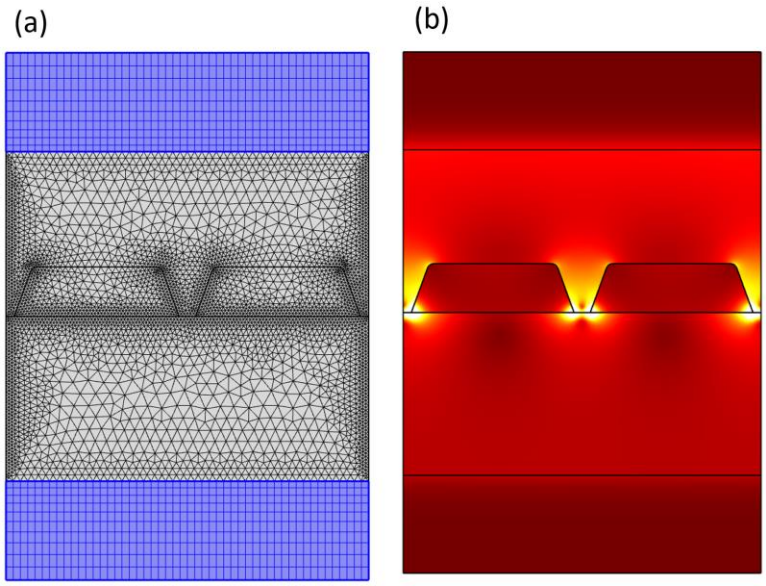

Figure 3.1.1. Meshed simulation space and electric field distribution.

In Appendix H, a detailed explanation of the FEM software usage is provided. These details give a good background of the software and start to build a desired model.

3.2 Fabrication steps

This section describes fabrication of some nanograting samples on different substrates and measuring the structure parameters such as wire width, wire thickness, gap space, and taper angle. The most common techniques in lithography are photolithography and electron beam lithography. According to Abbe's equation (Equation 3.1), photolithography is limited by the incident wavelength.

$$\mathrm{d_p} = \frac{\lambda}{2n\sin(\beta)} \qquad \text{(Equation 3.1)}$$

where $\mathrm{d_p}$ is the half aperture angle of the objective. Thus, photolithography is not useful for fabricating nano-gaps with ranges 50-250 nm or less for several reasons. From Equation 3.1, one can deduce that small $\mathrm{d_p}$, which represents minimum resolution, is desired. A small resolution requires short wavelengths, such as x-rays. X-rays have very high energies, and these energies make x-rays dangerous and hard to control with the conventional lens system. In addition, x-ray can damage samples and equipment.

The best candidate of the fabrication technique is the Electron Beam Lithography (EBL) technique. Instead of using the wavelength of light to obtain a high resolution of imaging and patterning systems, the wavelength of electrons can improve the resolution, thus better imaging and patterning. Equation 3.2 shows the relationship between electron wavelength and an accelerating voltage (V_{acc}).

$$\lambda_e = \frac{h}{\sqrt{2m_e eV_{\text{acc}}}} \qquad \text{(Equation 3.2)}$$

where λ_e is the De Broglie wavelength, h is the Planck's constant, m_e is the mass of electron and e is the electron charge. Equation 3.2 shows that electron wavelength depends on the accelerating voltage, which can be easily controlled. Many books include the detailed procedure of the (EBL) technique; however, following are the main steps, which are illustrated in Figure 3.2.1, with a brief explanation for each.

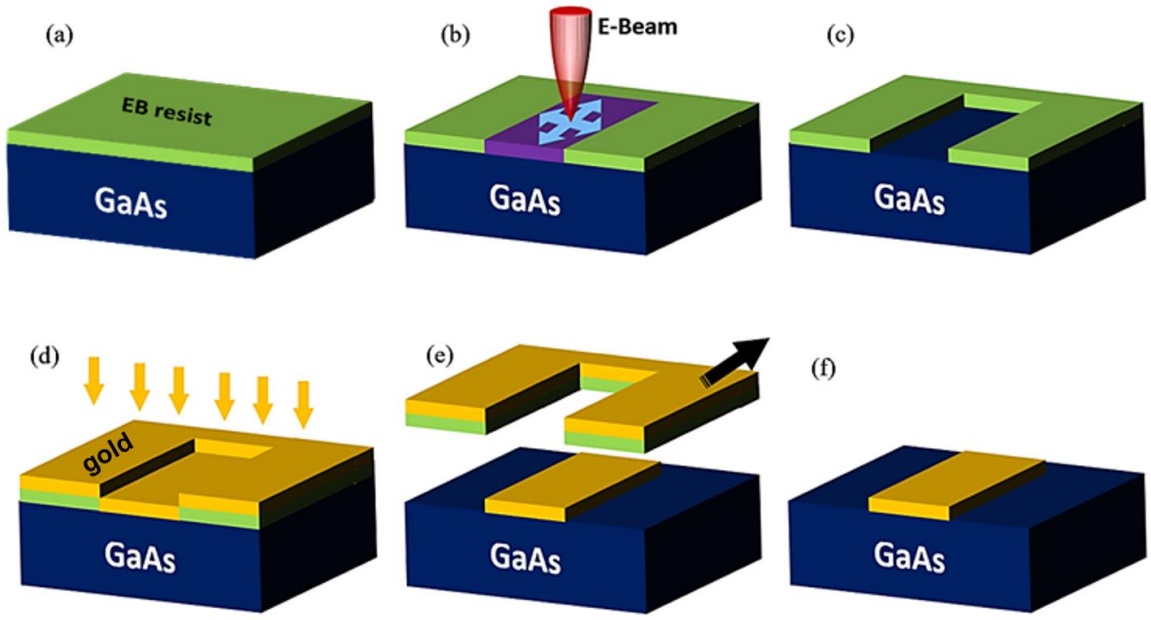

Figure 3.2.1. The main stages of EBL: (a) coating; (b) EBL; (c) developing; (d) evaporation; (e) lifting-off; and (f) desired pattern.

The first stage of the device fabrication starts with Design CAD, which is a software program used to define the desired pattern. Then, undoped GaAs substrate (the sample) is cleaned using an acetone and isopropanol (IPA) solution. Spin coating is used to coat the sample by polymethylmethacrylate (PMMA), which is the most common electron-beam-resist (EBresist) material for electron beam lithography, Figure 3.2.1 (a). A scanning electron microscope (SEM)

is used to make the pattern after uploading the Design CAD files, Figure 3.2.1 (b). Methyl-isobutyl-ketone (MIBK) with isopropanol (IPA) solution is a common developer that is used with PMMA. The developer will etch the exposed area, the area that is exposed to the electron beam, Figure 3.2.1 (c). Then, electron beam evaporation is used to deposit gold on the entire surface of the sample, Figure 3.2.1 (d). After that, acetone is used to lift off the photoresist and keep the desired pattern, as in Figure 3.2.1 (e) and (f). Figure 3.2.2 shows SEM images of the results of fabrication achieved in the lab. Figure 3.2.2 (a) shows several sets of a periodic grating of nanowires with different nano-gap space, whereas Figure 3.2.2 (b) shows one long set of nanowires that are separated by ~ 100 nm.

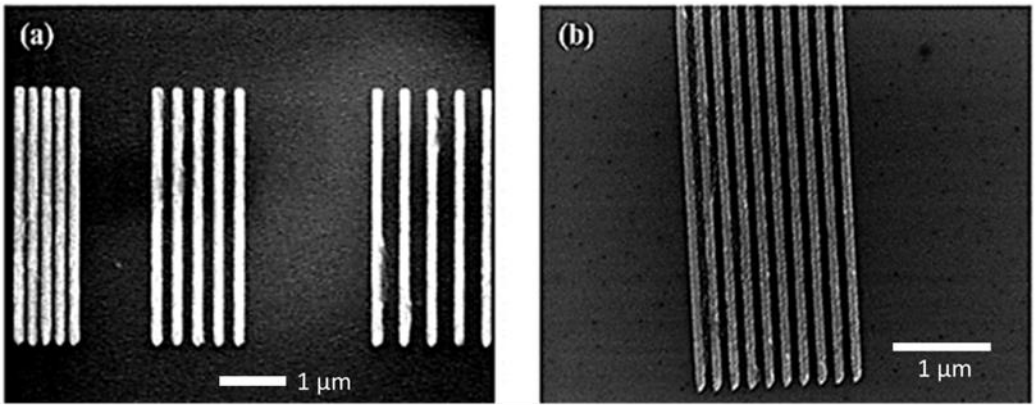

Figure 3.2.2. SEM 3D image of gold nano-wires with nano-gaps. (a) Nano-gap space is varied. (b) Nano-gap space is fixed.

Chapter 4.

OPTICAL ENHANCEMENT RESULTS

Optical enhancements of the proposed device were studied and are discussed in this chapter. These enhancements include several factors such as the enhanced near or local electric field, absorption, transmission, and reflection. The study covered the impact of the substrate material on the factors. This chapter is divided into three sections for SiO_2, Ti/SiO_2/Si, and GaAs substrates. In addition, the study contained the effect of the incident light frequency and angle, the thickness, the sidewall angle, and the width of the nanowires and the gap space on the mentioned factors.

4.1 Plasmonic nanogratings on SiO_2 substrate

A dual-width nanograting can be defined as a combination of two nanowire widths separated by nanogaps. Preliminarily, Figure 4.1.1 shows a 3D schematic of the dual-width nanograting structure with thickness, t, wire widths, w_1 and w_2, and period, P that is given by the following equation.

$$P = w_1 + w_2 + 2g \qquad \text{(Equation 4.1)}$$

COMSOL v5.1 was used to design and model a 2D structure. The cross-section of one period of plasmonic nanograting is shown in Figure 4.1.2 (a). The structure was composed of two gold nanowires separated by a nanogap, g = 5 nm, and surrounded by a real effective medium, n_{eff} = 1.25 that represents the average of the air and SiO_2 refractive indexes. Wire thickness was held constant at 15 nm. A p-polarized electric field, E_0, was simulated to perpendicularly strike the plasmonic nanostructure from the top. Perfectly matched layers

(PMLs) were applied to the top and bottom of the model to prevent the scattered electromagnetic waves from returning into the model space.

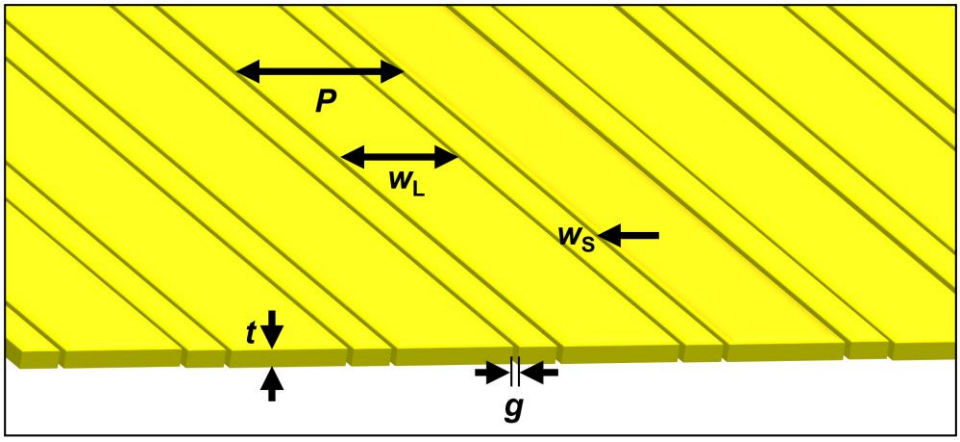

Figure 4.1.1. 3D structure of a dual-width plasmonic nanograting with a nano-gap spacing.[100]

A periodic condition was applied to the left and right sides of the model to generate an infinite repeating horizontal array, in the x-direction. An example of resulting enhanced electric field distribution with the incident wavelength, λ_0 = 700 nm, is shown in Figure 4.1.2 (b).

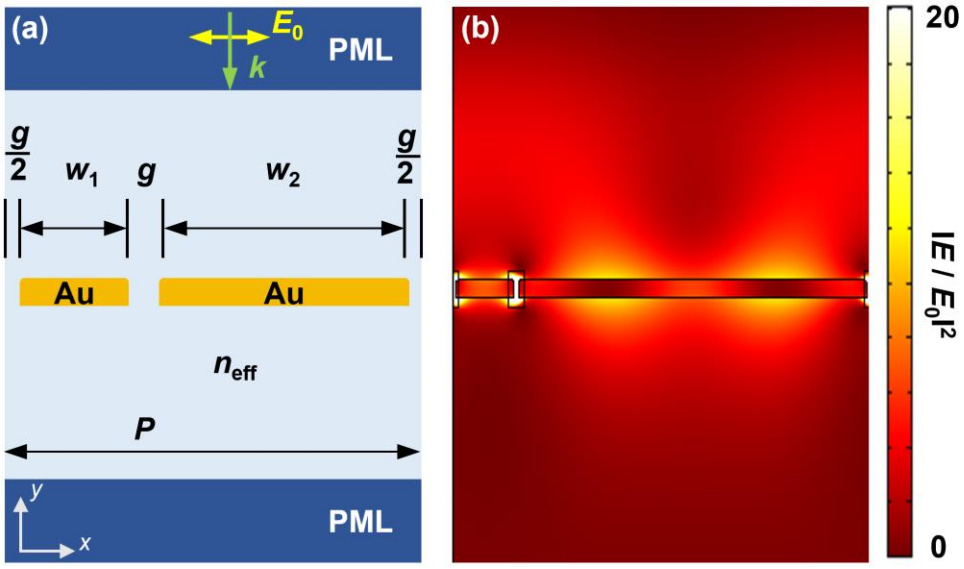

Figure 4.1.2. Cross-section view and electric field distribution of simulated plasmonic grating contains a single period of the dual-width structure.[100]

The small black box, including the gap space and the two wire inner edges, represents the desired area of the calculation. Optical enhancement, $\left(\frac{E}{E_0}\right)^2$, in this area was determined for wire combinations (w_1= 60 nm and w_2= 360 nm); it is defined as the ratio of the local enhanced electric field to the incident electric field all squared.[100] Figure 4.1.3 illustrates the simulation results that summed the near-field gap enhancement values, $\sum\left(\frac{E}{E_0}\right)^2$. The effects of dual-width nanograting structures on the optical enhancement have been studied. These studies included both $w_1$and w_2 as variables ranging from 10 to 250 nm with a step size of 10 nm for three different wavelengths, λ_0 = 600, 700, and 800 nm. The dashed white diagonal line in each figure represents the standard (single-width) nanograting structure, $w_1 = w_2$. The standard grating is defined as an infinite array of nanowires that have the same widths. The off-diagonal regions represent the dual-width nanograting structures, $w_1 \neq w_2$. Higher enhancement peak values appear at the edges of the maps (a) and (b). These values indicate that the dual-width structure can give better enhancements; they increase and shift while the incident wavelength increases. At λ_0= 700 nm, for example, interesting enhancement values appear when the wire widths are greater than 200 nm. Because of this, the calculations of the wire combinations were extended to 1 μm, as will be explained later.[100] To figure out the optical enhancement beyond the limits of the wire widths in Figure 4.1.3, the w range for the single-width structure (the diagonal) was extended to 1000 nm in 10 nm steps.

Figure 4.1.4 shows the plots of the optical enhancement as a function of w, for three different wavelengths, λ = 600, 700 and 800 nm. The enhancement is only dependent on w or P, as g and t were held at 5 and 15 nm, respectively. Three clear peaks, P_0, P_2, and P_4 are shown in each plot at different wavelengths. These peaks represent the optimum resonant wire widths or

period structures. From the plots in Figure 4.1.4, relationships were made between the enhancement peaks at optimum w vs. λ_0 and are represented in Figure 4.1.5.

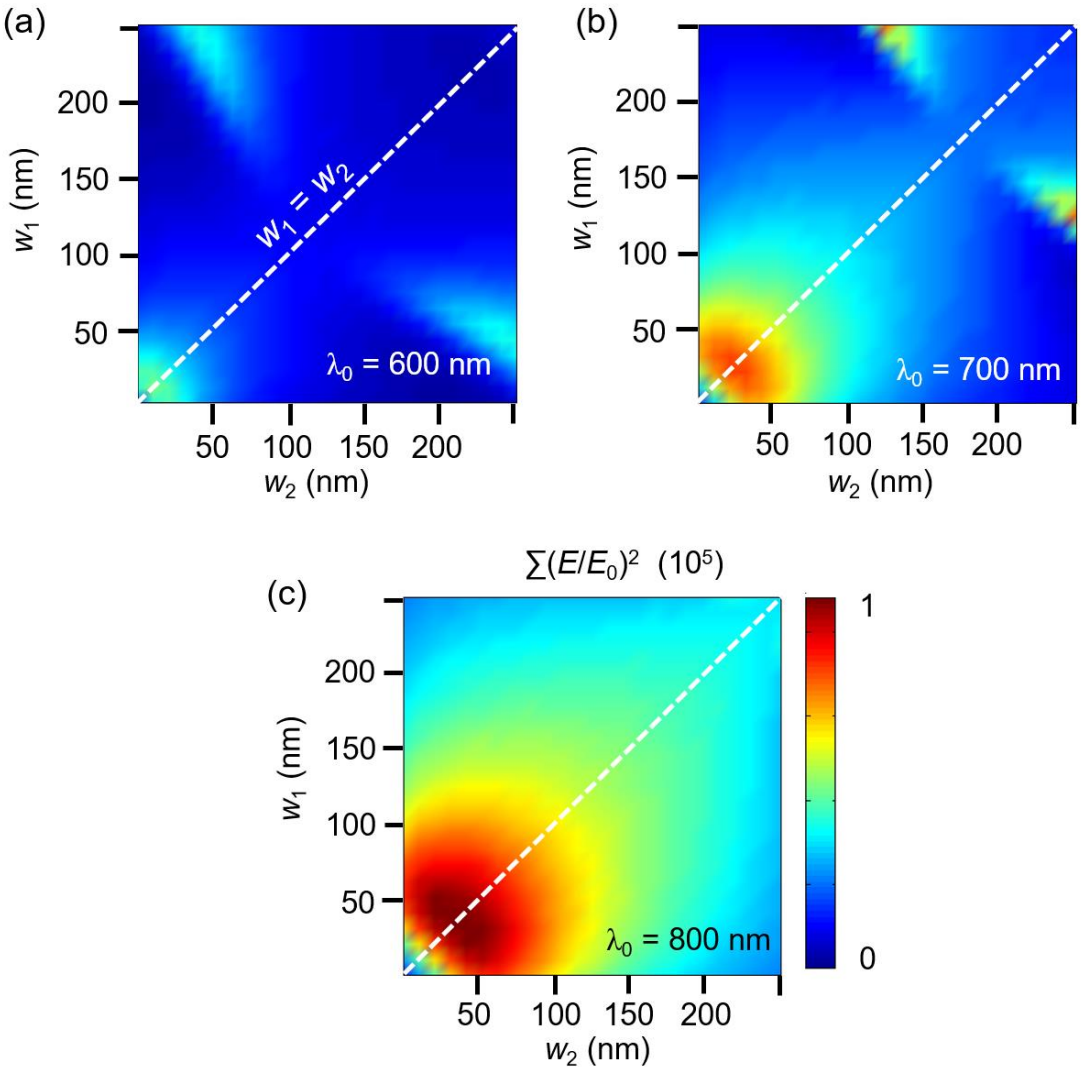

Figure 4.1.3. Electric field vs. w_1 and w_1 at different λ_0.[100]

These nearly linear relationships could be used to estimate the optimum wire width and incident wavelength for single-width structures.[100] Since several interesting peaks appeared in Figure 4.1.3 (b), $w_1$and w_2 ranges were extended up to 1000 nm and their enhancements were calculated as well. This can give a clear image of the enhancement of the nanograting structure that has a period beyond 250 nm. Figure 4.1.6 is the color map of the optical enhancement as a

function of w_1 and w_2 when λ_0, t, and g were set constant at 700, 15, and 5 nm, respectively.

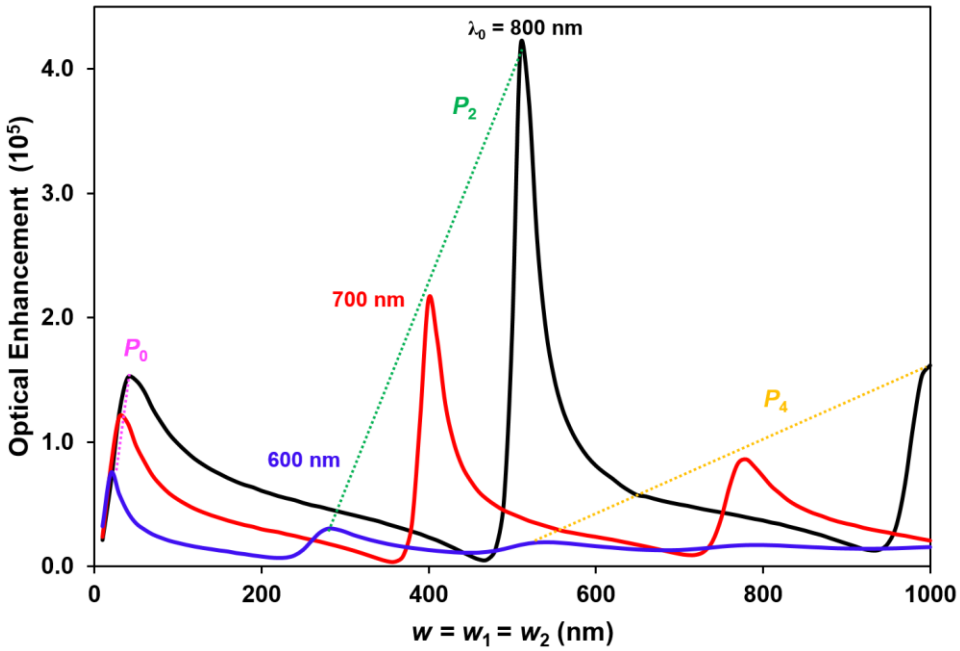

Figure 4.1.4. Optical enhancement vs. $w = w_1 = w_1$ at λ_0 = 600, 700, and 800 nm.[100]

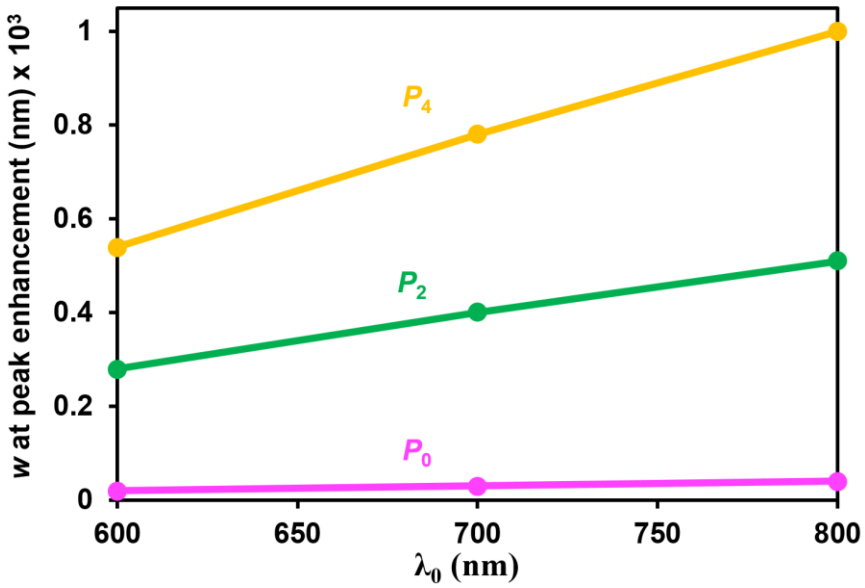

Figure 4.1.5. Resonant w vs. λ_0, corresponding to Figure 4.1.4.[100]

Different peak areas of enhancements are shown at different w combinations. Several

dashed white lines that have negative and positive slopes were plotted to determine the optimal wire widths and period, $P = w_1 + w_2 + 2g$. Again, the positive sloped diagonal line represents the single-width structure. This line represents the same plot in Figure 4.1.4 (red line). Three labeled peaks ($P_0, P_2,$ and P_4) are located at P = 90, 800, and 1540 nm, respectively. On the other hand, several labeled peaks (P_1 and P_3) showing off-diagonal (dual-width) are located at P = 430 and 1190 nm. The dashed lines, with a slope of negative one, represent the resonant periodic structures.

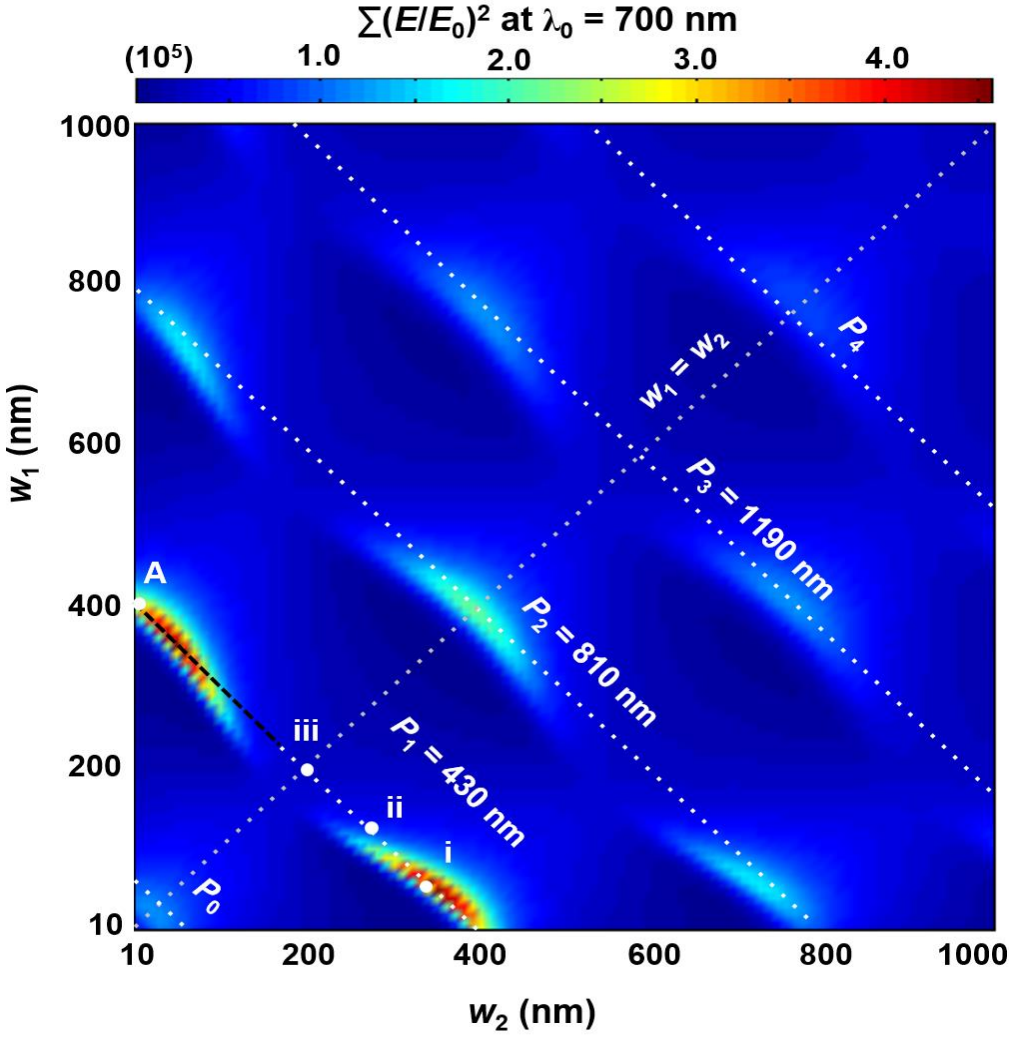

Figure 4.1.6. Color map of optical enhancement as a function of the wire widths, w_1 and w_2.[100]

Comparing the peak enhancement values for the single- and dual-width structures, the maximum values occur in the dual-width structure regions. The maximum value reaches 4.6 x 10^5 (w_1= 60 nm and w_2= 360 nm), which is more than double the maximum value, 2.1 x 10^5, for the single-width structure ($w_1 = w_2$ = 400 nm). According to the dual-width structure (Equation 4.1), the lines with negative slopes are given by Equation 4.2:

$$w_1 = -w_2 + (P - 2g) \qquad \text{(Equation 4.2)}$$

The slope here is -1 and the lines have constant P and g. These lines that have constant periods contain the maximum optical enhancement values, validating the importance of the dual-width structure in plasmonic nanograting. These periods are the optimum period length, P_n, for nanograting with this specific geometry. The optimum period lengths linearly increase with n as shown in Figure 4.1.7 (a).

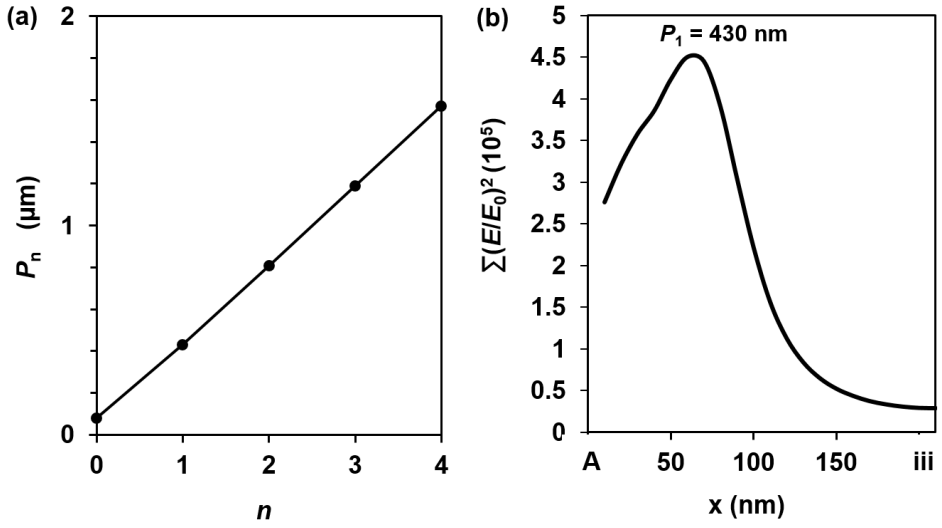

Figure 4.1.7. Optical enhancement data along P = 430 nm. (b) Period width vs. resonance number corresponding to Figure 4.1.6.[100]

This result confirms the importance of period in the plasmonic nanograting design.[101–105] Since the maximum value of the optical enhancement occurs in the dual-width region, the data is

extracted from the black diagonal line in Figure 4.1.6. These data represent the optical enhancement of the constant period, P = 430 nm, which are plotted versus the gap position from point A to iii, as shown Figure 4.1.7 (b).[100] Figure 4.1.8 shows the gap position for the dual-width structure; it is a function of w_1 and g. This structure is used to determine the highest value of optical enhancement at the resonant period.[100]

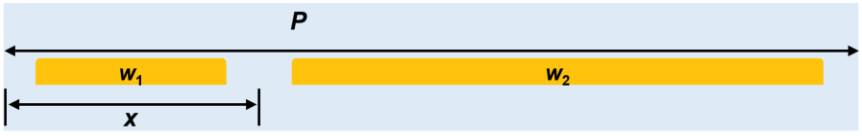

Figure 4.1.8. Cross-section view of the dual-width structure with a gap position, x.[100]

An enlarged view of the area in Figure 4.1.6 that includes the maximum optical enhancement is shown in Figure 4.1.9. It shows the highest value that occurs at w_1= 60 nm, w_2= 360 nm when λ_0 = 700 nm.[100] The optical enhancement was calculated for different wavelengths to find a relationship that connects them.

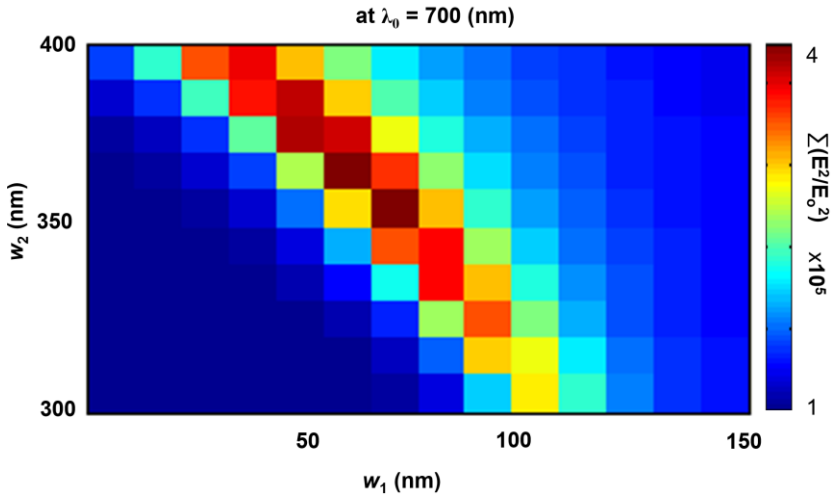

Figure 4.1.9. Enlarged view of the enhancement color map in Figure 4.1.6 for region i.[106]

It reveals that the optical enhancement increases linearly with λ_0, see Figure 4.1.10(a).

Figure 4.1.10 (b) shows the relationship between the incident wavelength, λ_0, and the wire widths, $w_1$and w_2. From these plots, two equations were made to determine the optimal wire widths at any particular wavelength in the range of 600-900 nm. These equations can be written as following:[106]

$$w_1 = 0.095\lambda_0 - 6.4 \qquad \text{(Equation 4.3)}$$

$$w_2 = 1.04\lambda_0 - 372 \qquad \text{(Equation 4.4)}$$

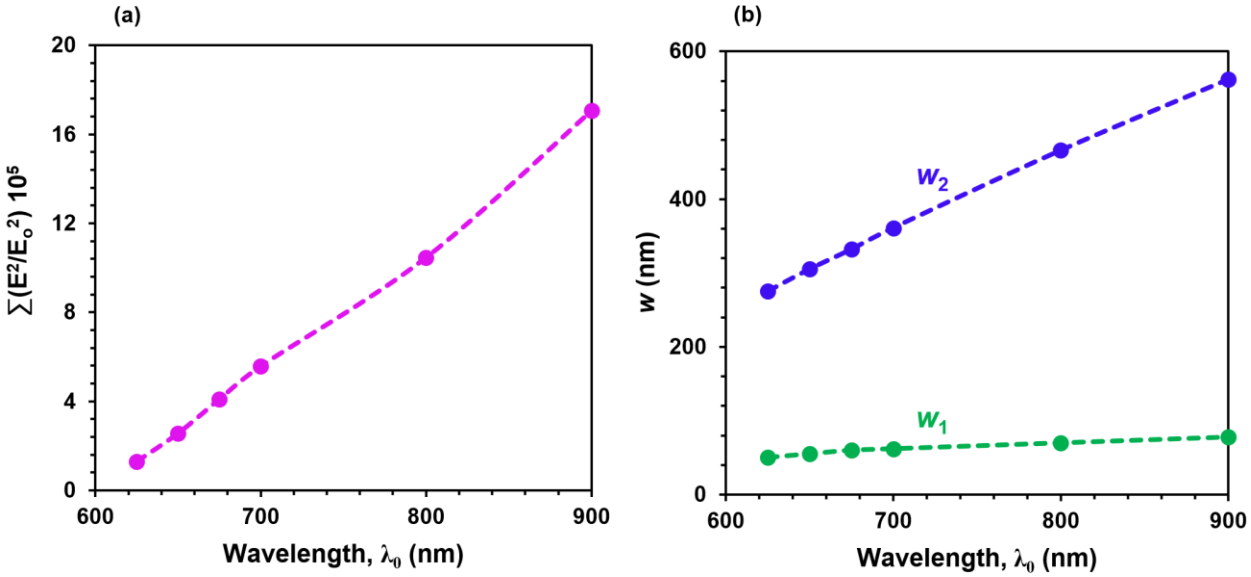

Figure 4.1.10. Plots of (a) enhancement and (b) *w* vs. λ_0.[106]

A new term, plasmonic wavelength (λ_P), should be defined here. This wavelength, represents the distance between two positive or negative regions on a structure surface and a function of the incident wavelength and geometric structure. To determine the natural plasmonic wavelength that corresponds λ_0= 700 nm, a Au slab with 5 μm width and 15 nm thickness was used as a non-periodic model structure. Figure 4.1.11 shows a zoomed (normalized) charge distribution on the slap surface; it shows λ_P= 363 nm that represents the distance between two

white adjacent area centers. This wavelength is very close to the width of w_2= 360 nm in the optimal dual-width structure.[100]

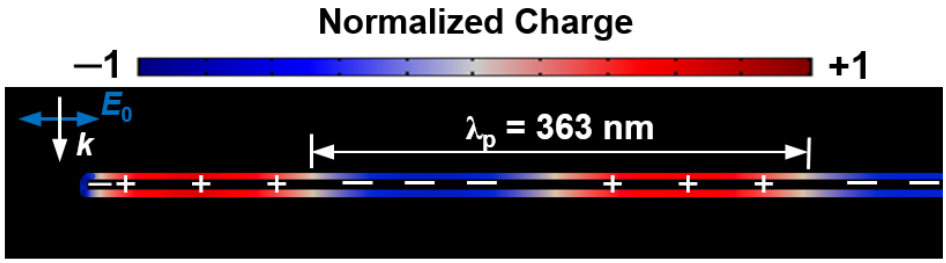

Figure 4.1.11. Charge distribution for non-periodic structure, illustrating plasmonic wavelength, λ_P.[100]

In the case of the single-width structure, a minimum enhancement is gained, (see Figure 4.1.4). This is due to the matching between the structure length and the plasmonic wavelength for all Au structures. This matching can reduce the fluctuation of the charges near the gaps, hence, minimize the enhancement in the gaps. In the case of dual-width structure, however, only one structure closely matches the plasmonic wavelength. This matching can increase the enhancement in the gaps when the optimum period is tuned. The optimum period can boost up the enhancement because of the coupling between the two nanowires in each period.

Three points were taken to illustrate the electric field and charge distributions at the resonant period, P = 430 nm, see Figure 4.1.12. These points are i (w_1= 60 nm and w_2= 360 nm), ii (w_1= 130 nm and w_2= 290 nm), and iii (w_1= 210 nm and w_2= 210 nm), as was shown in Figure 4.1.6. They represent the single-width (iii), the non-resonant dual-width (ii), and the resonant dual-width (i) structures, respectively. For the single-width structure (iii), each wire adopts a dipole mode, which couple to each other and enhances the electric field in the gap. This enhancement is very weak compared with the resonant dual-width structure at (i).

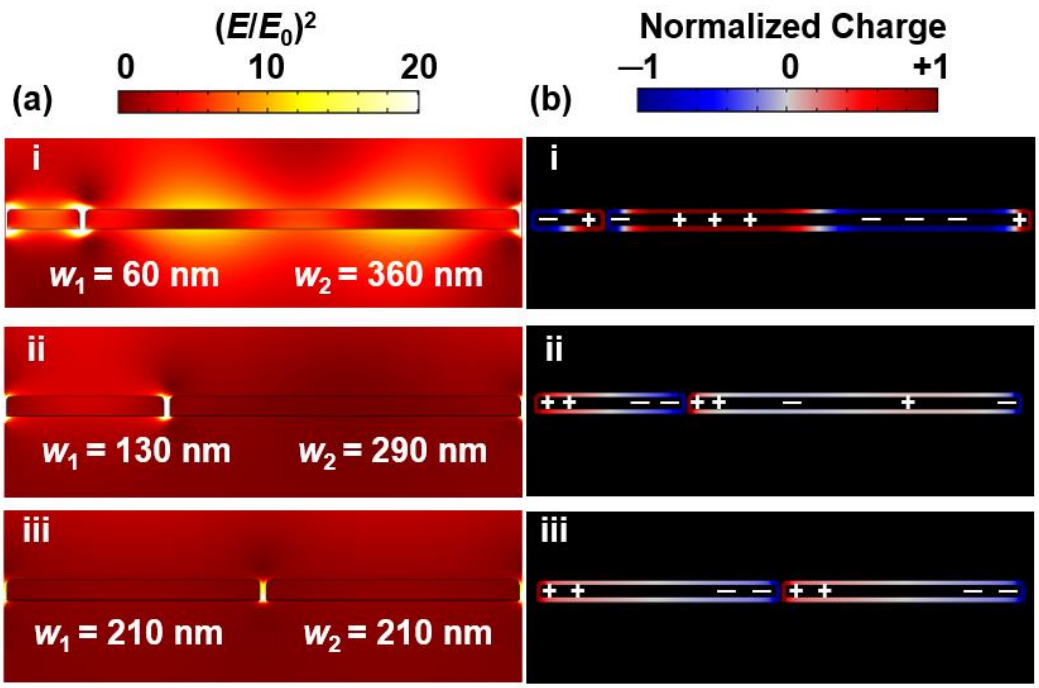

Figure 4.1.12. (a) Electric field and (b) charge distributions for i, ii, and iii regions, corresponding to Figure 4.1.6.[100]

This could be attributed to the strength of the generated dipoles, Figure 4.1.12 (a)iii and (b)iii. When the symmetry of the single-width is broken, a dual-width structure is produced. Then, different modes are generated that depend on the wire widths. In the case of the non-resonant dual-width structure (ii), the optical enhancement in the gap increases due to more charges accumulated at w_1 edges, Figure 4.1.12 (a)ii and (b)ii. In the case of the resonant dual-width structure (i), however, a hybridized grating plasmon is created between the two different widths, causing a very strong electric field in the gap space and on both wires surfaces, top and bottom.[26,100,107–109] This can be attributed to the charge distributions that generate a very strong dipole on w_1 and quadrupole on w_2, as shown in Figure 4.1.12 (a)i and (b)i.[100] In addition, the results show that the plasmonic grating depends not only on the period, but also on the wire widths of the nanostructure, w_1 and w_2, within the period. This is the advantage of the dual-width structure in the enhancement.

Figure 4.1.13 shows the optical enhancement peaks as a function of w_1 and w_2 at different wavelengths. This plot can help to determine the optimized wires widths combination at any particular wavelength that ranges from 625 to 900 nm.[106]

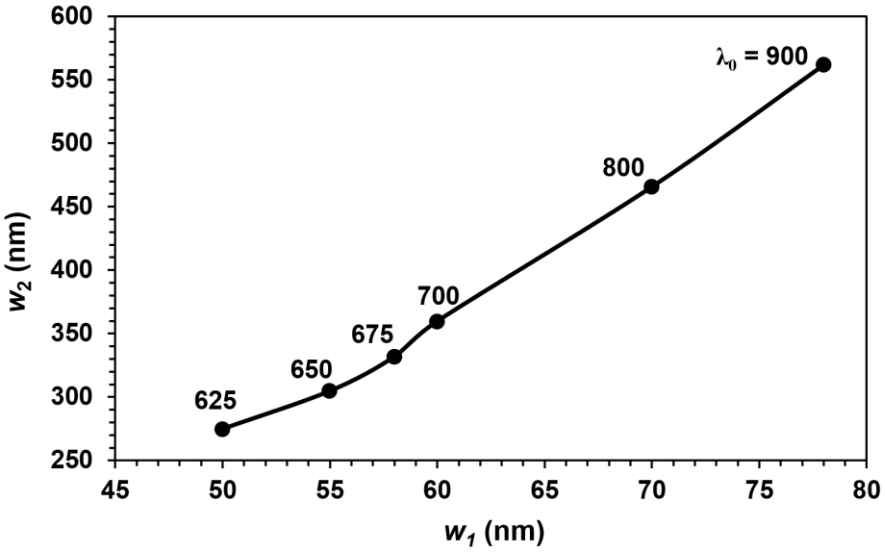

Figure 4.1.13. Plot of the peak enhancements for λ_0 vs. wire-widths, w_1 and w_2.[106]

Another important factor that can improve the light enhancement is the distance between the adjacent metallic nanowires.[110–113] However, it is important here to study the effects of the gap space on the enhancement. Three different gap spaces, g = 5, 20, and 50 nm, were tested to determine the enhancement peaks. At each gap width, the period was set constant at 430 nm. Then three conditions were studied. These conditions were as follows: full geometry (including both wire widths and the gap space), same geometry (with $w_1$removed), and same geometry (with w_2 removed), see Figure 4.1.14. Figure 4.1.15 shows the plots of the optical enhancement as a function of λ_0 for the three mentioned conditions. The figure is divided into three regions (i, ii, and iii) with various gap widths (g = 5, 20 and 50 nm), respectively. Each region includes the three geometries.

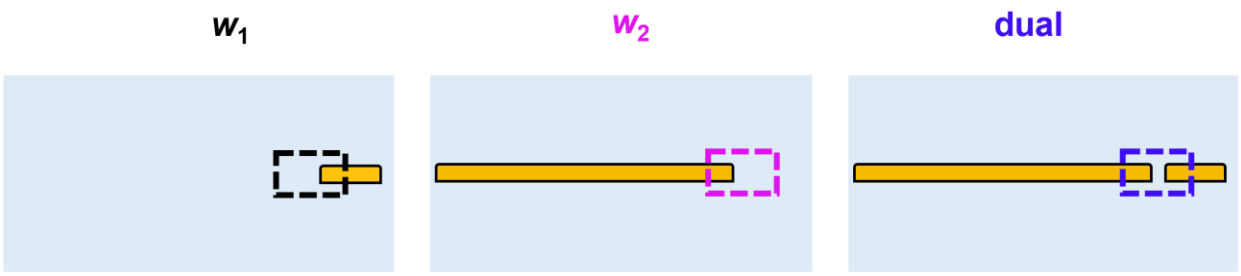

Figure 4.1.14. Single and dual-widths structure cross-sections.[100]

Figure 4.1.15 shows the plots of the optical enhancement as a function of λ_0 for the three mentioned conditions. The figure is divided into three regions (i, ii, and iii) with various gap widths (g = 5, 20 and 50 nm), respectively. Each region includes the three geometries.

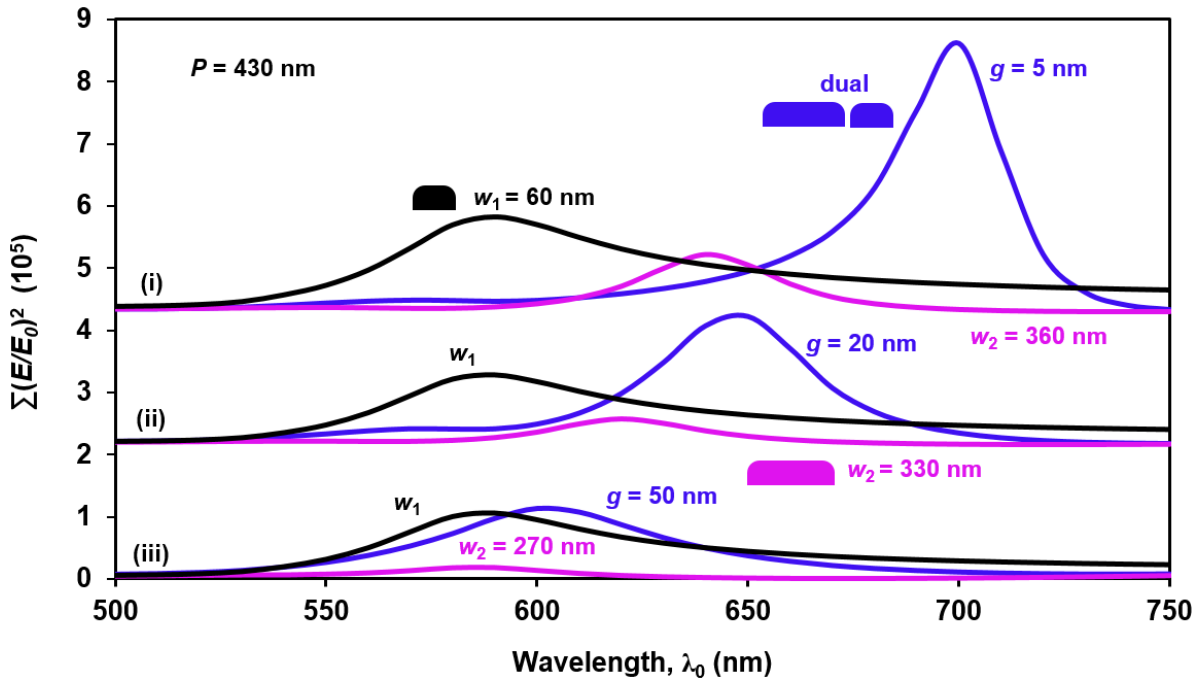

Figure 4.1.15. Optical enhancement vs. λ_0 for three different geometry structures.[100]

In region (i), three plots illustrate the enhancement curves for the dual-width structure (blue curve), w_1 and g structure (black curve), and w_2 and g structure (red curve). The same plots were repeated in the other regions (ii and iii) with a different gap space (20 nm and 50 nm),

respectively. For all curves and structures, one can notice that increasing g can reduce the enhancement. In addition, the maximum peak enhancement occurs with the dual-width structure. Again, these results proved and validated the importance of the dual-width geometry in the optical enhancement. In the case of the dual-width structure, increasing g not only reduces the peak enhancement, but also makes a blue shift in the peaks. When g = 5 nm, the resonant peak wavelength (λ_{peak}) is 700 nm.

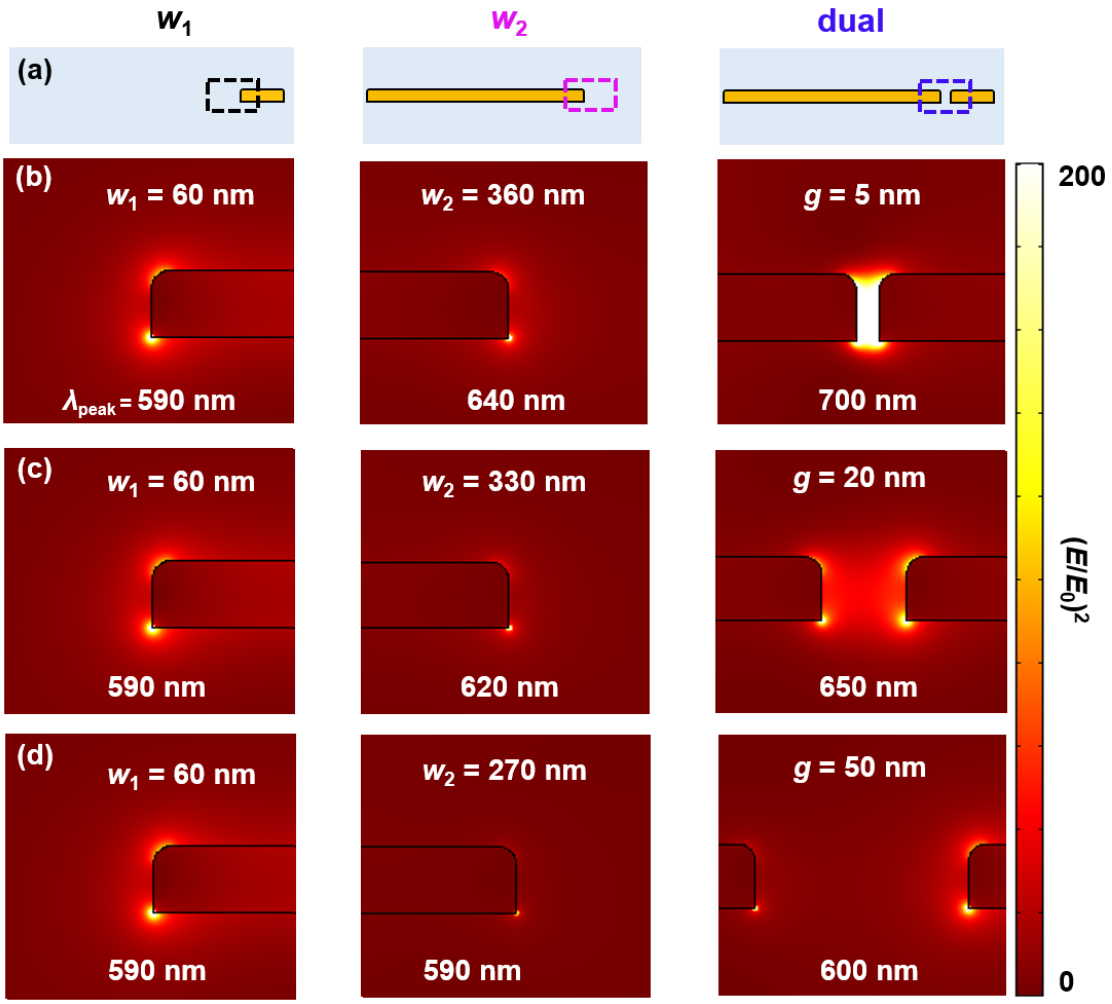

Figure 4.1.16. Electric field distribution at the peak enhancements, corresponding to Figure 4.1.15.[100]

However, λ_{peak} is 650 nm and 600 nm when g is 20 nm and 50 nm, respectively. The

same trend takes place when the structure includes only w_2. However, no peak shift appears when the structure contains only w_1. This could be attributed to the very small fixed w_1. Electric field distributions for the all structure cases are illustrated in Figure 4.1.16. They show the enhanced electric field in the gap and at the edges of the nanowires. Plots of the optical enhancement versus g for the dual-width structure are presented in Figure 4.1.17. The black curve represents the enhancement at the different peak wavelengths (λ_{peak}) at which the maximum optical enhancement is gained.

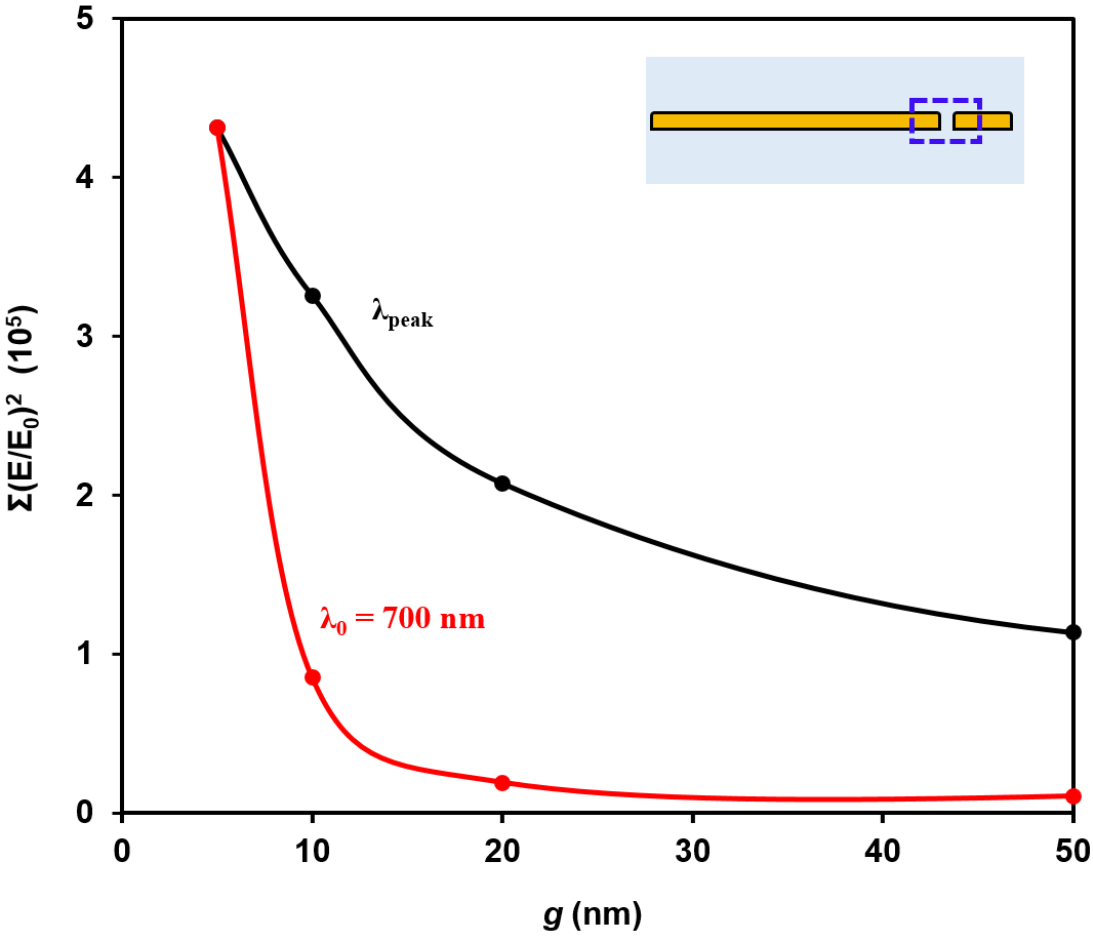

Figure 4.1.17. Plot of optical enhancement vs. g for dual-width structure.[100]

The enhancement increases 4 times when g decreases from 50 nm to 5 nm. The red curve

represents the enhancement as a function of g at λ_0= 700nm. The enhancement increases almost 40 times when g decreases from 50 nm to 5 nm. A new dual-width structure was designed and modeled on SiO_2 substrate and air superstrate, see Figure 4.1.18 (a). This structure was made to make a comparison with the n_{eff} model that was explained previously.

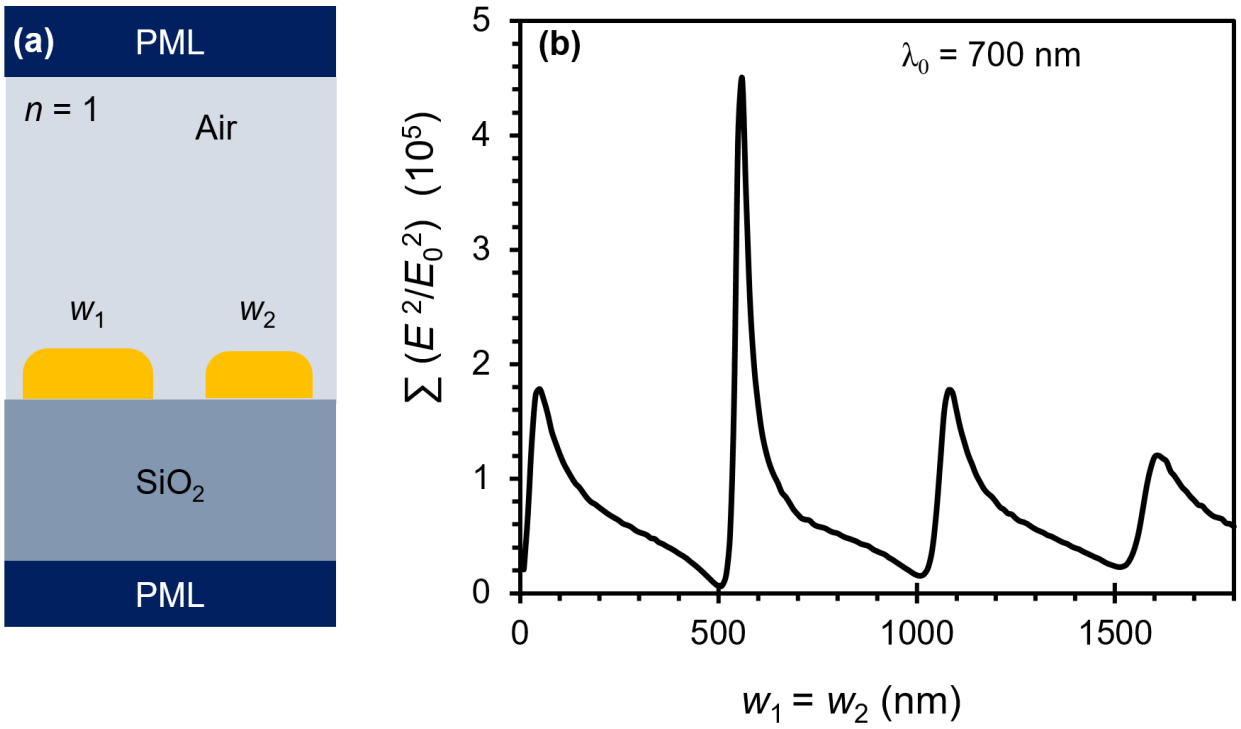

Figure 4.1.18. (a) Cross-section of the dual-width structure on SiO_2. (b) Optical enhancement vs. w_1 for the single-width structure.[100]

Figure 4.1.18 (b) shows the optical enhancement versus wire width (single-width structure), $w = w_1 = w_2$. The trend of the plot is the same as for the n_{eff} structure, see Figure 4.1.4 (red curve). Then, a color map was plotted to determine the optical enhancement for single- and dual-widths structures, see Figure 4.1.19. The color map is the same as for the n_{eff} structure, see Figure 4.1.6. The maximum value occurs in the dual-width region and it is 2.1 times larger than the maximum optical enhancement on the diagonal.

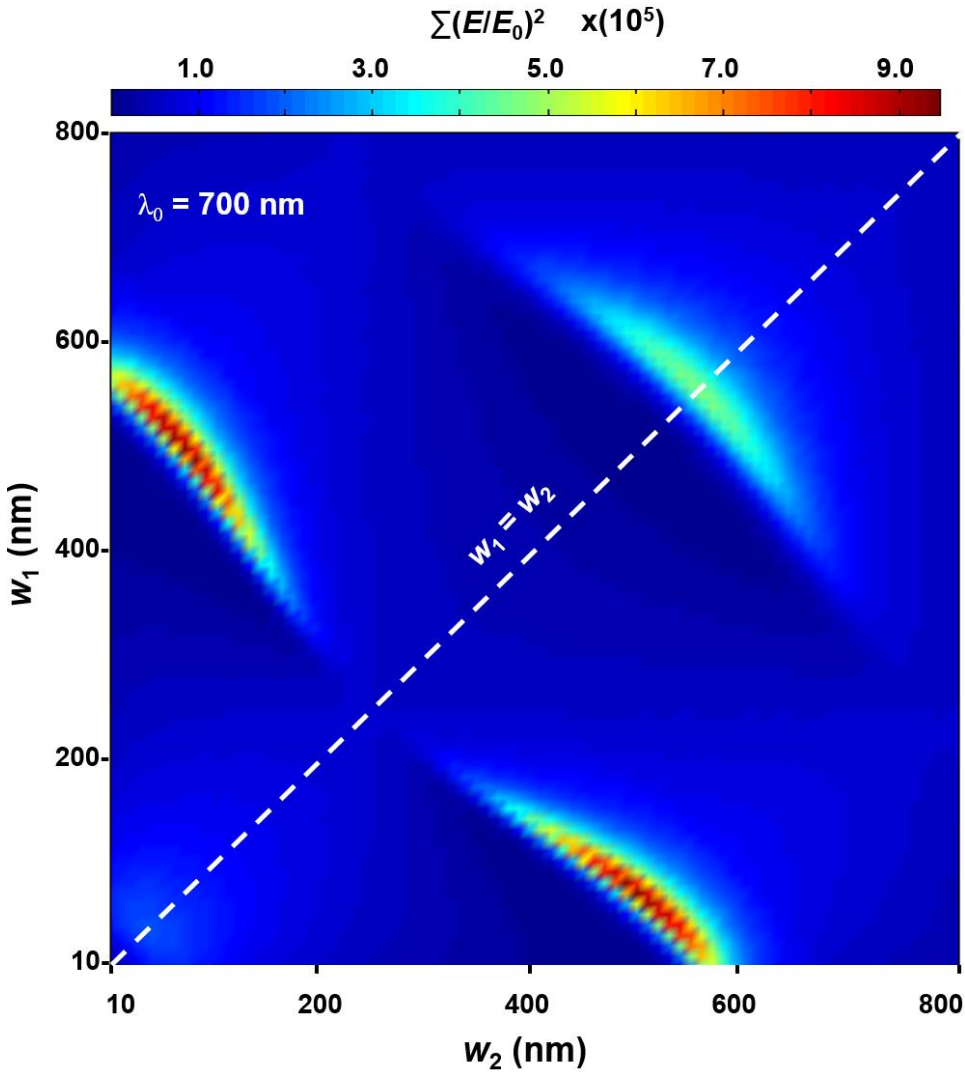

Figure 4.1.19. Optical enhancement color map of the proposed structure in Figure 4.1.18 as a function of wire-widths.[100]

4.2 Plasmonic nanogratings on Ti/SiO_2/Si substrate

The next plasmonic nanograting structure was built on a SiO_2/Si substrate, see Figure 4.2.1. In this section, the effect of SiO_2 thickness and Ti (titanium), which is used as an adhesive layer, on the optical enhancement were studied. For some plasmonic devices such as SERS, the optical enhancement was calculated on the surfaces of the nanostructures and the substrate. Figure 4.2.1 illustrates s 3D schematic sketch of the proposed device.

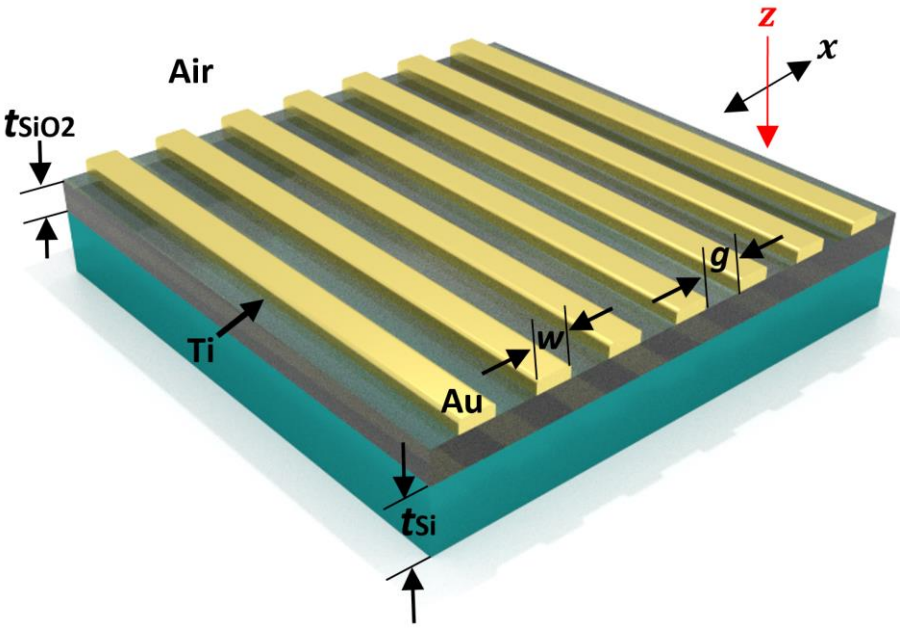

Figure 4.2.1. 3D schematic view of nanograting on Ti/SiO_2/Si substrate.[114]

A 2D model was designed by using COMSOL v5.3a. Figure 4.2.2 shows the cross-section view of the device; it consists of an infinite thickness of Si with a scalable SiO_2 layer. A thin layer of Ti was used to adhere the nanostructures, gold nanowires, with the substrate.[114]

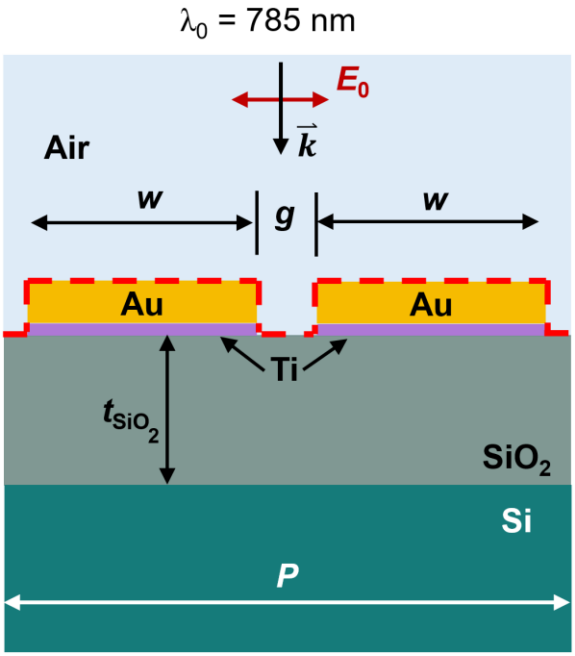

Figure 4.2.2. 2D simulation space.[114]

Figure 4.2.2 shows a single-width nanowire structure, w, with nanogap space, g. The incident wavelength, λ_0= 785 nm, was used to perpendicularly propagate on the structure with p-polarization. An example of the resulting electric field distributions for different wire widths, w = 50, 200, and 400 nm, at t = 15 nm, t_{Ti} = 1 nm and g = 10 nm, are shown in Figure 4.2.3. It shows how the enhanced electric field intensity, especially in the gap space, depends on w.[114]

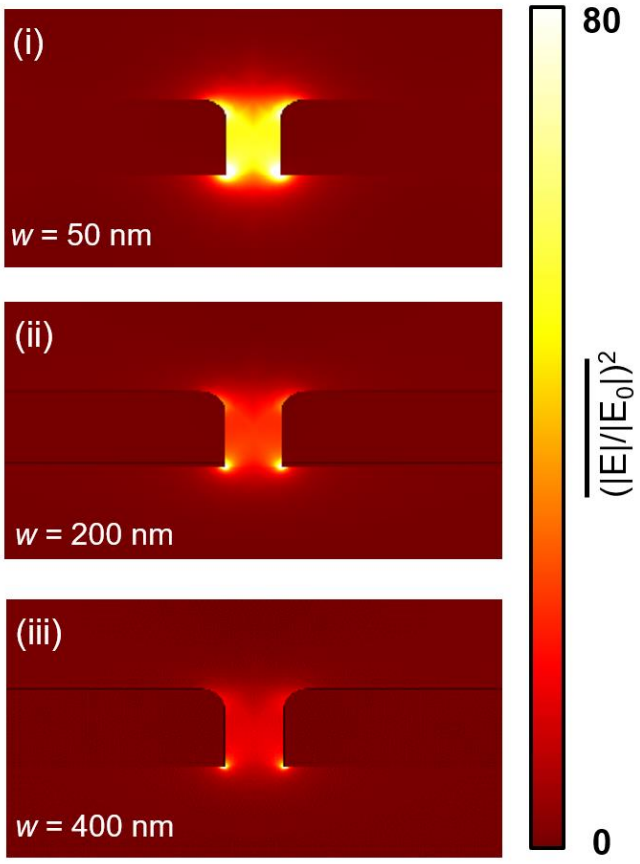

Figure 4.2.3. The electric field distributions for different w on Ti/SiO_2/Si and g = 10 nm.[114]

The average optical enhancement color map as a function of t_{SiO2} and w for the standard single-width structure is shown in Figure 4.2.4 (a); it was calculated in the gap space by taking the integration area. The width was swept from 20 to 250 nm in 10 nm steps; whereas, t_{SiO2} was swept from 0 to 800 nm in 10 nm steps.

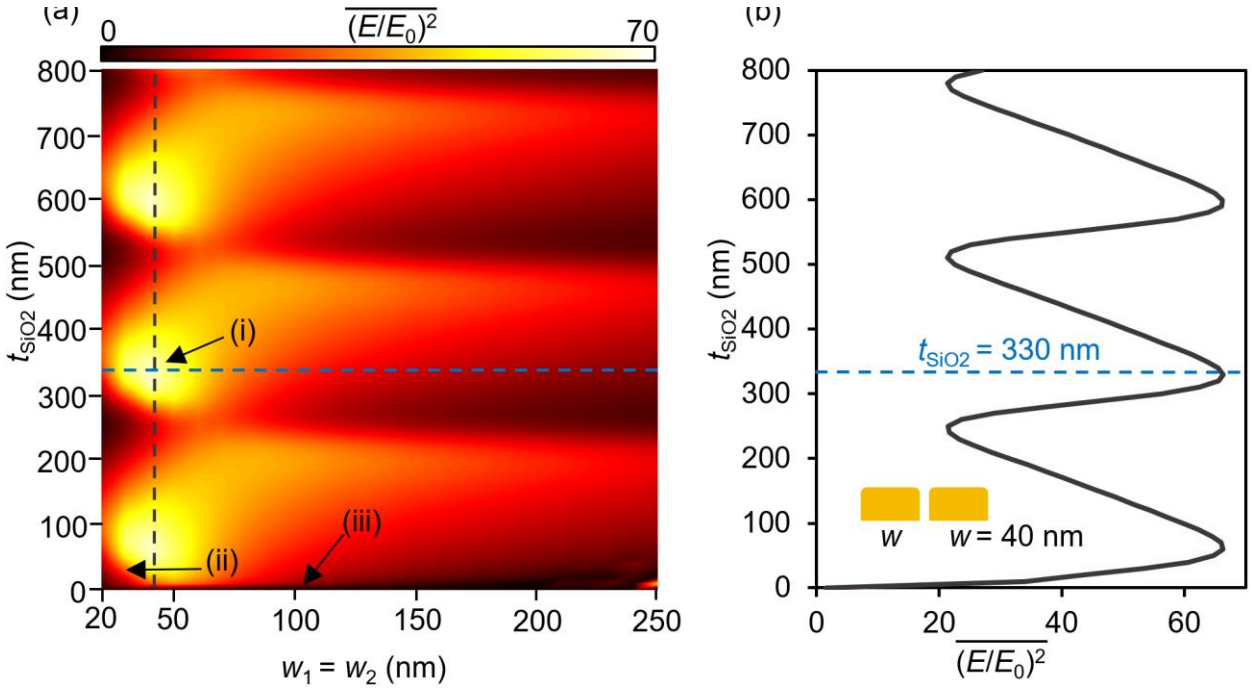

Figure 4.2.4. Average optical enhancement as a function of w and t_{SiO2}.[115]

The vertical dashed black line in the color map reveals the optimum w at which the maximum optical enhancement was gained. Three peaks of the enhancement appear in the color map. They occur at a constant wire width, w = 40 nm, and at different oxide thicknesses, t_{sio2} = 60, 330, and 600 nm. From the result, an optimum oxide thickness equation can be written as follows:

$$t_{(SiO2)_m} = m\ (270\ \text{nm}) + 60\ \text{nm} \qquad \text{(Equation 4.5)}$$

where m = {0,1,2…}. The periodic regions that appear in the color map are attributed to the thin film (oxide layer) interference effects.[115] The maximum peak of the enhancement is located at the intersection of the vertical and horizontal dashed lines, where w = 40 nm and t_{SiO2} = 330 nm. Three spots, the maximum enhancement peak and optimum geometry (i), median enhancement (ii), and minimum enhancement (iii), were indicated on the color map. Figure 4.2.4 (b) is the plot

of the average optical enhancement as a function of t_{SiO2} at the constant optimum wire width, w = 40 nm. Figure 4.2.5 illustrates the electric field distributions at the three spots. The averages of optical enhancement were calculated across the entire device surface rather than near field regions (gap space).

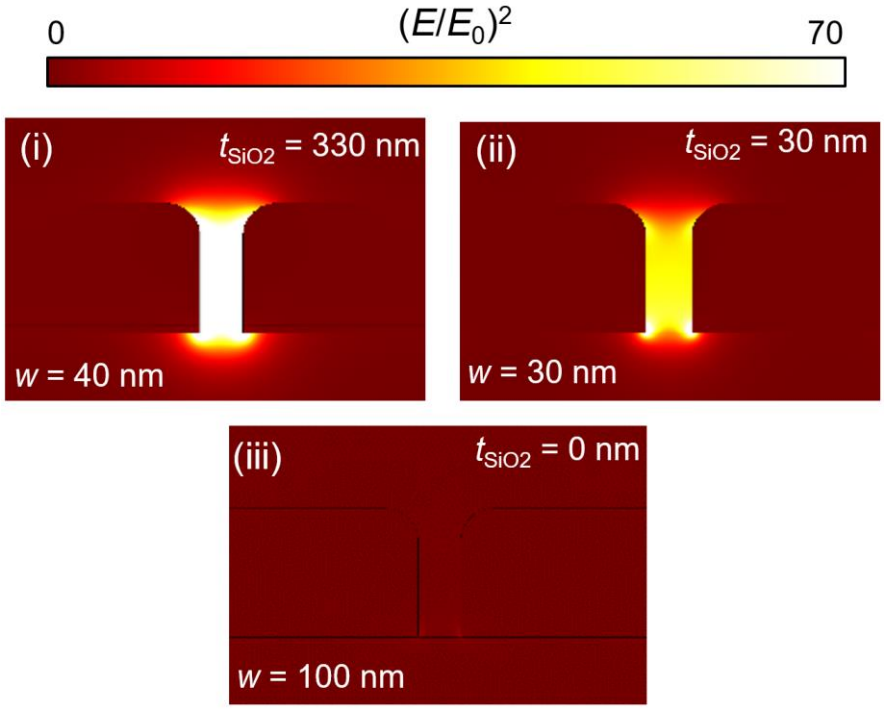

Figure 4.2.5. Electric field distributions at (i), (ii), and (iii).[115]

This technique can give a clearer estimation of the sensor response. Figure 4.2.6 shows the average enhancement along the line of the entire surface as a function of w. The electrode spacing was set constant at g = 10, 50, 100, and 500 nm and w was swept from 10 to 600 nm with 10 nm steps at each value of g. The optimized t_{SiO2} was held constant at 330 nm.[115] The average line of the enhancement decreases with increasing the gap space but only in the range of w less than 400 nm. In addition, a shift in the peak enhancement appears toward larger w with increasing g. This result ensures that smaller wire width generates more enhancement. However,

there are more additional plasmonic resonance modes, with less magnitude, appearing at higher w.[114]

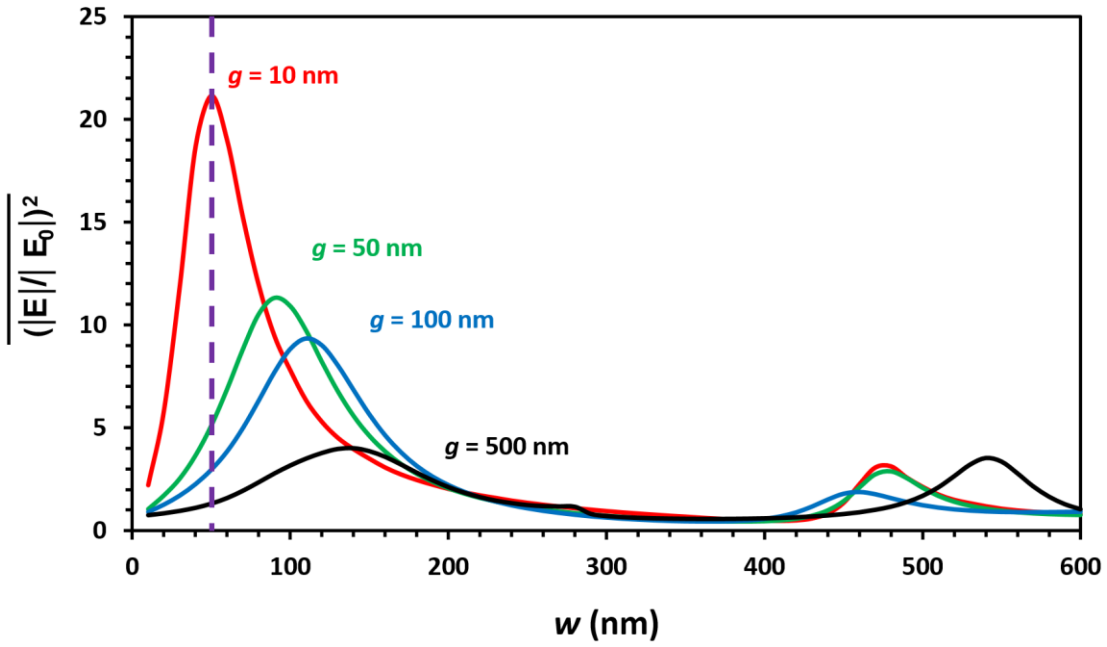

Figure 4.2.6. Surface average enhancement as a function of w for different g values.[114]

Two color maps and plots, showing the optical enhancement across the entire surface of the nanostructures and substrate as a function of w, g and t_{SiO2}, are illustrated in Figure 4.2.7. Figure 4.2.7 (a) exhibits the relationship between w and g when they both are swept from 10 to 600 nm in 10 nm steps, with t_{SiO2} = 200 nm. The highest value of the enhancement occurs at (i), w = 70 nm and g = 10 nm. This result is expected because smaller gap produces more enhancement. However, the interesting thing is additional plasmonic modes appear at higher w and g. These plasmonic modes occur at w = 150 nm and g = 320 nm, which correspond to the second highist enhancement region (ii). This result can allow for more accessibly fabricated devices since w and g have large values. Plus, the result shows that increasing w or g do not always decrease the optical enhancement.[114] The white dashed line with a slope of -1 represents

the additional plasmonic modes that generate from the matching of the periodic structure and the incident wavelength.[100] The (iii) arrow, with w = 200 nm and g = 200 nm, shows the standard fabrication capabilities. Figure 4.2.7 (c) is the color map for the same structure parameter values in (a) but with optimal t_{SiO2} = 330 nm.

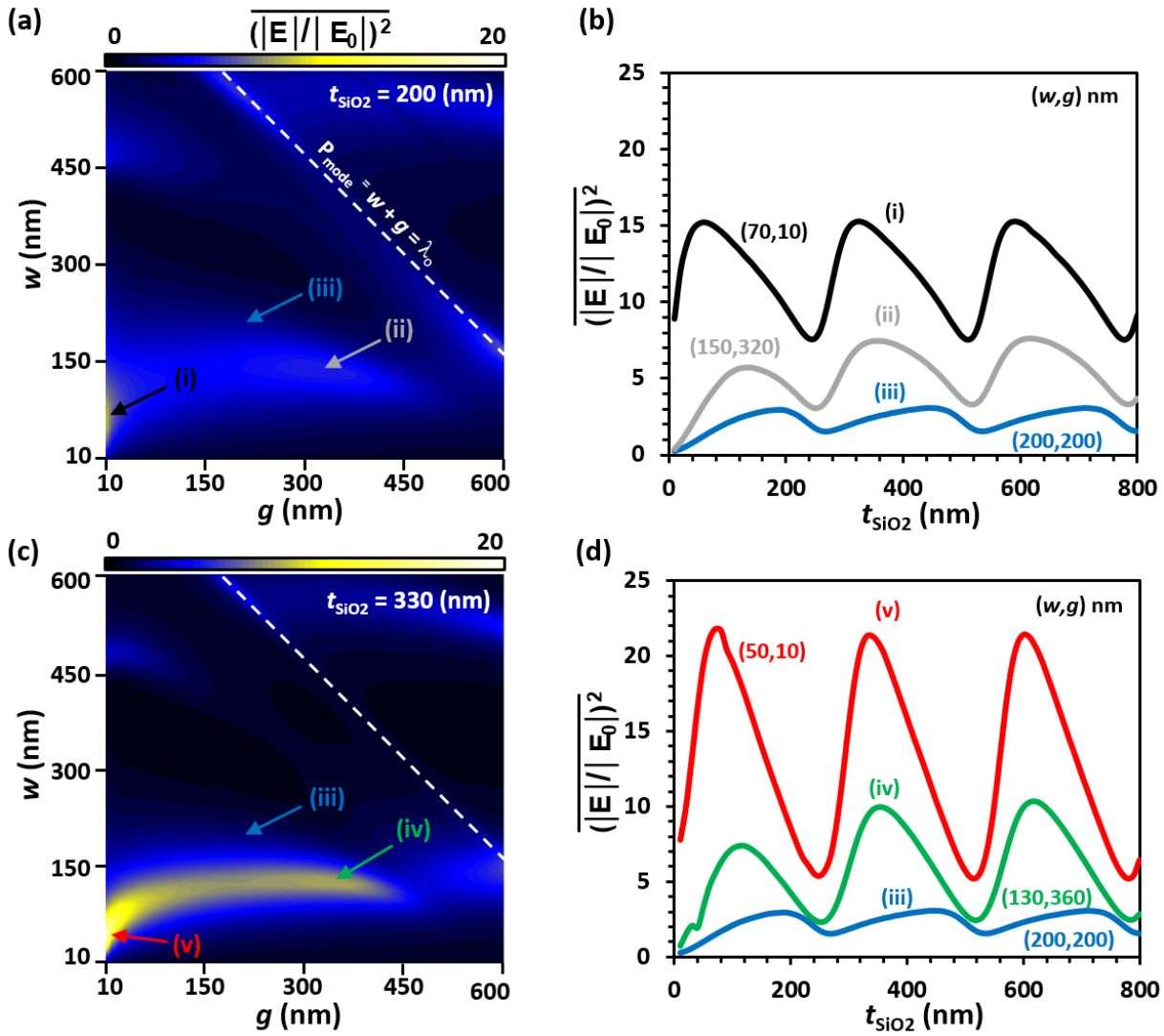

Figure 4.2.7. Surface average enhancement color map as a function of w, g, and t_{SiO2}.[114]

It shows that the enhancement can increase when the optimal t_{SiO2} layer is used. Plus, the optimum enhancement values slightly shifted from w = 70 nm and g = 10 nm at arrow (i)

and w = 150 nm and g = 320 nm at arrow (ii) to w = 50 nm and g = 10 at arrow (v) and w = 130 nm and g = 360 nm at arrow (iv), respectively. It is a good idea to test t_{SiO2} with the optimum structure parameter values to ensure that the structure is optimized. Figure 4.2.7 (b) and (d) show the plots of the average line enhancement as a function of t_{SiO2}, which was swept from 10 to 800 nm. For both plots, some periodic regions of constructive and destructive interference appear that depend on t_{SiO2} and λ_0.

The resonant t_{SiO2} is located at 60, 330 and 590 nm. Figure 4.2.8 shows three color maps of the average enhancement as a function of w and g for t_{SiO2} = 330, 290 and 250 nm. These

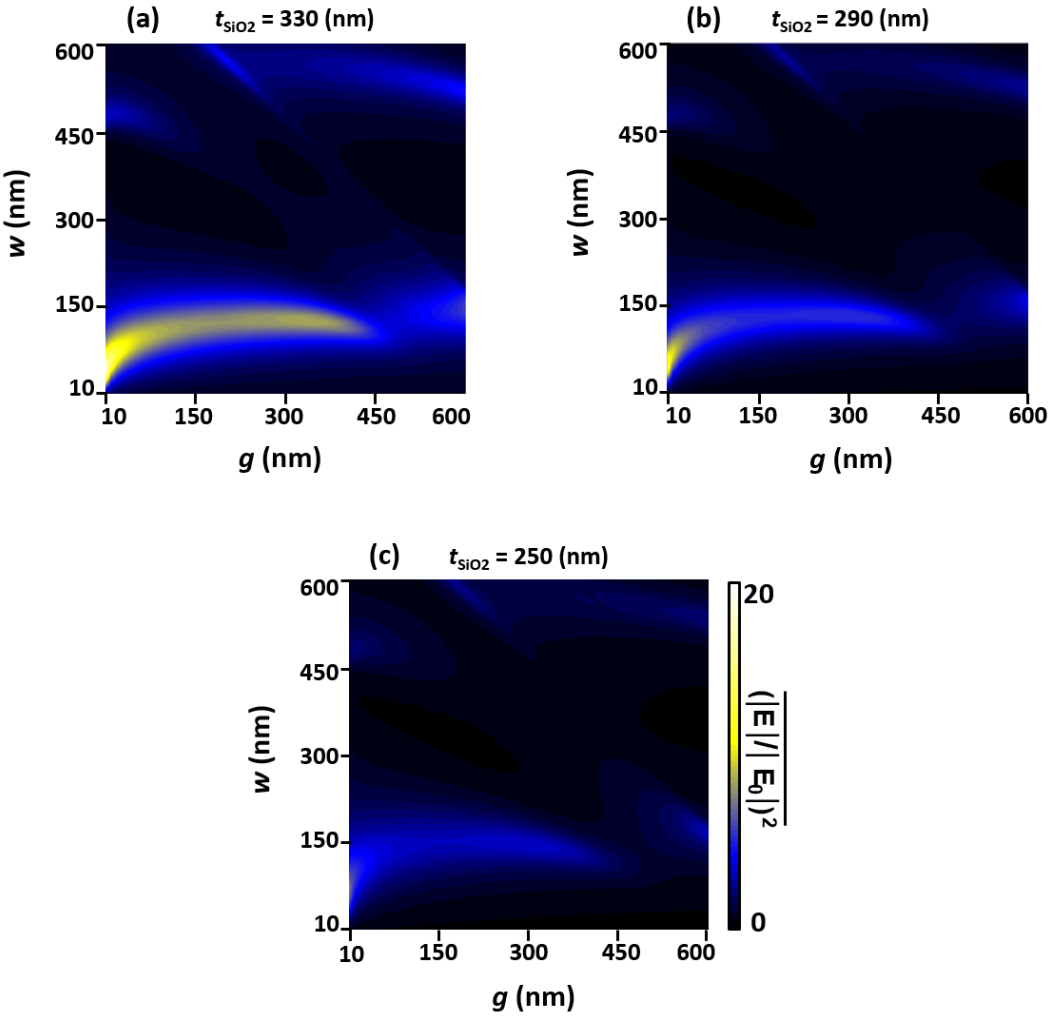

Figure 4.2.8. Color plot of surface average enhancement versus g and w at three t_{SiO2} values.[114]

values represent the maximum, median, and minimum enhancement values from the t_{SiO2} layer, see Figure 4.2.7 (d). The color maps show the importance of choosing the accurate t_{SiO2} that can significantly increase the optical enhancement.

All the previous results in Section 4.1.2 dealt the with single-width structure. However, the rest of this section will be focused on the impact of the dual-width structure on the optical enhancement. The proposed structure is shown in Figure 4.2.9 (a).

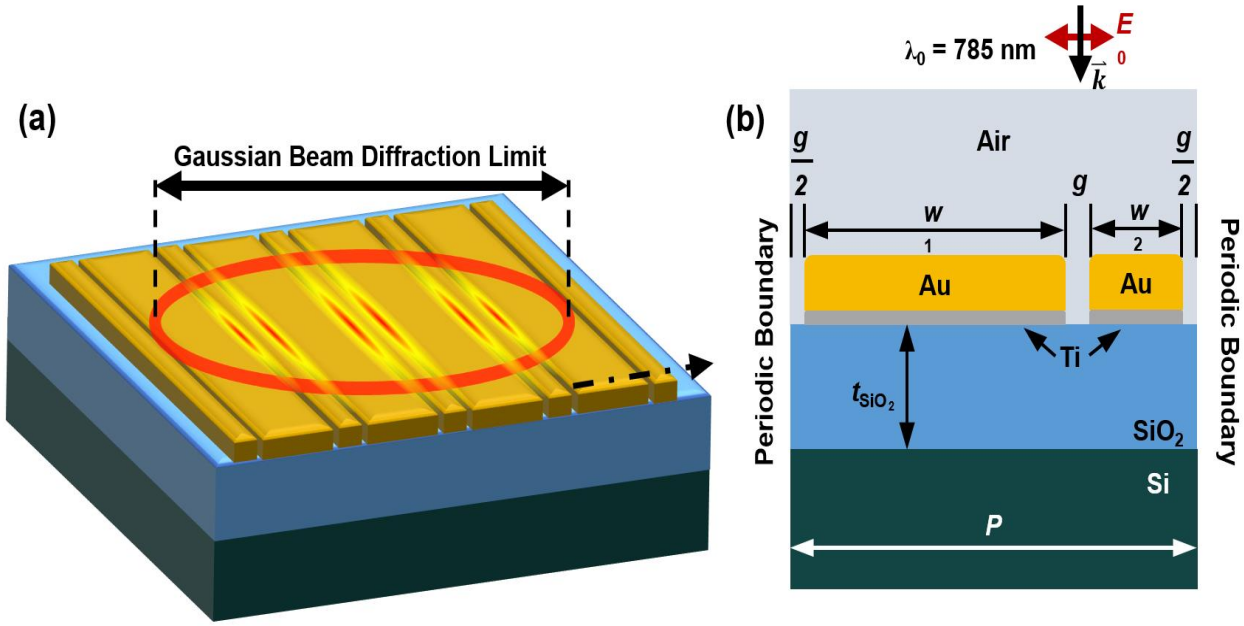

Figure 4.2.9. (a) 3D and (b) 2D sketches of the dual-width plasmonic grating structure atop a Si substrate.[115]

A cross-section view of one period that includes wire combination, w_1 and w_2, and gap space, g, is shown in Figure 4.2.9 (b). The optical enhancement of the integration area surrounding the gap space was calculated and presented in the results. In this model, the parameters, t_{Ti}, t_{Au}, λ_0, and t_{SiO2}, were set constant at 1 nm, 15 nm, 785 nm, and 330 nm, respectively. Furthermore, the incident light is simulated to normally strike the structure from the top. To probe the enhancement at the dual-width structure, the wire width combination, w_1

and w_2, were swept from 20 nm to 500 nm by 10 nm increments. Then, the average optical enhancement in the gap region was calculated at every single mesh point and presented as a color map in Figure 4.2.10 (a).[115]

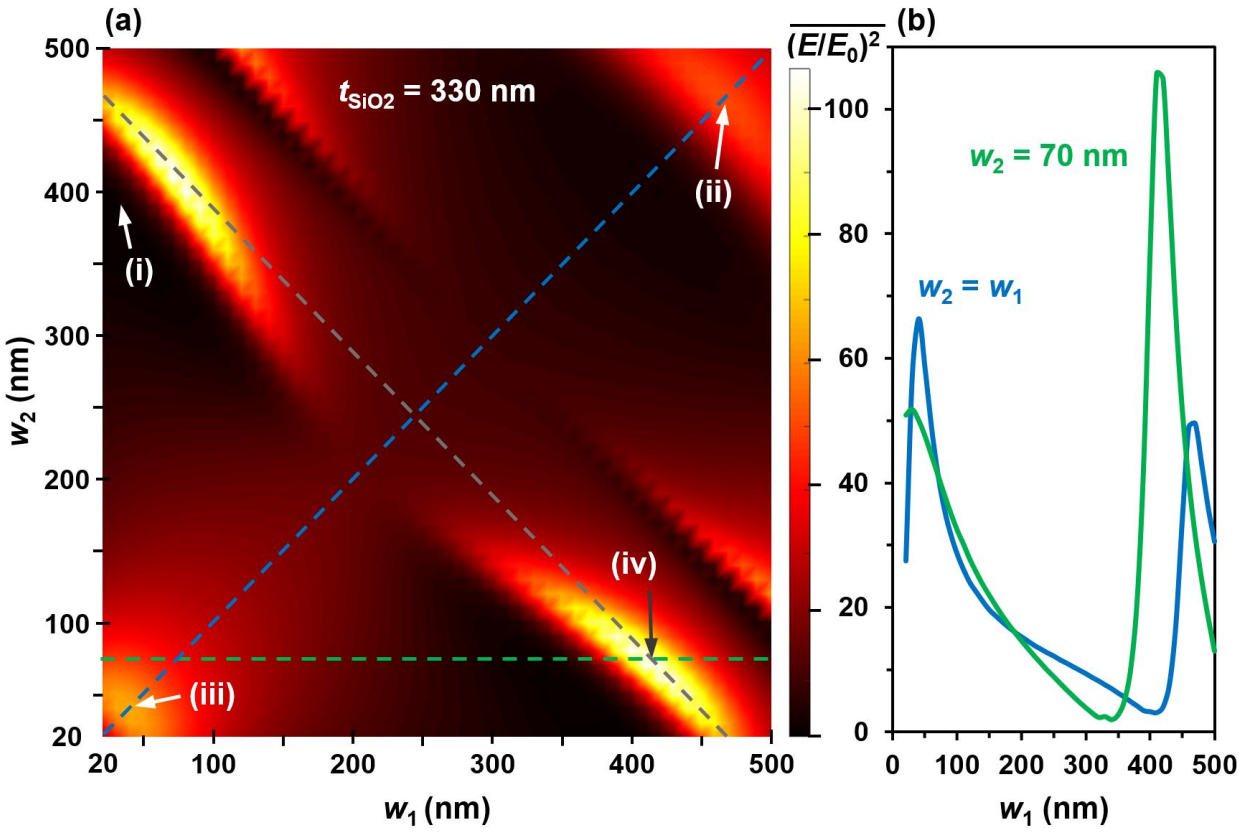

Figure 4.2.10. Color map and plot of average optical enhancement vs. (a) dual-width, w_1 and w_2 and (b) single-width, w_1.[115]

The diagonal dashed blue line expresses the single-width structure. Several resonant peaks are noticed at different areas. Two of these resonant peaks appear at spot (ii), when w_1 = w_2 = 470 nm, and (iii), when w_1 = w_2 = 40 nm. These are due to the periodicity of the structure (Rayleigh anomaly).[116] Another peak appears at spot (iv), when w_1 = 410 nm and w_2 = 70 nm, on the dashed grey line with a slope of -1. This peak is attributed to the hybridization effects.[100] For comparison purposes, the minimum value of the average enhancement, which appears at spot

(i), is taken. Figure 4.2.11 0illustrates the electric field distributions at the four spots that are indicated in (a). Figure 4.2.10 (b) shows two plots of the optical enhancement as a function of *w* at the blue (single-width) and green (dual-width) dashed lines. The plot reveals that the dual-width structure can double the enhancement.

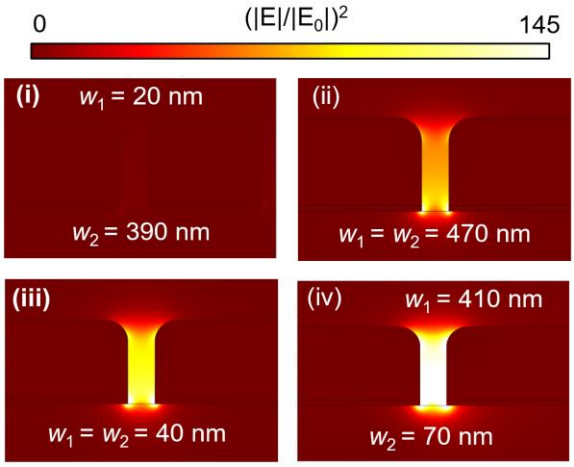

Figure 4.2.11. Electric field distributions at the four regions, (i), (ii), (iii), and (iv).[115]

Finally, a comparison was made between the enhancement at the optimum dual-width structure (blue curve) and the single width (red curve) as a function of t_{SiO2}, see Figure 4.2.12.[115]

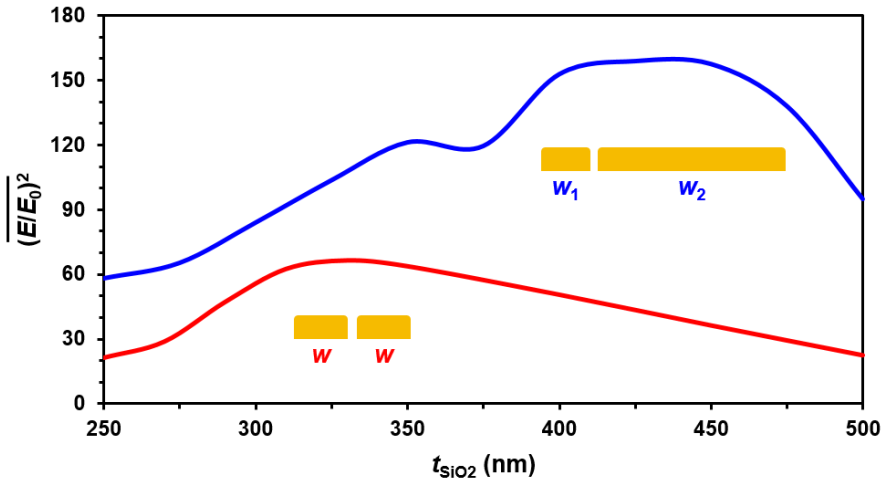

Figure 4.2.12. Peak average enhancement values as a function of t_{SiO2} for the optimal dual- and single-widths.[115]

The plot shows a significant difference between the two enhancements, and this difference reaches ~160%.

4.3 Plasmonic nanogratings on GaAs substrate

The next focus of this dissertation will be on the gallium arsenide, GaAs, substrate for plasmonically enhanced GaAs photo-detector applications. This section focuses on the optical enhancement that can be gained from gold nanostructures on GaAs. In addition, the effects of wire width structures (single- and dual-widths), gap space, wire thickness, incident wave angle, and taper angle were studied. A single wavelength detection technique was used to determine the optical enhancement. The incident wavelength was fixed at 875 nm, which corresponds to the near bandgap of the electrons in the GaAs, for all models that are discussed in this section.

Figure 4.3.1 shows one period of the simulated model that consists of air in the top and the nanostructure atop GaAs. The incident electric field, E_0, with p-polarization and wavelength, λ_0 = 875 nm, is modeled to strike the nanowires from the top with zero incident angle. g, w_1, w_2, k, P, and E_0 are indicated in Figure 4.3.1.

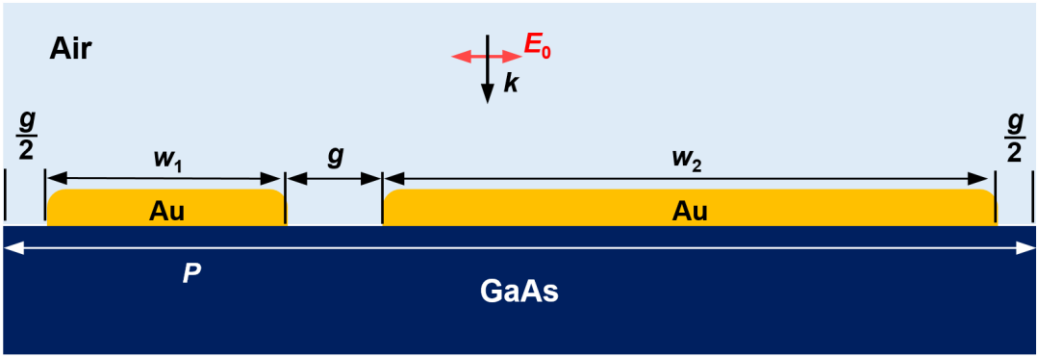

Figure 4.3.1. Cross section of dual-width grating structure on GaAs substrate.

One of the GaAs features is roughness, which can give enough flexibility to fabricate the

device without an adhesive layer, Ti. Instead, the nanostructure directly touches the surface of GaAs. Figure 4.3.2 depicts a color map of the summation of the optical enhancement in the GaAs near the gaps.

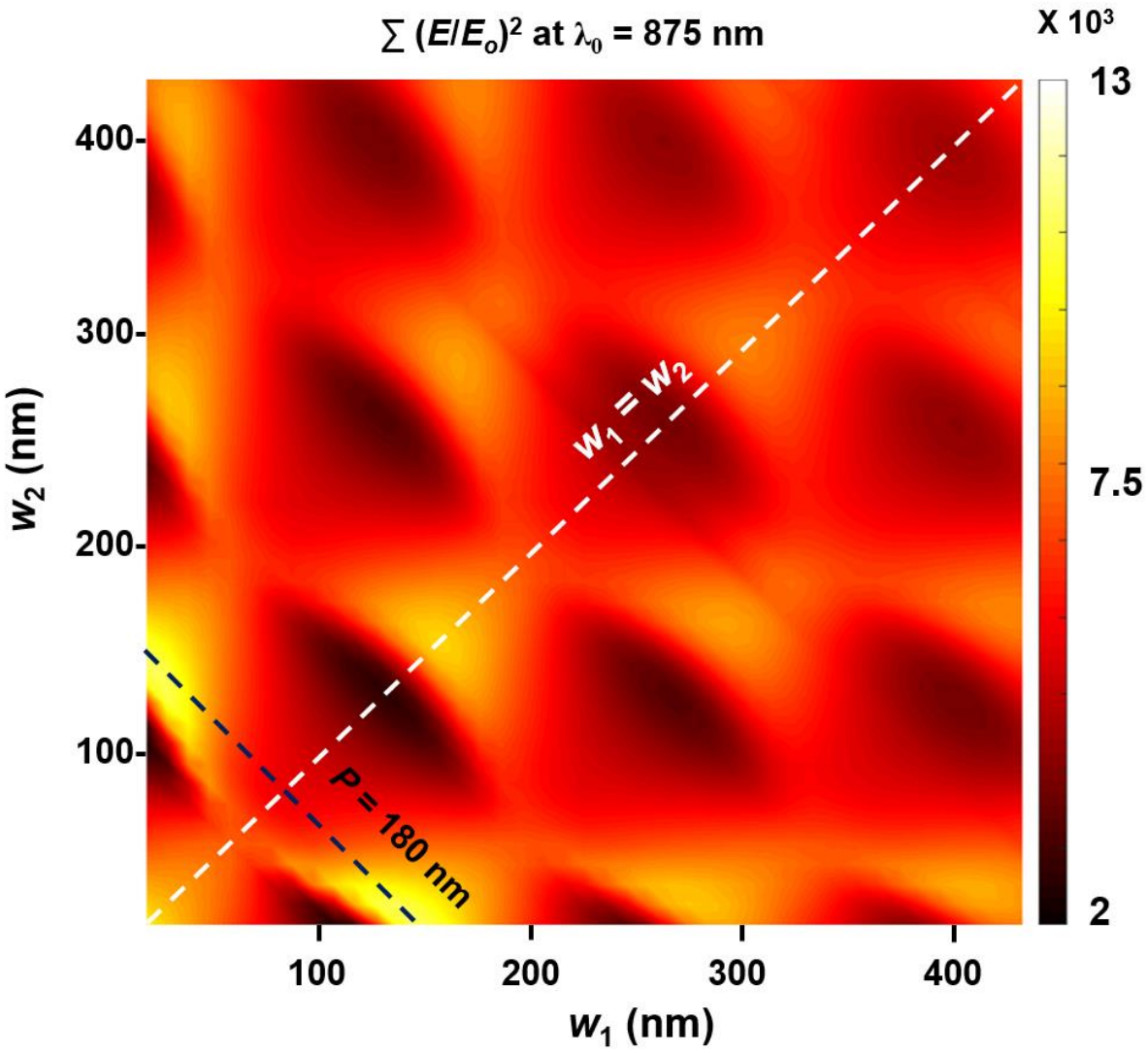

Figure 4.3.2. Color map of optical enhancement as a function of dual-width.[117]

Both wires, w_1 and w_2, were swept from 20 to 440 nm by 10 nm increments. Again, the diagonal states the single-width structure regions, and off the diagonal states the dual-width combination structure regions. The highest peak of the optical enhancement reaches a value of

9544 for the single-width structure, $w_1 = w_2 = 160$ nm; however, it reaches a value of 11282 for the dual-width structure, $w_1 = 150$ nm and $w_2 = 20$ nm. The result shows that the dual-width combination structures can provide more optical enhancement compared to the single-width structures. This extra enhancement could exceeds 10%. Figure 4.3.3 illustrates the electric field distributions of one period for the two different nanograting structures. The period of each structure is equal to 180 nm, however, the gap position in each structure is located at different position.

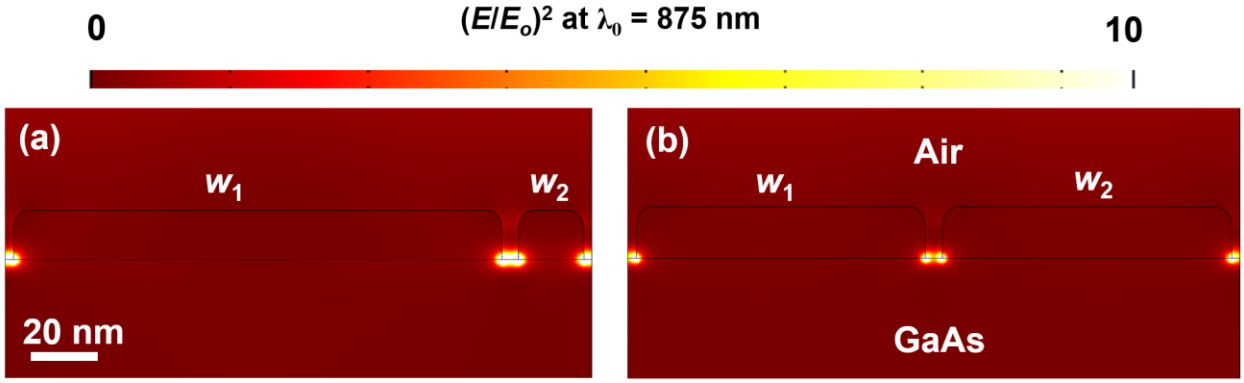

Figure 4.3.3. Electric field distributions for (a) dual-width and (b) single-width.[117]

The calculated optical enhancement for the optimum dual-width structure is ~19% greater than that of the single-width structure, at $P = 330$ nm. The optimum widths of the structures (dual- and single-width) are $w_1 = 150$ nm and $w_2 = 20$ nm and $w_1 = w_2 = 160$ nm, respectively.[117] Figure 4.3.4 (a) is the plot of the average optical enhancement (in GaAs near the gaps) versus w for different g values. w was swept from 10 to 500 nm with 10 nm increments, and g was swept from 5 to 50 nm. The plot illustrates that an increase in w creates multiple-peaks in the average optical enhancement curve; these optimal peaks decrease when w increases. Moreover, the average optical enhancement decreases with increasing g. This trend of the data proves that smaller g can produce a larger average optical enhancement.

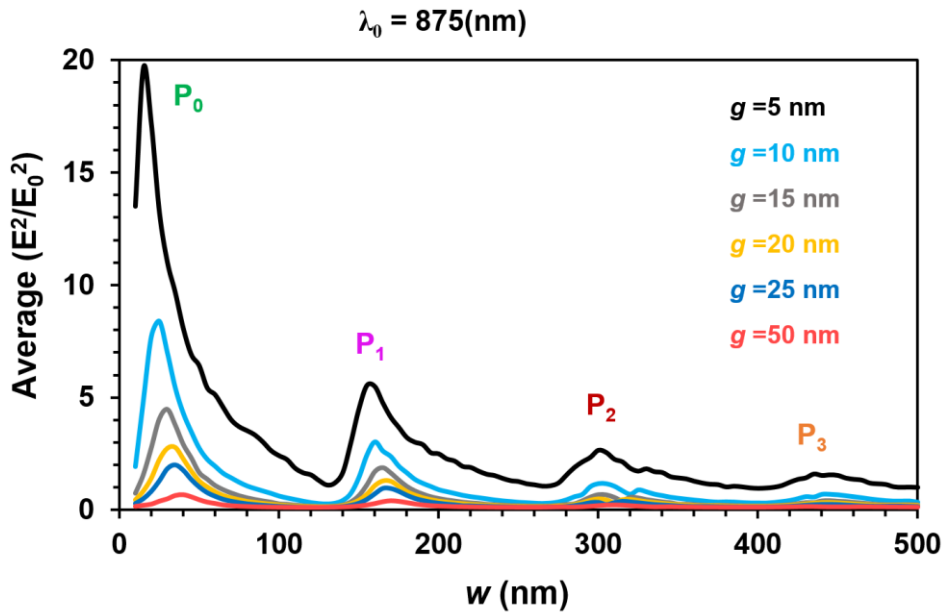

Figure 4.3.4. Plots of average optical enhancement vs. (a) w and (b) g.[106]

A red shift to each peak in the curves is noticed when both w and g increase, as shown in Figure 4.3.5. These figures illustrate the big difference between the peaks at P_0, and this difference becomes smaller at the other peaks, P_1, P_2, and P_3.[106]

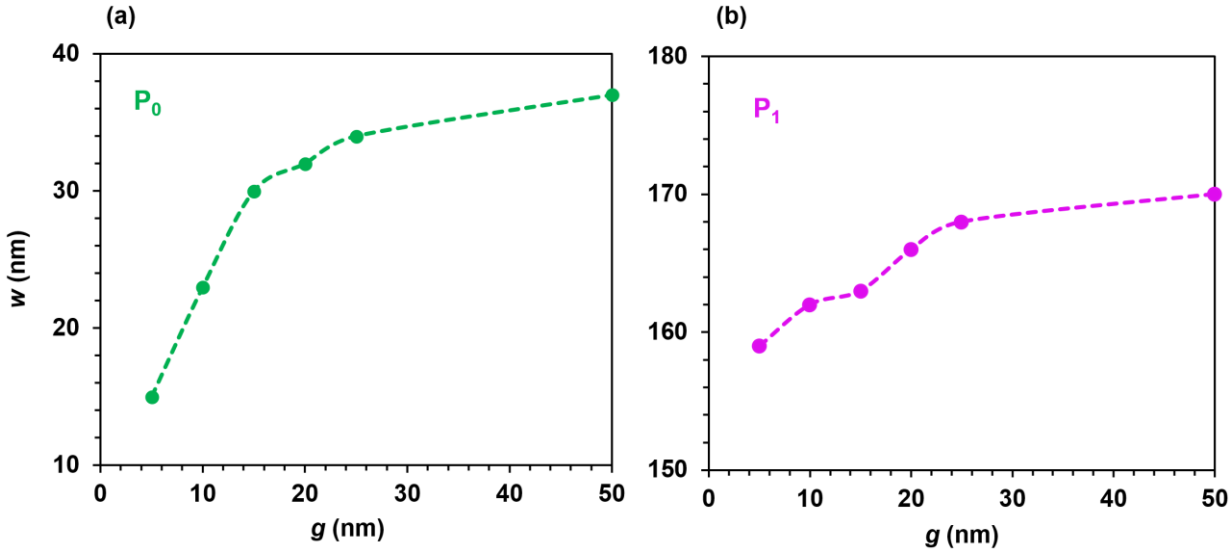

Figure 4.3.5. Plots of enhancement peaks vs. w and g, corresponding to Figure 4.3.4 (a).[106]

The average optical enhancement as a function of g at the first two peaks, P_1 and P_2, was

plotted in Figure 4.3.6. It shows that the average optical enhancement increases ~260% at same g, but different peaks (P_0 and P_1). However, the increase becomes smaller and smaller when increasing g. One of the factors that could affect the average optical enhancement is to use Ti as an adhesive layer. The enhancement was calculated in the entire GaAs substrate for various thicknesses of Ti (t_{Ti}), which were swept from 0 to 10 nm by 1 nm increments. It was found that the t_{Ti} of the layer can significantly reduce the enhancement in both the gap space and the GaAs layer; it reduces the plasmonic resonance magnitude that was caused by the incident light, see Figure 4.3.7.

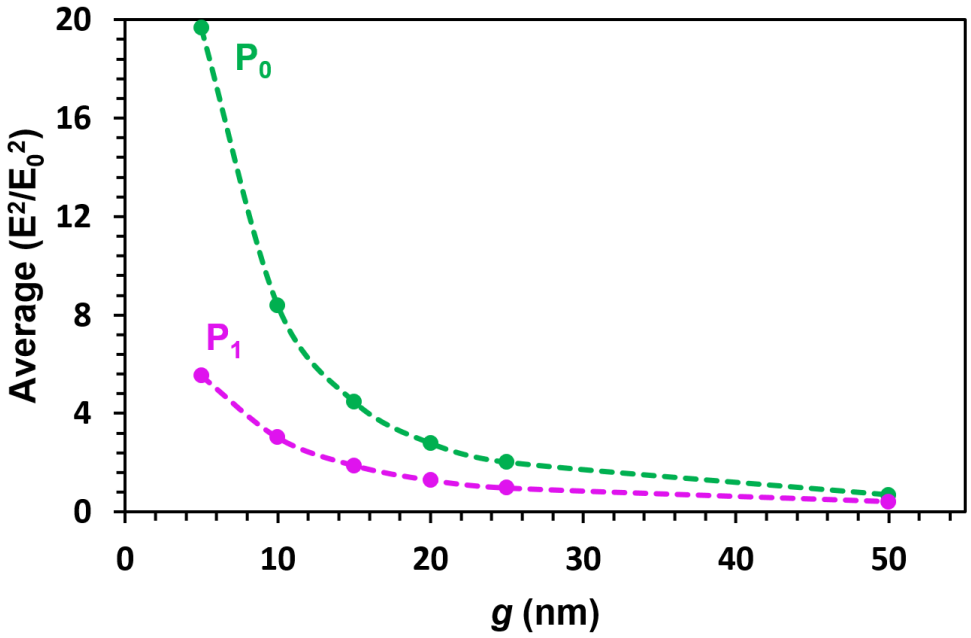

Figure 4.3.6. Average optical enhancement vs. g at P_0 and P_1.[106]

A normalized average optical enhancement versus t_{Ti} was plotted in Figure 4.3.7 (c) when w = 50 nm, g = 35 nm, and t_{Au} = 10 nm. Even if t_{Ti} = 1 nm, it can extremely reduce the enhancement. The plot shows that at t_{Ti} = 0 nm, the enhancement jumps to more than 20 times compared with the enhancement at t_{Ti} = 1 nm.[118] This is expected because Ti is considered as a

very weak plasmonic material and has a very large imaginary dielectric function component.

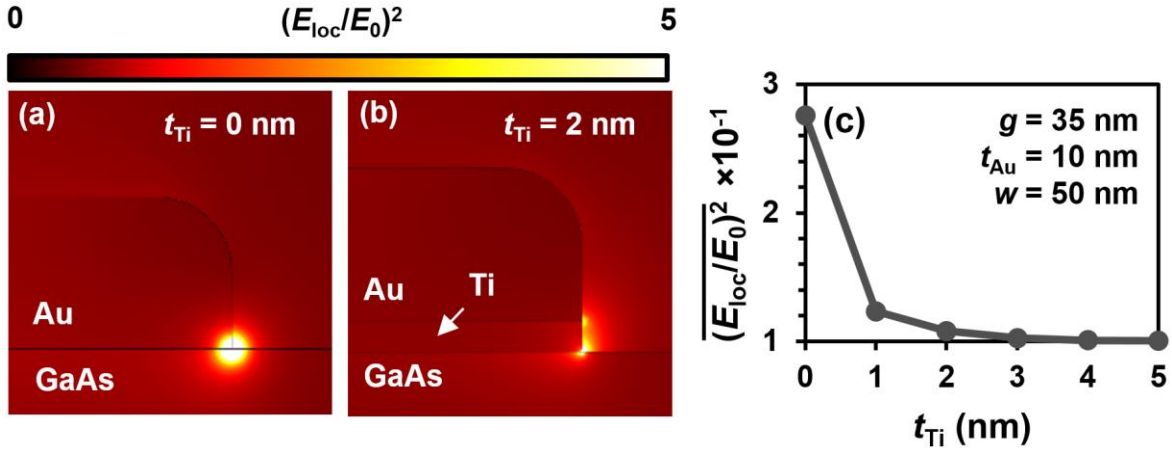

Figure 4.3.7. Electric field distributions (a) without (b) with Ti. (c) Plot of average optical enhancement vs. t_{Ti}.[118]

As a result, using Ti can dampen the plasmon effect, which could decrease the enhancement, because of the charge interactions between the Ti/Au interfaces.[119] In addition, the average optical enhancement was studied and plotted versus t_{Au}. The variables, w, g, λ_0, and t_{Ti}, were set constant at 160 nm, 5 nm, 875 nm, and 0 nm, respectively. Two different values of t_{Au} were simulated and their electric field distributions are shown in Figure 4.3.8.

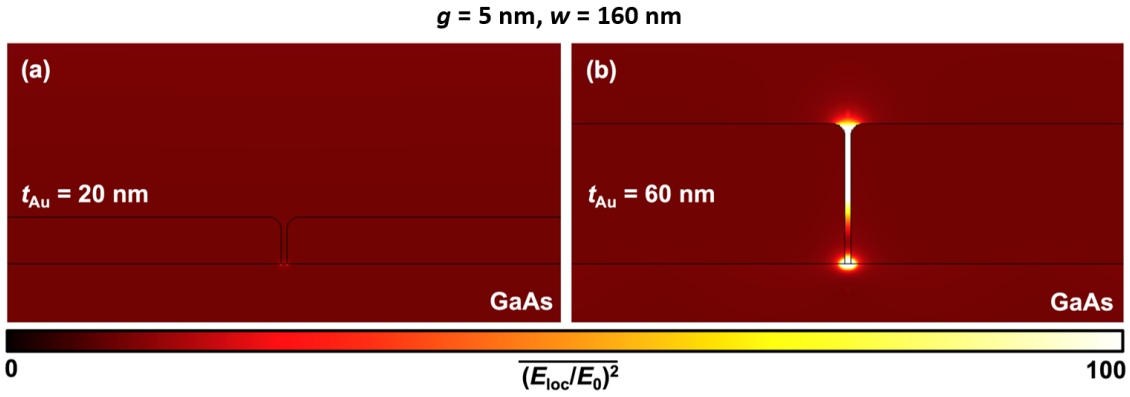

Figure 4.3.8. Electric field distributions for two different values of t_{Au}, 20 and 60 nm.[118]

As t_{Ti} increases from 20 to 60 nm, the average optical enhancement increases in both the

GaAs layer and the gap space.[118] Next, the average optical enhancement within the entire GaAs layer was calculated as a function of w and t_{Au}. The data result is represented in the color map as shown in Figure 4.3.9 (a).

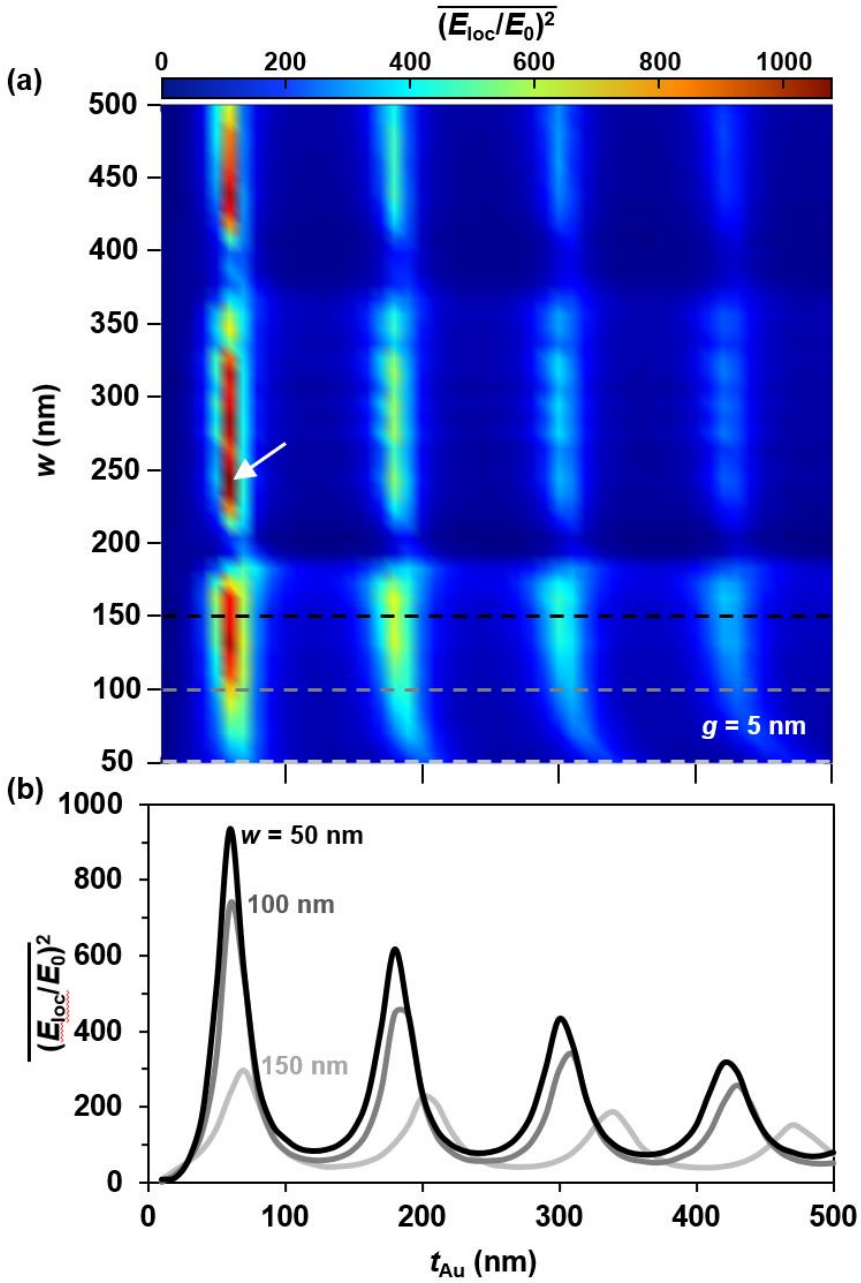

Figure 4.3.9. (a) Color map and (b) plot of average optical enhancement as a function of w and t_{Au}.[118]

w was swept from 50 to 500 nm, whereas, $t_{Au}$was swept from 10 to 500 nm with a step size of 10 nm. Both g and $\lambda_0$were fixed at 5 nm and 875 nm, respectively. The map shows that some peaks appear in the average optical enhancement spectrum at specific t_{Au} values as w increases. In Figure 4.3.9 (b), the plot of the enhancement took the same value range of t_{Au} but at three particular wire widths, w = 50, 100, and 150 nm, representing by the dashed lines in Figure 4.3.9 (a). Both (a) and (b) in Figure 4.3.9 exhibit several peaks and troughs in the enhancement spectrum while increasing t_{Au}. These peaks are also resonant values for t_{Au} that can improve the enhancement due to plasmonic effects. The maximum peaks of the average optical enhancement are located at w = 240 nm and t_{Au}=60 nm, as shown with a white arrow on Figure 4.3.9 (a). This resonance peak could be attributed to Fabry-Perot resonance phenomenon. To confirm that the geometry is ideal and optimized, the reflection spectrum in Figure 4.3.10 (a) shows a resonance at λ_0= 875 nm. Figure 4.3.10 (b) shows the average optical enhancement as a function of t_{Ti} at the resonant structure.

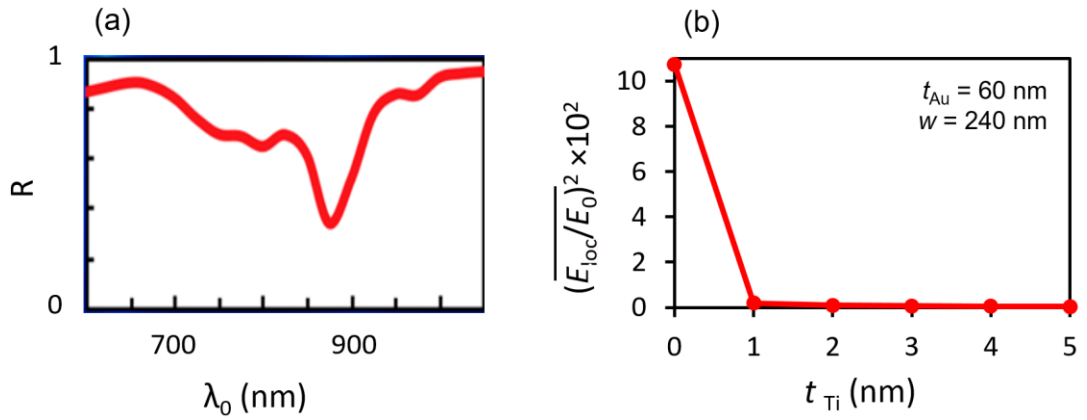

Figure 4.3.10. (a) Reflection spectrum vs. wavelength and (b) average optical enhancement vs. Ti thickness.[118]

The enhancement at the optimum structure is between 10 and 20 times greater than other non-optimal structures. Two other factors that can improve the optical enhancement of the

nanograting structures were studied as well. These factors are the period (P) for a single-width and the incident wave angle (α). Figure 4.3.11 shows a 3D depiction of the a nanograting, illustrating α and the other parameters, such as P, w, g, t, k_0, and E_0.[116] The previous models were updated to calculate the enhancement when g and α are varied. In this case, only one period, which includes one g and one w, was modeled. Periodic boundary conditions, however, were horizontally applied to make an infinite array. In this section, a very strong plasmon resonance appeared at the optimum wire width (w = 160 nm) when the wavelength λ_0 = 875 nm was simulated and used as a baseline.[106] t_{Au} was fixed at 15 nm. Then the calculations focused on the effects of both P and α.

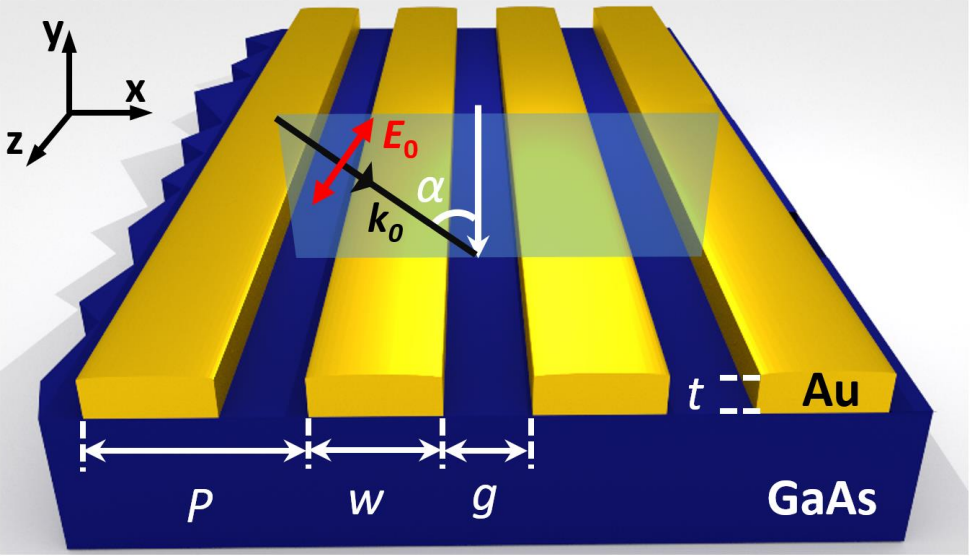

Figure 4.3.11. 3D schematic diagram of 1-D nanograting structure.[116]

Figure 4.3.12 shows the color maps of reflection, transmission, and absorption versus P and α. To study the impact of P on the enhancement, two parameters should be taken into consideration. These parameters are w and g since P is a function of both ($P = w + g$). For example, Figure 4.3.12 (a)-(c) are the results with w = 160 nm; whereas, Figure 4.3.12 (d)-(f) are

the results with g = 90 nm. The first three maps, Figure 4.3.12 (a)-(c), are a function of g (or P) and α, which were swept from 5 to 300 nm (or 165 to 460 nm) and 0° to 45°, with a step size of 1 nm and 1°, respectively. In the reflection color map, Figure 4.3.12 (a), it is expected that the values are very high at a small g region because of the high filling factor, which is defined as the ratio between P and g.

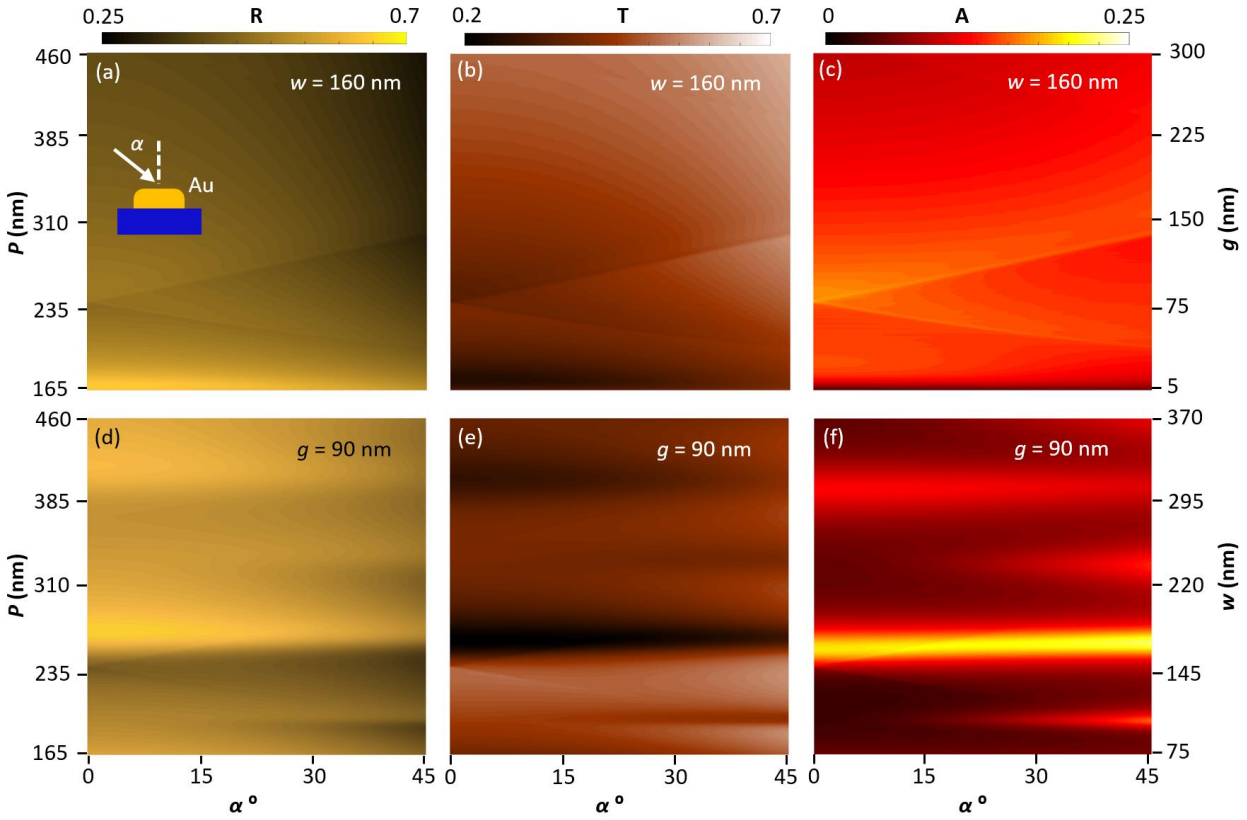

Figure 4.3.12. Reflection, transmission, and absorption color maps vs. α° and P (w and g).[116]

Increasing g leads to reducing both the filling factor and the reflection because more light transmits through the nanograting. The second three maps, Figure 4.3.12 (d)-(f), are a function of w (or P) and α that were swept from 75 to 370 nm (or 165 to 460 nm) and 0° to 45°, with a step size of 1 nm and 1°, respectively. Figure 4.3.12 (d) expresses a different trend of reflection from that in (a). This is due to the effect of surface plasmon polaritons that generate different

modes. In Figure 4.3.12 (a), in other words, w is constant, but g is variable. As a result, Rayleigh's anomaly is dominant instead of surface plasmon polaritons. In Figure 4.3.12 (d), however, g is constant, but w is variable. Hence, surface plasmon polaritons are dominant in this case because w is increasing. This can generate multiple surface waves that couple to each other, as will be explained later. In addition, both the weaker transmission and the stronger absorption in Figure 4.3.12 (e) and (f) are completely different from those in Figure 4.3.12 (b) and (c). Again, this is due to the different type of modes that generate in each case. For example, at α = 0° and P = 258 (w = 168 nm and g = 90 nm) a very strong absorption is noticed, see Figure 4.3.12 (f); however, less absorption is observed at the same values of incident wave angle and period (α = 0° and P = 258 nm, w = 160 nm and g = 98 nm), see Figure 4.3.12 (c). Since the reflection is a function of α,[120] varying α from normal to oblique can make a significant change in the optical response. In Figure 4.3.12 (a)-(c), the resonant periods shift as α changes and two distinct Rayleigh's anomalies appear in the spectrum at any oblique incidence, according to the general equation of diffraction grating (Equation 2.82).[116] This trend is weak when sweeping w due to the dominance of SPPs, see Figure 4.3.12 (d)-(f).

The transmission and absorption data were taken from the previous color maps in Figure 4.3.12; they were plotted as a function of w and g, black and red lines, respectively, as shown in Figure 4.3.13. g was swept from 5 to 840 nm (P = 165 to 1000 nm at α = 0°) and w = 160 nm. From the absorption spectrum (red line), the optimum gap (g = 83 nm) was picked and set constant for the sweep of w. Then, w was swept from 82 to 917 nm (P = 165 to 1000 nm). Sharp peaks and dips appear in the spectra of the transmission and the absorption. These sharp changes are due to the Rayleigh anomaly, see Figure 4.3.13 (a) and (b). According to Equation 2.83, five resonant peaks should appear in the spectra, four of which are located at P = 242, 484, 726, and

968 nm when m = 1, 2, 3, and 4, respectively, for the GaAs-Au interface, and only one peak is located at P = 875 nm when m = 1 for the air-Au interface.

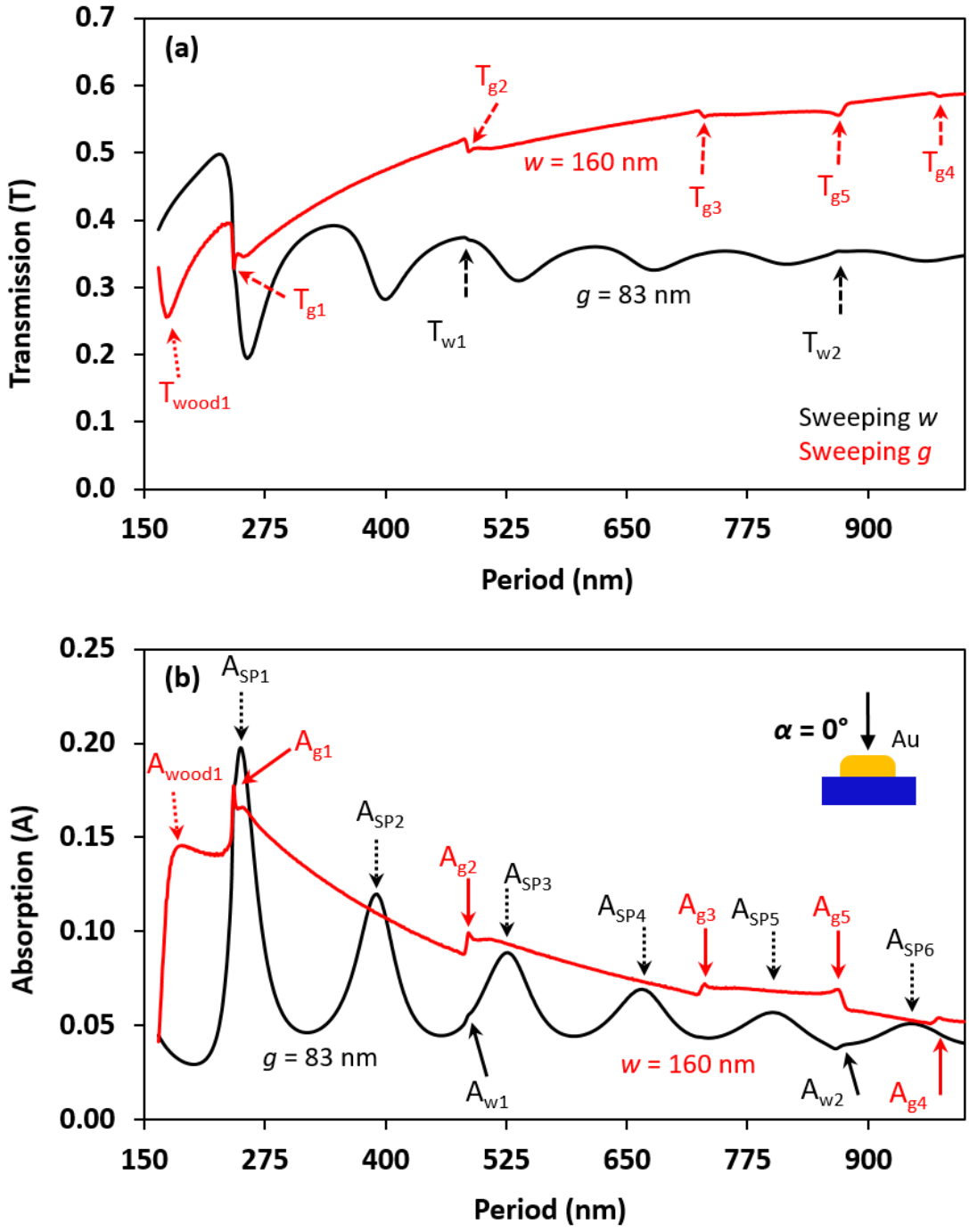

Figure 4.3.13. Plots of (a) transmission and (b) absorption vs. P (w and g), corresponding to Figure 4.3.12.[116]

The computation results show that the resonant peak values are located at P = 243, 486, 731, and 975 nm when m = 1, 2, 3, and 4, respectively, for the GaAs-Au interface, and the last peak is located at P = 868 nm when m = 1 for the air-Au interface. These peaks are labeled as T_{g1}/A_{g1}, T_{g2}/A_{g2}, T_{g3}/A_{g3},T_{g4}/A_{g4}, and T_{g5}/A_{g5}, respectively. Additionally, only one diffuse calculated peak is located at P = 190 nm; however, in the computation results, the peak is located at P = 187 nm according to Equation 2.84. This peak belongs to Wood's anomaly and is labeled as T_{wood1}/A_{wood1}in Figure 4.3.13 (a) and (b). The resonant period values for Rayleigh-Wood anomalies were well matched in both calculations, the analytical and the computational. Since both sweeping g and w give the same period, Rayleigh's anomaly peaks and dips are located in the same positions. Two very small peaks, labeled T_{w1}/A_{w1} and T_{w2}/A_{w2}, appear in the spectra and belong to Rayleigh's anomaly in the case of sweeping w. Plus, several peaks, labeled A_{SP1-6}, belonging to surface plasmon resonances, appear in the absorption spectrum; however, no Wood's anomaly is observable in the same spectrum. As w increases, the peaks of surface plasmonic resonance become wider and lower in intensity due to the optical enhancement reduction.[116]

The electric field and charge distributions at the resonant peaks, represented by the normalized local field $\left|\frac{E_{local}}{E_0}\right|$ and surface charge density (σ) , are shown in Figure 4.3.13. These distributions are generated by Rayleigh-Wood anomalies and surface plasmon polaritons. The dips/peaks in the transmission/absorption spectrum are located at the same positions. In the case of sweeping g, no difference is noticed among the resonant modes, Figure 4.3.14, but only one as shown in Figure 4.3.14 (d). This unique resonant mode is due to the near matching between P and λ_0 (868 nm and 875 nm, respectively) at m = 1 for the air-Au interface. This close matching accumulated the charges on the top interface of the nanowire and made a different

resonant mode. As a result, the electric field becomes stronger in both the air and GaAs.

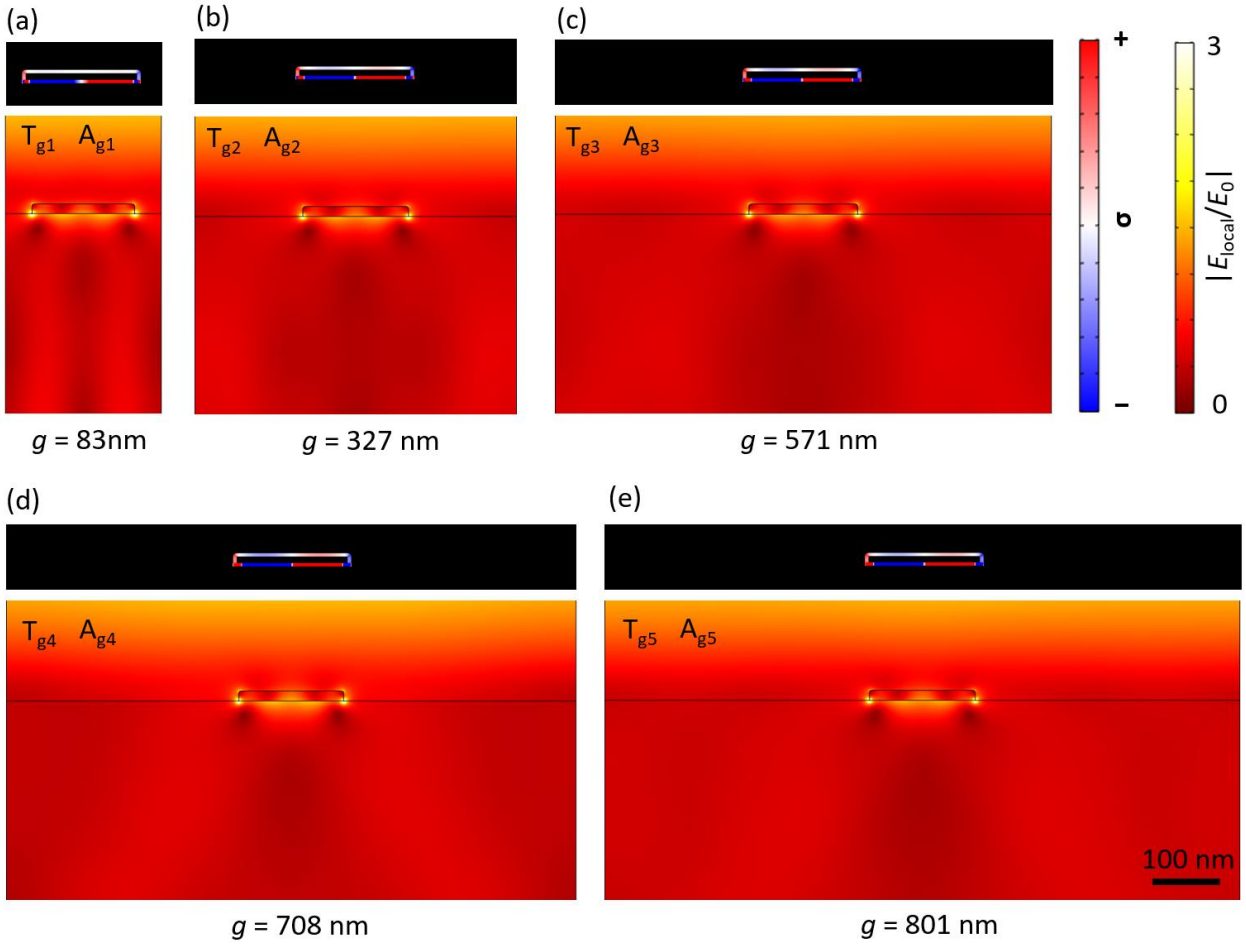

Figure 4.3.14. Electric field and charge distributions at resonant peaks, corresponding to Figure 4.3.13 (b).[116]

Again, this resonant mode is due to the strong constructive interference between the electromagnetic waves.[116] In the case of sweeping *w*, only two resonant modes appear in the spectra in Figure 4.3.13; these resonant peaks, T_{w1}/A_{w1} and T_{w2}/A_{w2}, can be attributed to Rayleigh's anomaly as well, see Figure 4.3.15. Figure 4.3.16 shows the electric field distributions at the top and bottom interfaces of the nanowires of Figure 4.3.15. The distributions are almost similar at the top and bottom interfaces; however, they are stronger at the bottom edges due to the sharp edges of the nanowires and higher GaAs refractive index. Multiple

dipoles, which can be considered as individual wavelet sources, are generated on both interfaces.

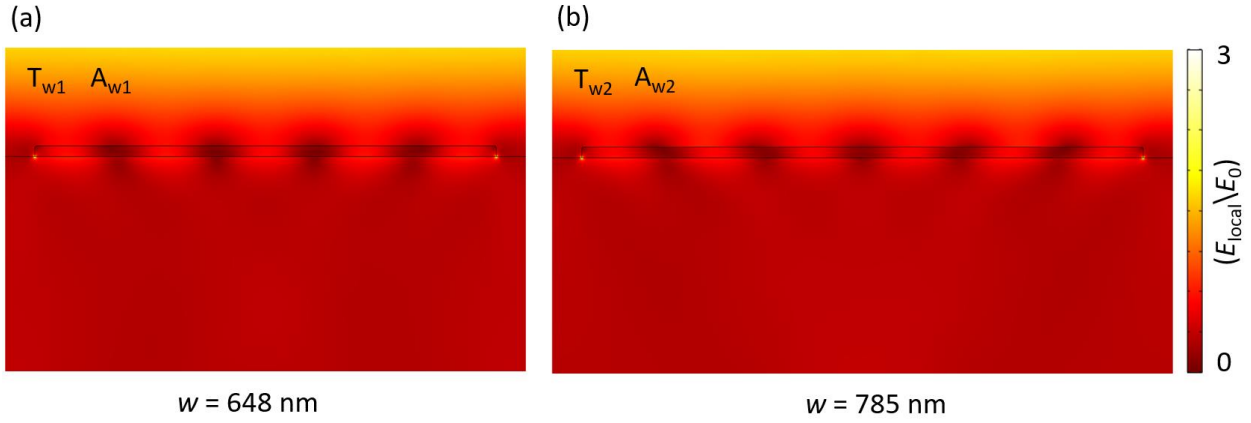

Figure 4.3.15. Electric field plots and distributions for different *w* at Air-Au and GaAs-Au interfaces.[116]

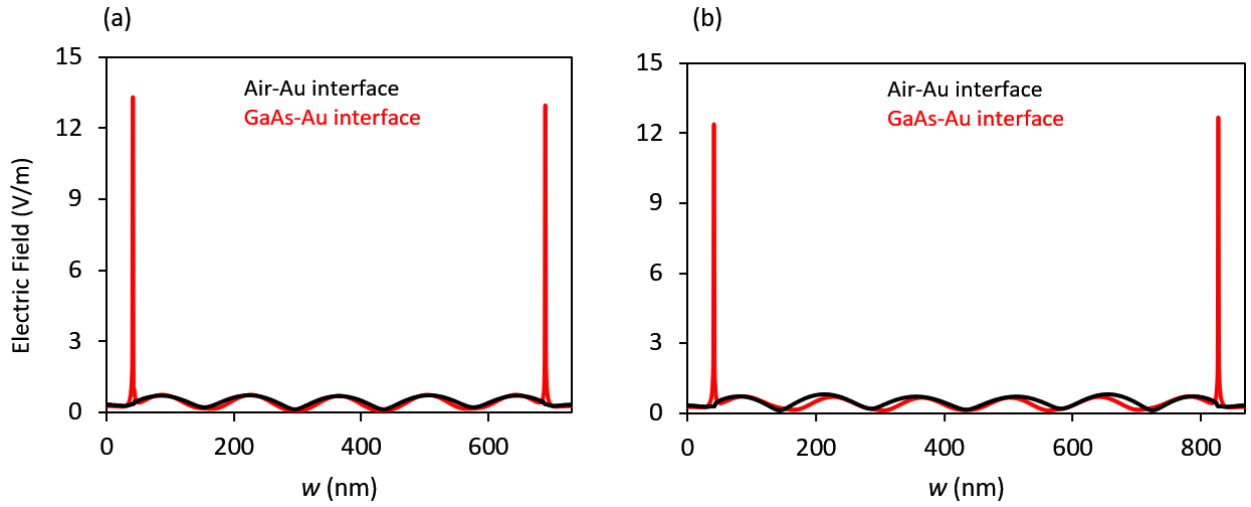

Figure 4.3.16. Electric field plots and distributions for two wire widths at Air-Au and GaAs-Au interfaces.[116]

These dipoles can radiate and interfere constructively and deconstructively with each other. This interaction can increase or decrease the total enhancement. The last two electric field distributions are illustrated in Figure 4.3.17 for the entire model and the top and bottom interfaces; they belong to Wood's anomaly, A_{wood1}, and surface plasmon, A_{Sp1}. The electric field increased 48 times at the Au-GaAs interface, compared to the Au-Air interface, at the first

resonance peak of the surface plasmon. This result can boost electron-hole pair production; hence, boosting the current density of MSM PD or solar cell applications.

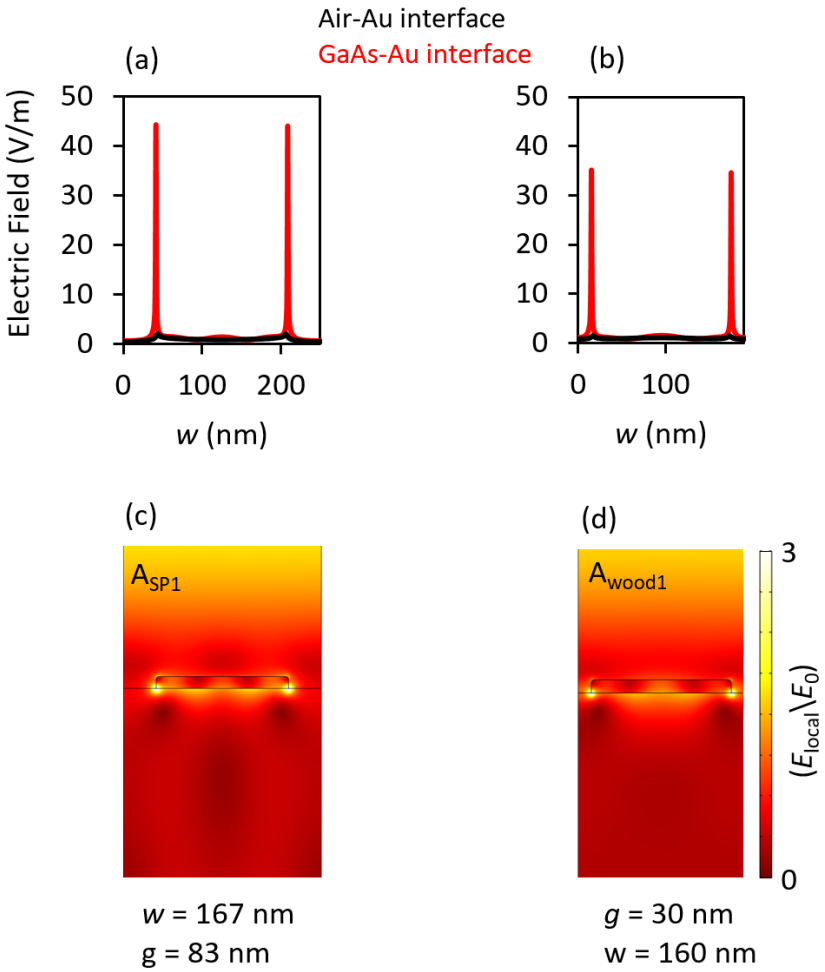

Figure 4.3.17. Electric field plots and distributions for different *g* at Air-Au and GaAs-Au interfaces.[116]

For Wood's anomaly, the electric field increased up to 35 times at the Au-GaAs interface compared to the Au-Air interface, see Figure 4.3.17 (a) and (b).[116] So far, the effect of the following parameters: single- and dual-width structures, gap space, wire thickness, and incident wave angle on the optical enhancement for GaAs substrate were studied. The other important parameter, which is the sidewall angle of the wire (taper angle), was studied here as well. In

general, the vertical sidewall angle is defined as the sidewall of the nanowires that are parallel to the normal. This means that the up and down opening slits of the gap space are equal, see Figure 4.3.18 (a).

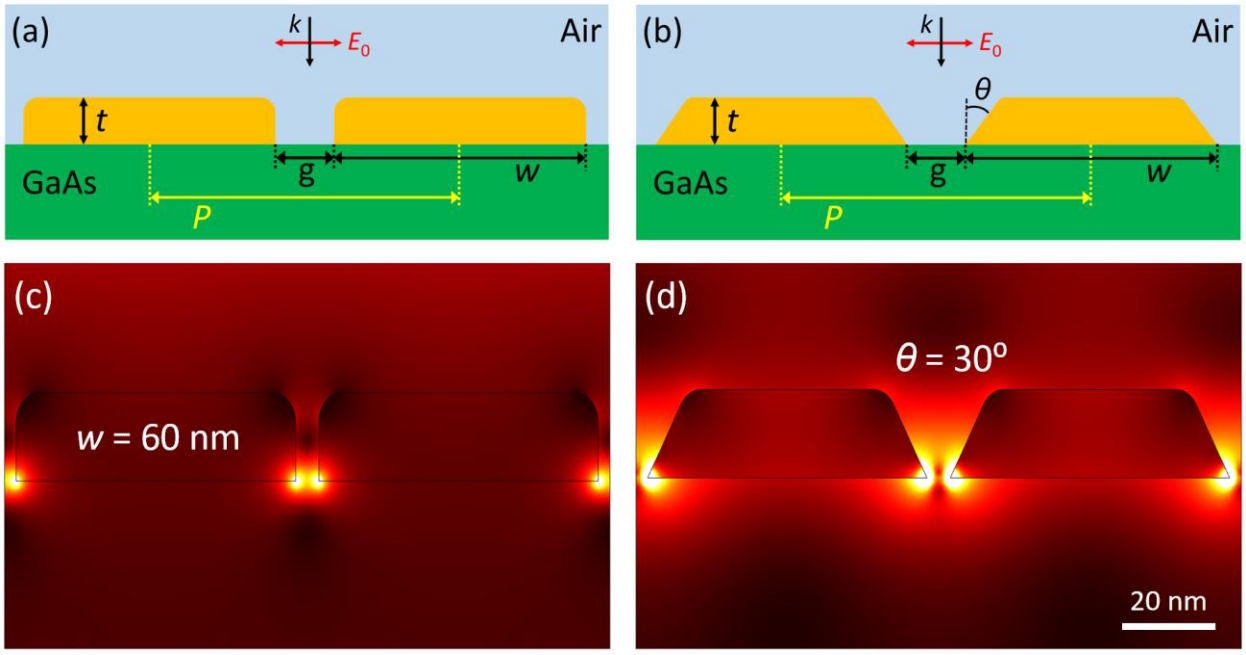

Figure 4.3.18. Cross sections and electric field distributions of vertical and tapered nanoslits.[121]

On the other hand, the taper angle is defined as the gap space that has different up and down opening slits. This means the sidewalls of the nanowires make an angle with the normal, see Figure 4.3.18 (b). In the real fabrication process, obtaining vertical sidewalls is difficult, especially when the electron beam lithography technique is used. Figure 4.3.19 illustrates some experimental results (SEM images) and show the sidewall angle of the nanowires for different structures. The surface bounded by the two white lines on the top of the wire is the top wire surface and the outer edges are the base of the wire, see Figure 4.3.19 (b). Several researchers have studied the effect of taper angle on the optical enhancement by using a gold nanograting structure with surrounding media such as air and air/glass.[80] The effect of the taper angles on the

optical enhancement in the substrate was studied in this research. Figure 4.3.18 (a) and (b) are the cross-sectional views of one single-width period structure with vertical sidewall (θ = 0°) and taper (θ > 0°) angles. t_{Au}, g, w, and $\lambda_0$were held constant at 15 nm, 5 nm, 60 nm, and 875 nm, respectively.

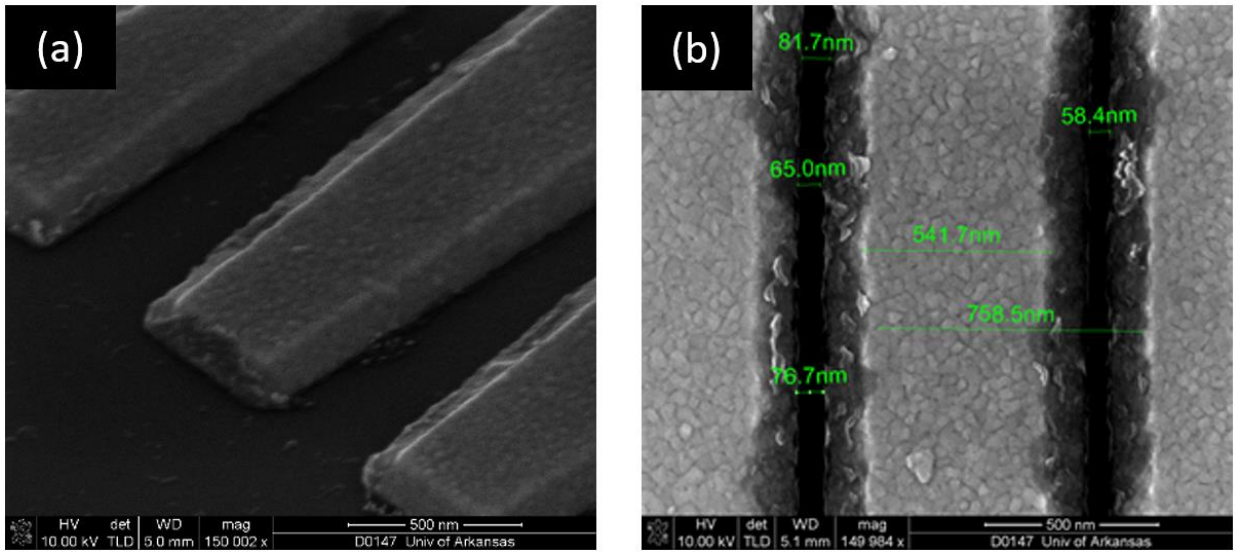

Figure 4.3.19. SEM images illustrate the sidewall angle (taper angle) of the nanowires.

To simulate the taper angle, the bottom opening slit was fixed at 5 nm, which equals to g. Light was simulated as normally incident on the metallic structures that comprise the plasmonic grating. This is one of the techniques that enhances the incident electric field in the GaAs by funneling light and exciting surface plasmon polaritons due to constructive interference effects. Figure 4.3.18 (c) and (d) are the electric field distributions for the vertical sidewall and taper angles. They show that the electric field in the case of (θ = 30°) is much larger than that in the case of (θ = 0°). The large enhancement in the case of the taper angle is due to the sharper edges at the bottom that focus the charge density at these spots. Moreover, the top opening slit can collect more light, focusing it within the gap space.[78,79]

Absorption, transmission, and reflection are calculated and plotted as color maps, which

are functions of w and θ, in Figure 4.3.20. θ was swept from 0° to 30° and w was swept from 30 to 405 nm with a step size of 2° and 15 nm, respectively. Periodic peaks appear in the maps and these peaks become weaker as w increases.

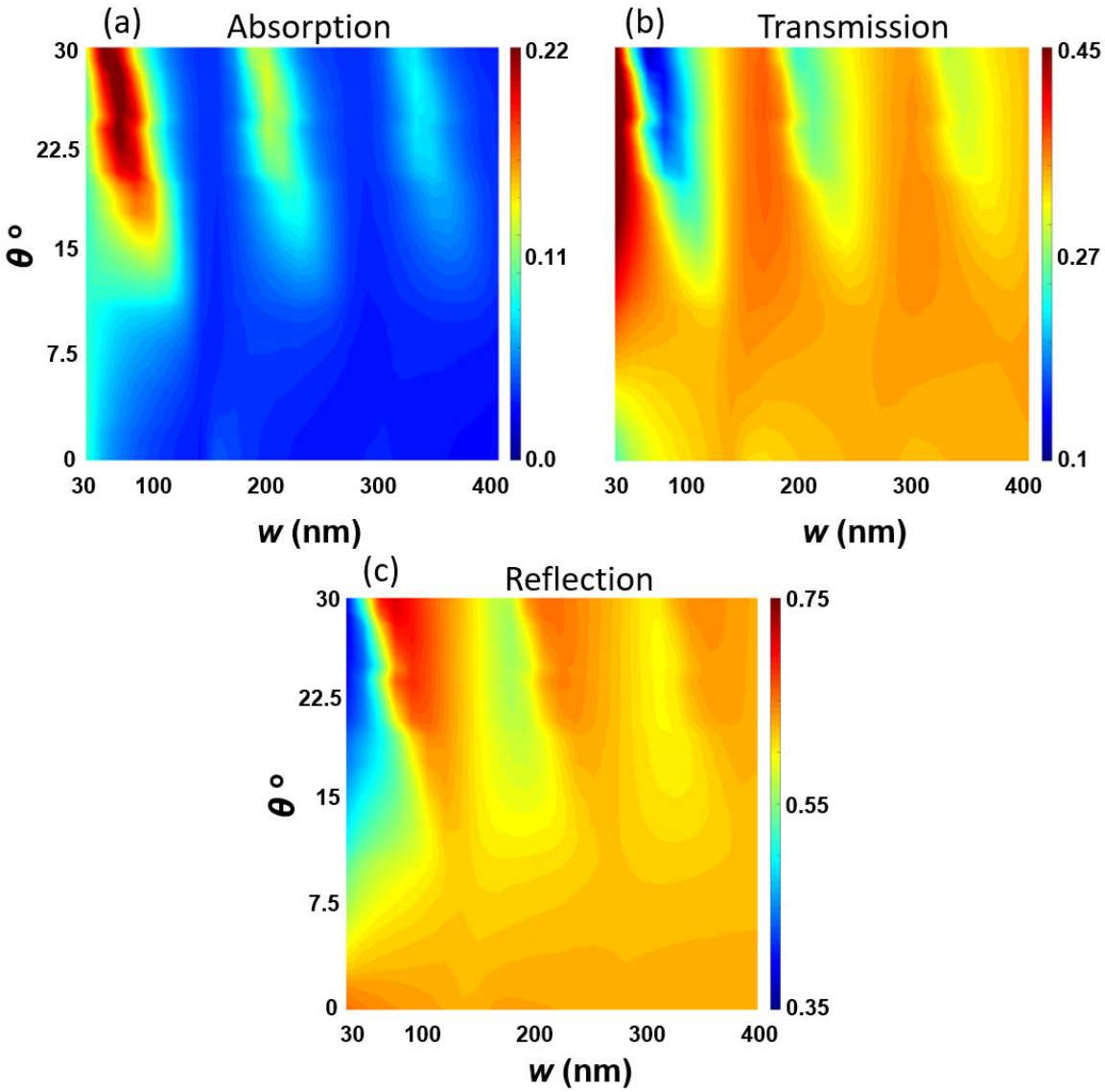

Figure 4.3.20. Absorption, transmission, and reflection as a function of w and θ°.[121]

The first two maps, absorption and transmission, show the highest and the lowest values that are located at θ = 24° to 30° when w = 60 nm, Figure 4.3.20 (a) and (b). Since the absorption is very high in this range, this result can be utilized to enhance the plasmonic MSM

PD and solar cell devices. In addition, the reflection is very high in this range of θ at particular wire widths, see Figure 4.3.20 (c). This might be harnessed to enhance different type of applications such as biosensors and SERS. To study the impact of the taper angle in detail, it is important to define two types of taper angles, positive and negative.

The first one is defined as the gap space, between two nanostructures, that has a large top opening slit and a small bottom opening slit that makes a positive angle ($\theta > 0$) with the normal, see Figure 4.3.21 (b). In contrast, the second type has a large bottom opening slit and a small top opening slit that makes a negative angle ($\theta < 0$) with the normal, see Figure 4.3.21 (c).

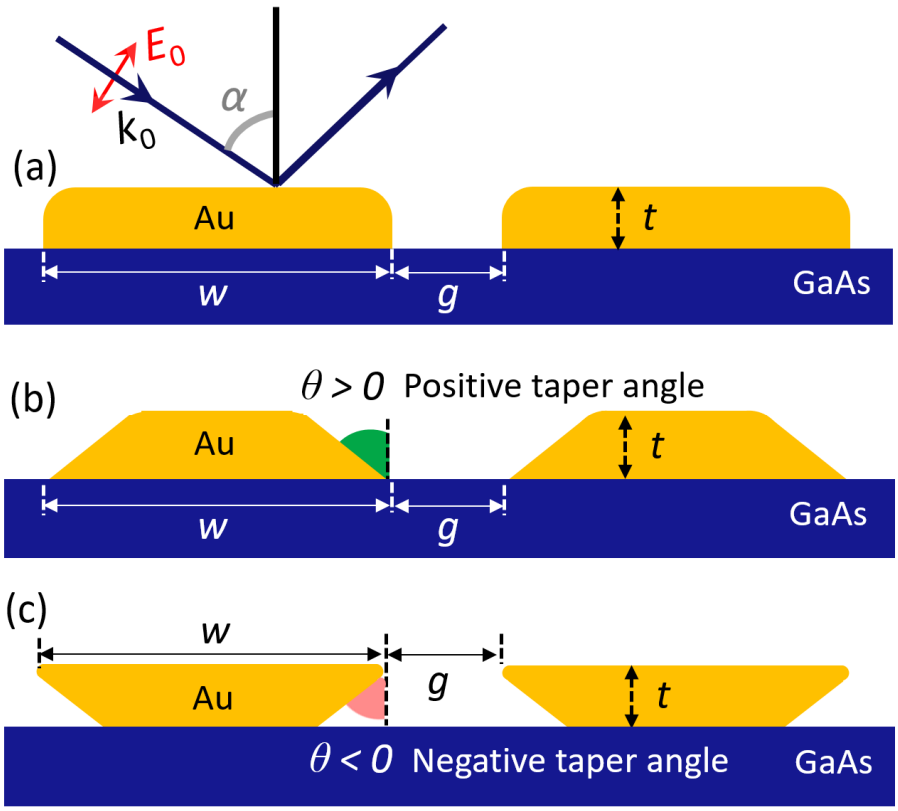

Figure 4.3.21. Cross sections of nanograting structure with (a) vertical, (b) positive taper, and (c) negative taper angles.

In addition, the vertical sidewall angle structure was considered to make a comparison in the enhancement among the taper angles, see Figure 4.3.21 (a). g was fixed at 5 nm for each of

the three structures in (a), (b), and (c). Moreover, w was fixed at 160 nm for the bottom GaAs-Au interface in (a) and (b) and for the top Air-Au interface in (c). The top edges of the three structures were rounded with a radius of 3 nm. The incident wavelength was held at 875 nm with incident angle (α) and p-polarization. Electric field distributions for the positive and negative structures are shown in Figure 4.3.22 (a) and (b), respectively. These structures are at the optimal θ and w with different incident angles. The last important factor that can enhance the incident electric field is the angle of incident wave (α). In a previous work, a reflection of nanograting was calculated and plotted as a function of α.[121] However, Figure 4.3.23 shows color maps of reflection and enhanced electric field intensity as a function of θ and α.

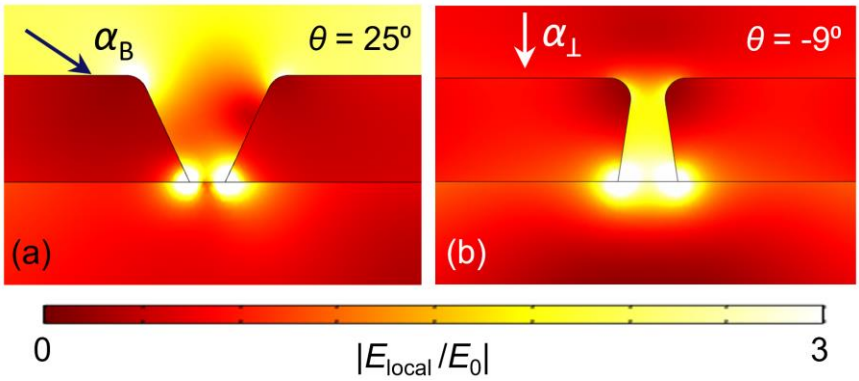

Figure 4.3.22. Electric field distributions for positive and negative taper angles.

Several dashed lines were drawn on the color maps, showing some important hotspots. For example, the horizontal black dashed lines in the middle divides the color maps into two regions. The first region (the upper part) includes the $\theta > 0°$ range; the second region (the lower part) includes the $\theta < 0°$ range. In addition, the vertical blue dashed lines represent the Brewster incident angle (α_B) position. The Brewster angle is defined as an angle of incidence at which a p-polarized light is perfectly transmitted, with no reflection, through transparent nonmetallic surfaces, or partially transmitted, with minimum reflection, through opaque metallic surfaces.

For example, the Brewster angle for bulk gold is ~71.221° for which the minimum reflection value was recorded.[122] In the color maps, α_B is considered to be 77° because the highest transmission or lowest reflection was obtained at this incident angle. The last two horizontal green and red dashed lines on the color map in Figure 4.3.23 (b) indicate the highest optical enhancement in $\theta > 0°$ and $\theta < 0°$ ranges, respectively. In Figure 4.3.23 (a), the minimum values of the reflection are located at α_B for the whole range of θ ($-40° \leq \theta \leq 40°$). The very small or zero reflection values that appear close to the 90° incidence are due to the incident wave that propagates parallel to the grating. The same pattern can be seen in Figure 4.3.23 (b), but stronger resonant peaks appear in the $0° \leq \alpha \leq 25°$ and $6° \leq \theta \leq 12°$ ranges. This is due to the optical impedance matching mechanism as explained in Section 2.4. Two hotspots are seen in Figure 4.3.23 (b), one of which occurs in the $\theta > 0°$ range when $\theta = 25°$ at α_{Br}. The other one occurs in the $\theta < 0°$ range when $\theta = -9°$ at normal incidence ($\alpha_\perp$).

Each range has a different mechanism of transmission or enhancement. In the $\theta > 0°$ range, for example, the nanofocusing mechanism works because the top opening slit is larger than the bottom opening slit of the taper angles, by which the incident light is focused, confined, and funneled at the bottom opening slit. However, the optical impedance matching mechanism works in the $\theta < 0°$ range. This is because the bottom opening slit of the taper angle is larger than the top opening slit of the taper angle.[80] Having the highest peaks of the enhancement at α_B in the $\theta > 0°$ range proves that a minimum reflection can be seen not only in the vertical sidewall structures but also in the tapered structures. In addition, the results show that α_B is active in the $\theta > 0°$ range, but it is inactive in the $\theta < 0°$ range. To illustrate, the resonant peaks in the two ranges occur at α_B when $\theta = 25°$ and at $\alpha_\perp$ when $\theta = -9°$.[116] Figure 4.3.24 shows plots of α in (a) and θ in (b) as a function of the optical intensity enhancement. The red, black, and green curves

in (a) represent the horizontal dashed lines in Figure 4.3.23 (b).

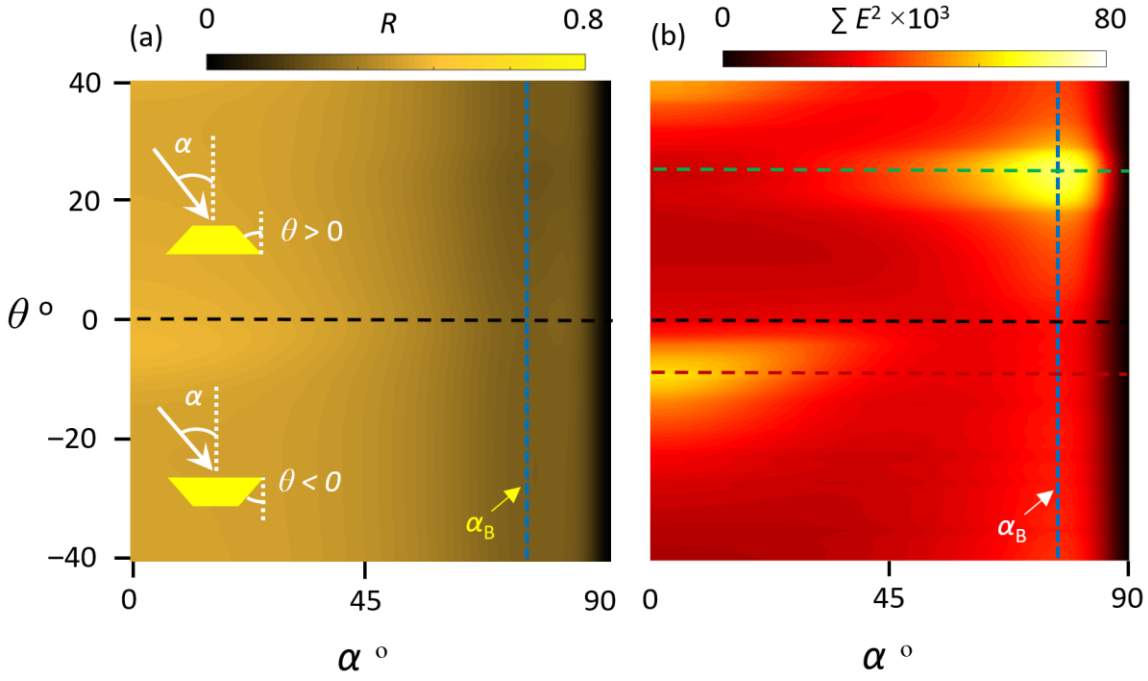

Figure 4.3.23. Color maps of reflection and optical enhancement vs. $\alpha°$ and $\theta°$.

A simple comparison is shown in Figure 4.3.24 (a) between the highest two peaks in both ranges versus α. The negative taper angle θ = -9° has the highest value at $\alpha_{\perp}$ (the red curve). The enhancement goes down as α increases. This trend could be because the top opening slit of the taper angle becomes smaller as α increases and a very small portion of the incident light transmits through the nanograting. When α reaches α_B, a small peak appears in the curve, then it drops down. The vertical sidewall angle structure is represented by the black curve. No change occurs on the enhancement until α = 60°; then, it behaves similarly to the negative taper angle. For the positive taper angle structure, the values of the enhancement are represented in the green curve; it has the highest peak value at θ = 25°. The enhancement starts with a minimum value at normal incidence, then it goes up until it records the highest peak when it reaches α_B. The enhancement gradually drops down after passing α_B. Since the highest peaks occur at $\alpha_{\perp}$ and α_B,

it is necessary to illustrate the trend of the optical enhancement versus θ at these two incidences, see Figure 4.3.24 (b).

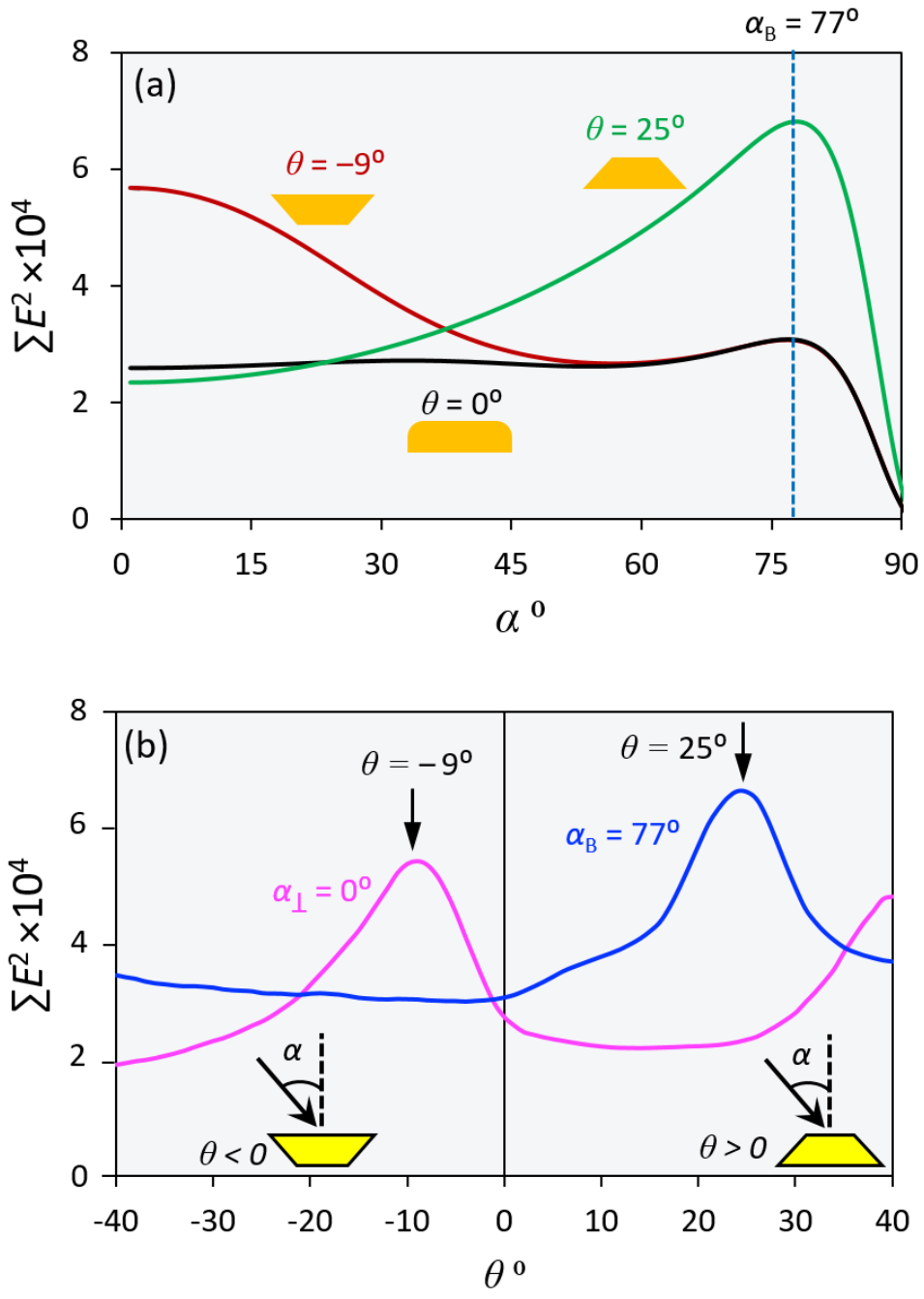

Figure 4.3.24. Plots of optical enhancement vs. α and θ° for vertical and taper angles.

The optical enhancement in the case of the positive taper angle (blue curve, θ = 25°)

increased ~22% more than that at the normal incident angle ($\alpha_{\perp}$= 0°) and optimum negative taper angle (magenta curve, θ = –9°). It increased ~120% more than that at the vertical wall. This validates the hypothesis that the positive taper angle structures can improve the enhancement more than the negative taper angle structures due to the nanofocusing mechanism. This is good because it is easier to fabricate structures with positive side wall angles as compared to negative side walls or perfectly vertical side walls.

Chapter 5.

ELECTRICAL ENHANCEMENT RESULTS

5.1 Plasmonic metal-semiconductor-metal photodetectors on GaAs

For the whole electrical enhancement section, only a single-width structure was modeled and used to determine the results. In addition, the impact of wire width (w), gap space (g), taper angle (θ), and incident wave angle (α) were examined. The thickness of the nanostructures (t_{Au}), the incident wavelength (λ_0) with p-polarization, and a bias voltage (V_{b}) were fixed at 15 nm, 875 nm, 5V, respectively. The surrounding media, substrate and superstrate, were chosen to be GaAs and air, respectively. In addition, several parameters related to semiconductor nature such as doping, bias voltage, carrier generation, recombination, and others that can enhance the current density were not taken into consideration. However, this section focuses on the parameters that enhance the incident light plasmonically, which in turn improves the weighted optical enhancement.

As mentioned previously, MSM PD consists of interdigitated electrodes separated by gap spaces and connected to two large pads, see Figure 5.1.1 (a). In addition, the figure shows the active area of the device, which is bounded by the red-dashed rectangle. Figure 5.1.1 (b) shows a 2D cross-sectional view of one period ($P = 2w + 2g$) that includes two nanowires (w), for the bias voltage requirement, and two nanogaps (g). Periodic boundary conditions were applied in the x-direction to make an infinite array. Every edge on the top surfaces of the gold nanowires was rounded with a radius of 5 nm.[123] For the structure with w = 50 nm and g = 5 nm, the normalized electric field (E_{local}/E_0) and current density (J/J_{max}) were calculated and illustrated in Figure 5.1.2 (a) and (b), respectively. Both the local electric field and the current density

hotspots are located at the same positions in the GaAs.[123] To make a correlation between the local electric field intensity and the current density, a so-called a weighted optical enhancement (G_Λ) is proposed.

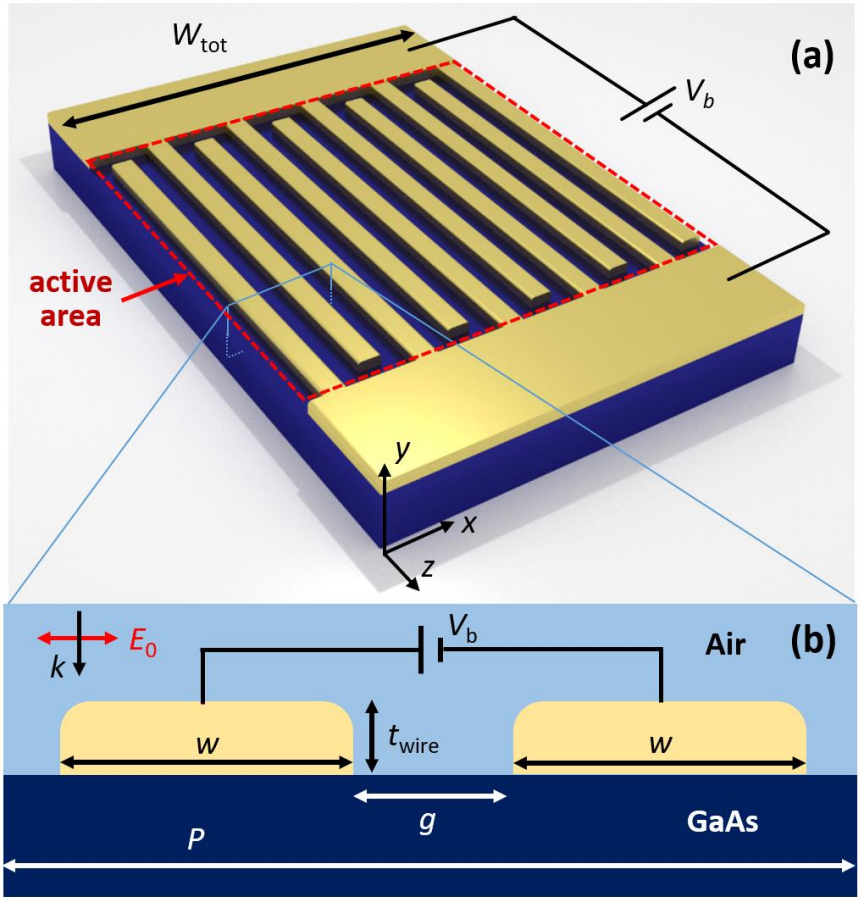

Figure 5.1.1. The proposed MSM PD (b) cross section of one period.[123]

Every single mesh point of the local optical enhancement (E_{ij}) in the GaAs substrate is weighted by the current density (J_{ij}) at the same point. As a result, more electron-hole production pairs (more current density) will be achieved when the incident light is plasmonically enhanced. For more clarification, Figure 5.1.2 (b) shows the device under no light (dark current). When the incident light hits the nanostructure, it enhances locally, and this enhancement promotes the current density. As a consequence, the photocurrent of the device will enhance as well. G_Λ

relationship can be written as follows:[123]

$$G_{\Lambda} = \sum \left[\left(\frac{E_{ij}}{E_0} \right)^2 J_{ij} \right] \Big/ \sum J_{ij} \qquad \text{(Equation 5.1)}$$

The two modules, Electromagnetic Wave, Frequency Domain (EWFD) and AC/DC Electric Current (explained in appendix H) were used to determine the values of the optical enhancement and the current density.

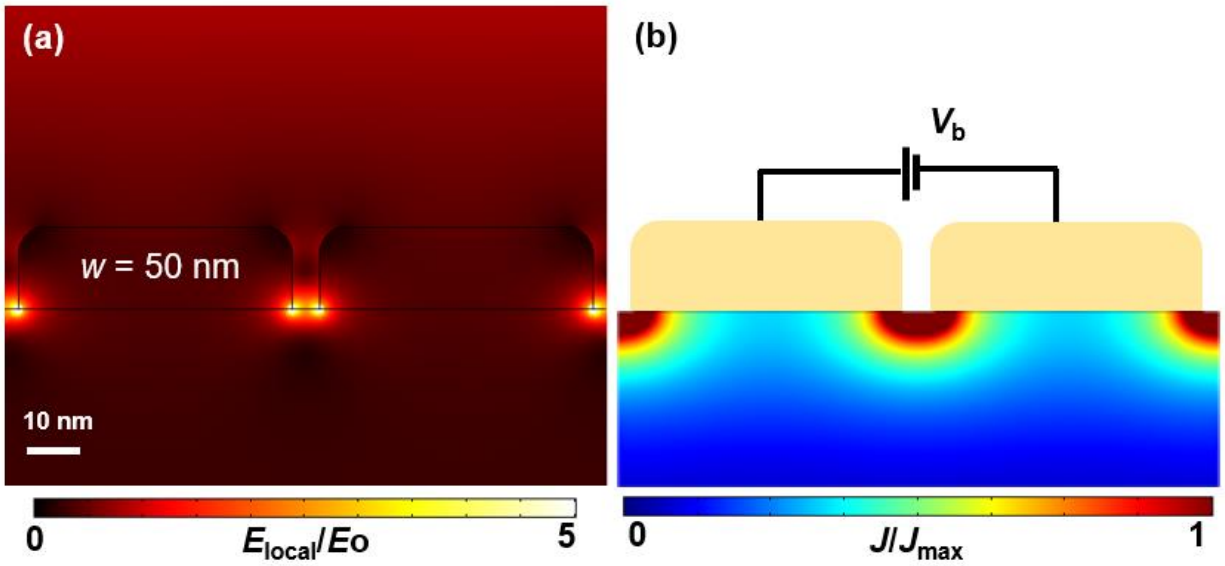

Figure 5.1.2. Electric field and current density distributions.[123]

These modules worked separately, and the results were connected by Equation 5.1 to calculate the weighted optical enhancement (G_{Λ}) for one period. The active area is supposed to be 10 x 10 μm^2 with a total width of this area (W_{tot}). This means the number of periods will increase if the period is small; then, the density of the interdigitated fingers will increase as well. Another correlation was made that connects the weighted optical enhancement (G_{Λ}) of one period with the number of periods per unit area. This correlation is called the total weighted optical enhancement (G), which is given by,[123]

$$G = G_\Lambda \left(\frac{W_{\text{tot}}}{P} - 1 \right) \qquad \text{(Equation 5.2)}$$

Equation 5.2 expresses that G depends on two factors: G_Λ and the effective number of periods $[(W_{\text{tot}}/P) - 1]$. The subtraction of one means the two electrodes at the outer edges of the active area are neglected.[123]

Figure 5.1.3 (a) and (b) are the plots of G_Λ and G, respectively, as a function of w. w was swept from 50 nm to 400 nm in 10 nm increments, and g was fixed at 5 nm. Both G_Λ and G decrease as w increases until w reaches 150 nm, then the curve goes up at w =160 nm, recording the highest peak for the remaining w values. In general, both values, G and G_Λ, in (a) and (b) go down when w increases.

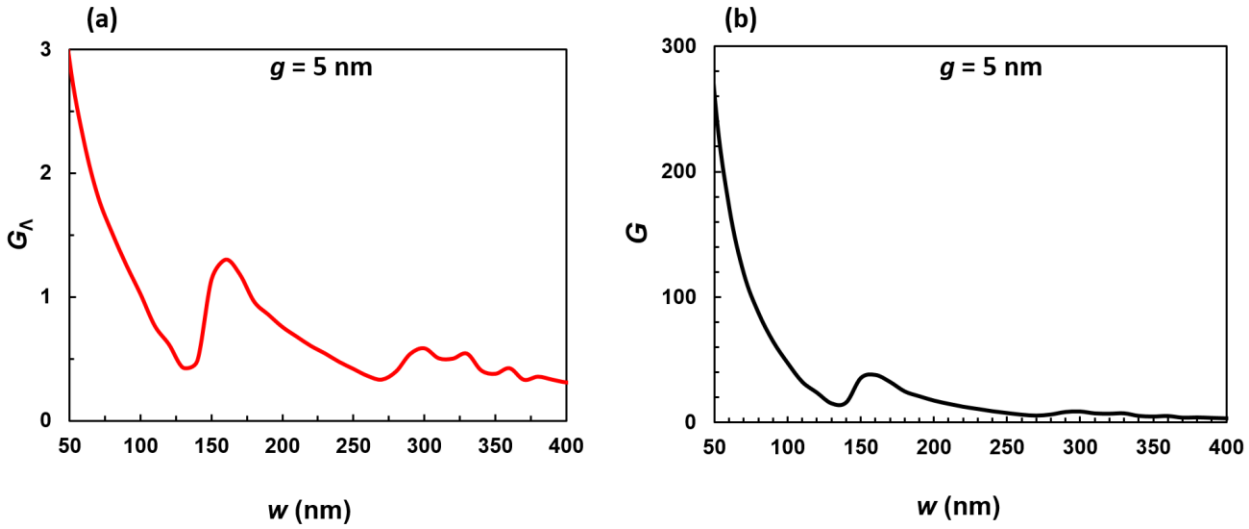

Figure 5.1.3. Plots of weighted optical enhancements vs. w for one period and the entire active area.[123]

This behavior is due to two reasons: First, increasing w leads to increasing P; hence, the effective number of periods goes down, recording small G. Second, when w increases the optical enhancement decreases as was proven by Darweesh et al and Brawley et al.[106,118] Only one

resonance peak appears at w =160 nm and this is due to the Fabry-Perot-like resonance that can generate strong coupling among the resonant plasmonic modes. Conversely, when w decreases, the optical enhancement and the effective number of periods increase and this can increase both G_Λ and G according to Equation 5.1 and Equation 5.2.[123]

The impact of g on both G_Λ and G was taken into the consideration as well. g was swept from 5 nm to 50 nm by 5 nm increments for only two wire widths, w = 50 and 160 nm. The reason behind choosing these values of w is they are resonance peaks. Figure 5.1.4 shows the plot of G versus g at the optimum w_s. In general, both G_Λ and G drop down as g increases and this is due to the plasmonic effects[106,118] and the reduction in the effective number of periods as g increases.

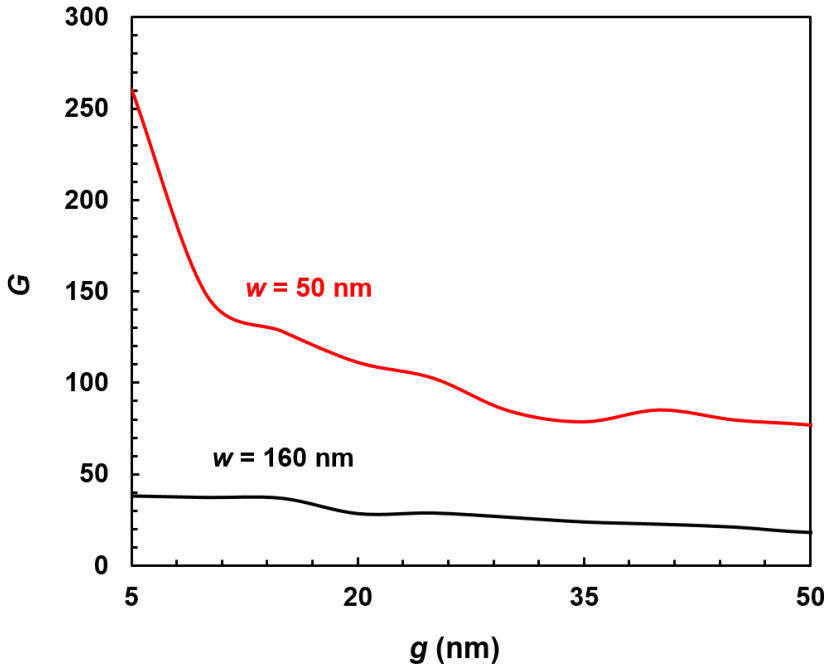

Figure 5.1.4. Plot of the total weighted optical enhancement vs. g for diferent w.[123]

At a particular w, reducing g can reduce the exposed GaAs area by the incident light because more gold covers the GaAs substrate. Figure 5.1.4 validates that smaller w and g can

improve not only the optical enhancement but also the total weighted optical enhancement (G).

In the optical enhancement results section (4.3), the impact of the two types of the taper angles (positive and negative) on the optical enhancement were studied. However, it is vitally important to study the effect of these types of taper angles on the total weighted optical enhancement (G) as well. Figure 5.1.5 is the normalized enhanced electric field, (a) and (c), and current density, (b) and (d), distributions at optimum θ and α for both ranges, $\theta > 0°$ and $\theta < 0°$, respectively.

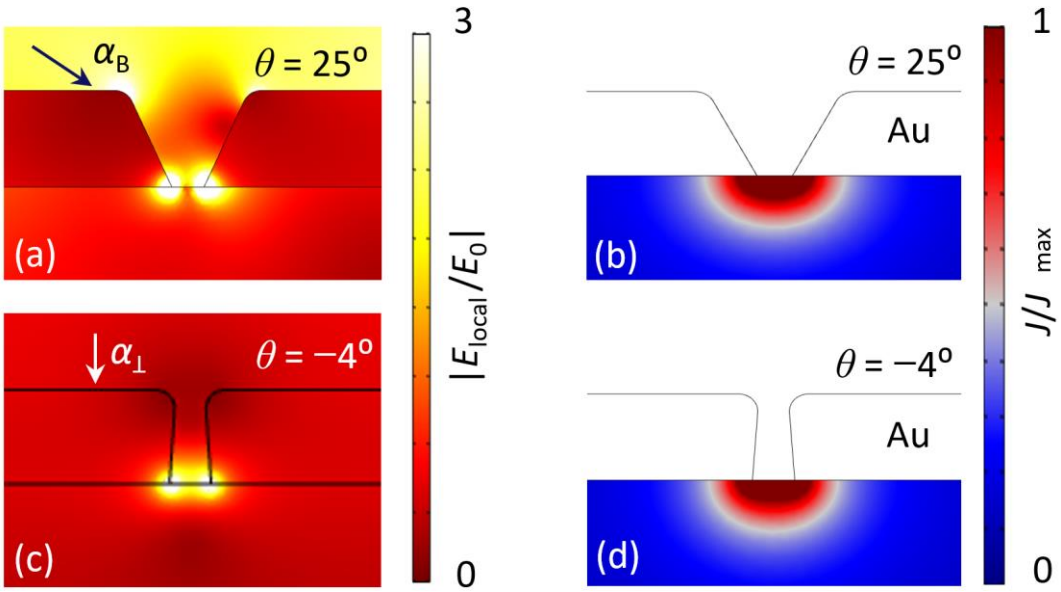

Figure 5.1.5. Electric field and current density distributions at θ = 25° and -4°.

They show that both the optical enhancement and the current density at θ = 25°, Figure 5.1.5 (a) and (b), are better than that at θ = -4°, Figure 5.1.5 (c) and (d). By calculating the optical enhancement and the current density and applying Equation 5.1 and Equation 5.2, a color map of G versus α and θ was plotted, see Figure 5.1.6. The vertical blue dashed line is the Brewster angle (α_B) position. The three horizontal dashed black, red, and green lines are the locations of the vertical sidewall angle, the optimum positive taper angle (θ = 25°), and the

optimum negative taper angle (θ = -9°).

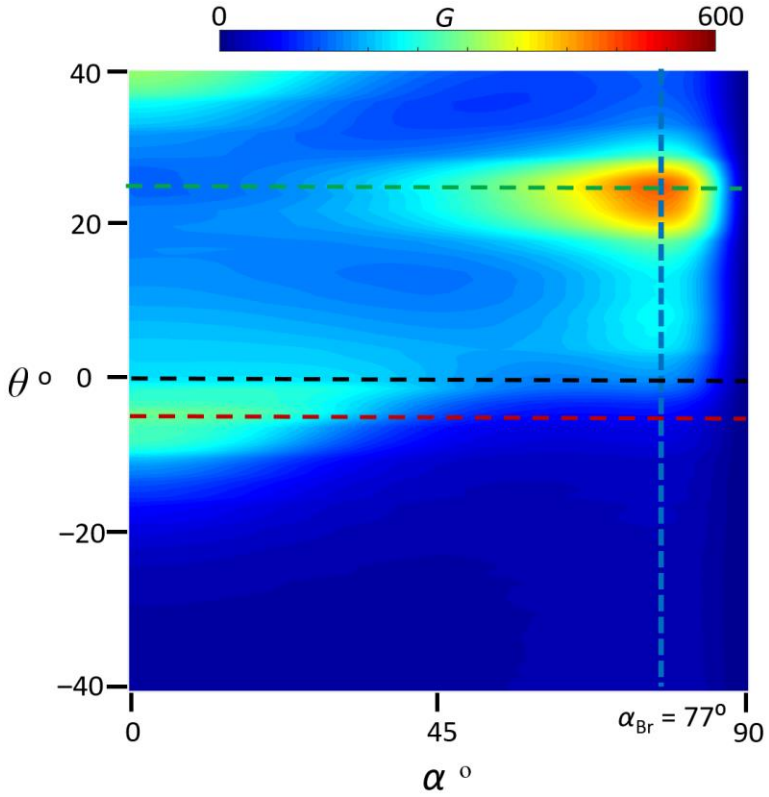

Figure 5.1.6. Color maps of optical and weighted optical enhancements vs. α° and θ°.

The highest peak of G is located at the same position as the highest peak of the optical enhancement in Figure 4.3.23 (b), in the $\theta > 0°$ range. However, G shifts a bit in the $\theta < 0°$ range and becomes θ = -4° instead of θ = -9° as in Figure 4.3.23 (b). This shift could be attributed to the reduction of the nanowire's bases at the GaAs-Au interface when the bottom opening slit increases to create the negative taper angles. These bases, however, are constant in the case of creating the positive taper angle. Because of this, Figure 5.1.6 shows that G is weak in the $\theta > 0°$ range, especially when $\theta > 10°$. In addition, no significant effect was noticed at $\alpha > 30°$, especially at α_{Br}. On the other hand, G in Figure 5.1.6 and the optical enhancement in Figure 4.3.23 (b) in the $\theta > 0°$ range are comparable. Again, this is due to the fixed bases of the

nanowires.

Figure 5.1.7 shows the plots of G as a function of α in (a) and θ in (b). The three dashed lines, red, black, and green at θ = -4°, 0°, and 25°, respectively, in Figure 5.1.6, are represented as the points of interest.

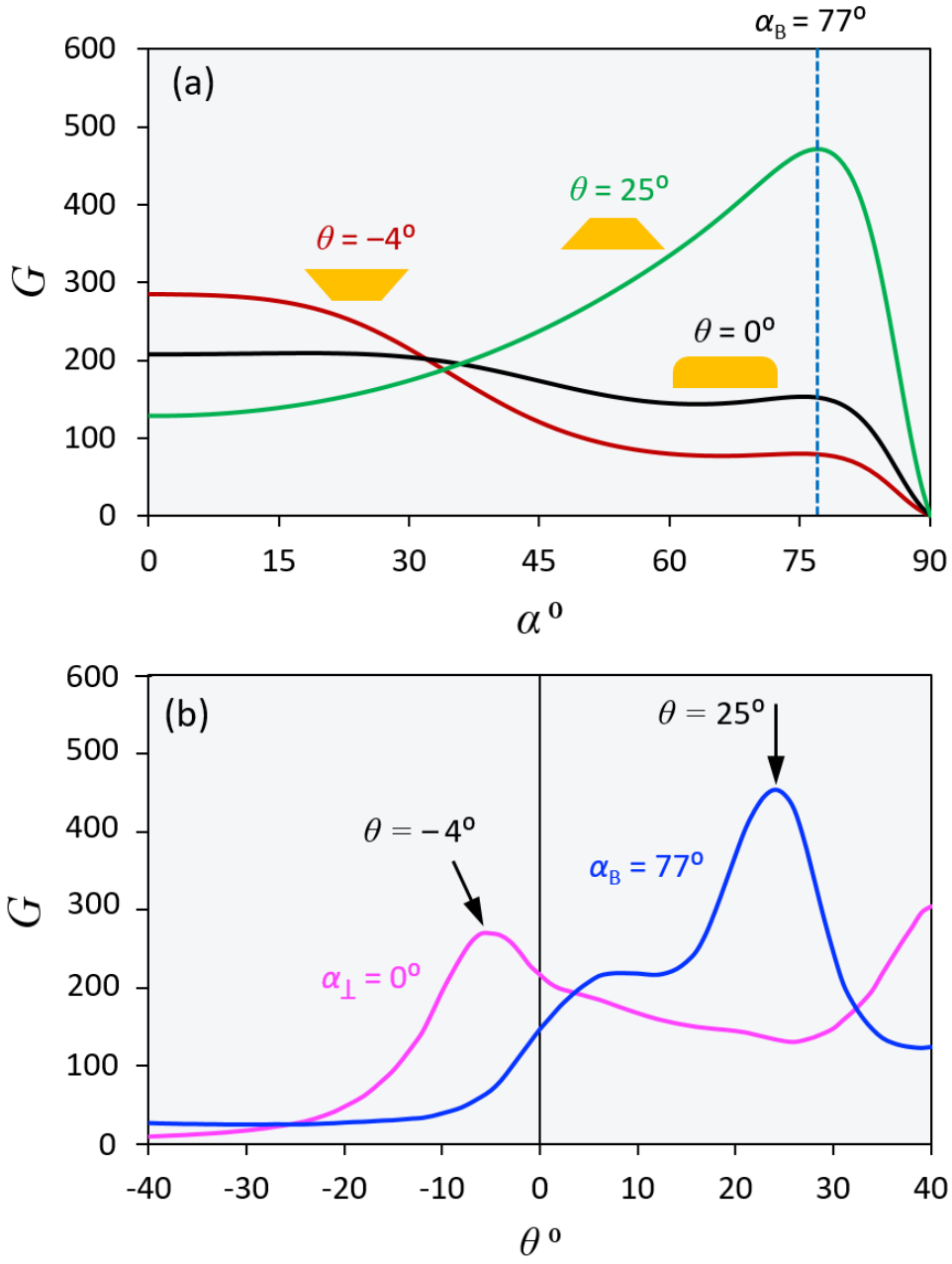

Figure 5.1.7. Plots of weighted optical enhancement vs. (a) α° and (b) θ°.

At both θ = -4° and 0°, G decreases as α increases and no improvement in the G values were recorded at α_{B}. At θ = 25°, however, G increases as α increases until it reaches the peak at α_{B}. Then G drops down because the optical enhancement becomes weak and approaches the zero value in this range.

Since the two peaks are located at $\alpha_{\perp}$ and α_{Br}, it is important to see the effect of θ on these two incidences, see Figure 5.1.7 (b). When θ = -4° and 25° (magenta and blue curves), G increased ~25% and ~120% more than that at the vertical sidewall structures, respectively. In addition, G at the resonant peak in the $\theta > 0°$ range (θ = 25°) increases ~120% more than that at at the resonant peaks in the $\theta < 0°$ range (θ = -4°). As a result, the positive taper angle nanostructures can enhance the incident electric field (E_{local}) and the total weighted optical enhancement (G) more than the negative taper angle nanostructures.

Chapter 6.

CONCLUSION AND FUTURE WORK

COMSOL Multiphysics was operated to design and calculate the enhanced electric field and current density by nanograting structures. A relationship was made that connects two modules and calculates the optical and the so-called total weighted optical enhancements of the metal-semiconductor-metal photodetectors. Several factors were studied in this work that can affect the enhancements of the incident light and the current density of metal-semiconductor-metal photodetectors. These factors are: wire width and thickness, gap space, taper angle, and the incident wavelength and angle. Nanograting, as a plasmonic excitation technique, was used to enhance the efficiency of the proposed device. The nanograting was laid on different types of substrates, SiO2, Ti/Sio2/Si, and GaAs.

The results showed the dependency of the enhancements on the period structure of the nanograting. Since the period of the nanograting, single and dual-widths, is a function of gap space and wire widths, the impact of these variables was carefully examined. Interesting enhancement peaks were revealed that appeared on the optical and electrical spectra. It has proven that the dual-width nanograting structure can increase optical enhancement more than two times compared to that of the single-width structure. In addition, a deep study was conducted on the impact of tapered nanostructures on the enhancements. The tapered nanostructures can give more enhancement than vertical sidewall structures. In addition to the taper angle effects, the incident light angle further affects the overall device performance. To illustrate, the enhanced electric field intensity at the Brewster angle ($\alpha_B = 77°$) for the optimum positive taper angle ($\theta = 25°$) increased ~22% and ~120% more than those measured for normal incidence ($\alpha_\perp = 0°$) with

an optimum negative taper angle (θ = –9°) and for the vertical wall structure, respectively. In the case of θ = 25°, however, the total weighted optical enhancement is ~65% greater than for the optimal negative taper angle (θ = –4°). In addition, it is ~120% greater than for the vertical side wall structures. Finally, it was found that a very thin layer of titanium (1 nm) as adhesive material can significantly eliminate the plasmonic effects.

For the entire dissertation, only mono-metallic (gold) nanograting structures were used to determine the enhancements. In future work, however, one could use different plasmonic materials as mono- or bi-metallic nanostructures, such as Au, Ag, Al, Cu, Ti, Pd, and Ni. The proposed structures could be modeled as 3D simulation models and meta-surface structures created. Moreover, the roughness effects of the metallic nanostructure surface could be modeled and studied to determine the optical enhancements. In addition, it would be possible to study the optical response and optimize the filled nano-gap grating structures with nanoparticles.

REFERENCES

1. Downs, C. & Vandervelde, T. E. Progress in Infrared Photodetectors Since 2000. *Sensors* **13**, 5054–5098 (2013).

2. Albert, A. & Gege, P. Inversion of irradiance and remote sensing reflectance in shallow water between 400 and 800 nm for calculations of water and bottom properties. *Appl. Opt.* **45**, 2331–2343 (2006).

3. Wu, P., Dai, Y., Ye, Y., Yin, Y. & Dai, L. Fast-speed and high-gain photodetectors of individual single crystalline Zn3P2 nanowires. *J. Mater. Chem.* **21**, 2563–2567 (2011).

4. Rogalski, A. Infrared detectors: an overview. *Infrared Phys. Technol.* **43**, 187–210 (2002).

5. Weissleder, R., Tung, C.-H., Mahmood, U., & Jr, Alexei B. In vivo imaging of tumors with protease-activated near-infrared fluorescent probes. *Nat. Biotechnol.* **17**, 375–378 (1999).

6. Izzetoglu, M., Bunce, S. C., Izzetoglu, K., Onaral, B. & Pourrezaei, K. Functional brain imaging using near-infrared technology. *IEEE Eng. Med. Biol. Mag. Q. Mag. Eng. Med. Biol. Soc.* **26**, 38–46 (2007).

7. Tan, C. L., Lysak, V. V., Alameh, K. & Lee, Y. T. Absorption enhancement of 980 nm MSM photodetector with a plasmonic grating structure. *Opt. Commun.* **283**, 1763–1767 (2010).

8. Choy, J. T., Bulu, I., Hausmann, B., Janitz, E., Huang, I., & Lončar, M., Spontaneous emission and collection efficiency enhancement of single emitters in diamond via plasmonic cavities and gratings. *Appl. Phys. Lett.* **103**, 161101 (2013).

9. Sobhani, A., Knight, M., Wang, Y., Zheng, B., King, N., Brown, L., Fang, Z., Nordlander, P., & Halas, N. Narrowband photodetection in the near-infrared with a plasmon-induced hot electron device. *Nat. Commun.* **4**, 1643 (2013).

10. Mishima, Y., Habara, H. & Tanaka, K. A. Two plasmonic mode excitation using a double-step rectangle grating. *JOSA B* **32**, 1804–1808 (2015).

11. Alaee, R. Lehr, D., Filter, R., Lederer, F., Kley, E., Rockstuhl, C., & Tünnermann, A. Scattering Dark States in Multiresonant Concentric Plasmonic Nanorings. *ACS Photonics* **2**, 1085–1090 (2015).

12. Rahbany, N., Geng, W., Blaize, S., Salas-Montiel, R., Bachelot, R., & Couteau, C. Integrated plasmonic double bowtie / ring grating structure for enhanced electric field confinement. *Nanospectroscopy* **1**, (2015).

13. Rahbany, N., Geng, W. Blaize, S., Salas-Montiel, R., de la Cruz, S., Méndez, E., Blaize, S., Bachelot, R., & Couteau, C. A Concentric Plasmonic Platform for the Efficient Excitation of Surface Plasmon Polaritons. *Plasmonics* **11**, 175–182 (2016).

14. Bantz, K. C., Meyer, C., Wittenberg, N., Im, H., Kurtuluş, O., Lee, S., Lindquist, N., Oh, S., & Haynes, C. Recent progress in SERS biosensing. *Phys. Chem. Chem. Phys.* **13**, 11551–11567 (2011).

15. Im, H., Bantz, K., Lee, S., Johnson, T., Haynes, C., & Oh, S. Self-Assembled Plasmonic Nanoring Cavity Arrays for SERS and LSPR Biosensing. *Adv. Mater.* **25**, 2678–2685 (2013).

16. Clark, A. W. & Cooper, J. M. Nanogap Ring Antennae as Plasmonically Coupled SERRS Substrates. *Small* **7**, 119–125 (2011).

17. Yue, W., Wang, Z., Yang, Y., Chen, L., Syed, A., Wong, K., & Wang, X. Electron-beam lithography of gold nanostructures for surface-enhanced Raman scattering. *J. Micromechanics Microengineering* **22**, 125007 (2012).

18. Abb, M., Wang, Y., Papasimakis, N., de Groot, C. H. & Muskens, O. L. Surface-Enhanced Infrared Spectroscopy Using Metal Oxide Plasmonic Antenna Arrays. *Nano Lett.* **14**, 346–352 (2014).

19. Zhang, Y., Zhen, Y., Neumann, O., Day, J., Day, P., & Halas, N. Coherent anti-Stokes Raman scattering with single-molecule sensitivity using a plasmonic Fano resonance. *Nat. Commun.* **5**, 4424 (2014).

20. Çetin, A. E., Güven, K. & Müstecaplıoğlu, Ö. E. Active control of focal length and beam deflection in a metallic nanoslit array lens with multiple sources. *Opt. Lett.* **35**, 1980–1982 (2010).

21. Tanemura, T., Balram, K., Ly-Gagnon, D., Wahl, P., White, J., Brongersma, M., & Miller, D. Multiple-Wavelength Focusing of Surface Plasmons with a Nonperiodic Nanoslit Coupler. *Nano Lett.* **11**, 2693–2698 (2011).

22. Verslegers, L., Catrysse, P., Yu, Z., White, J., Barnard, E., Brongersma, M., & Fan, S. Planar Lenses Based on Nanoscale Slit Arrays in a Metallic Film. *Nano Lett.* **9**, 235–238 (2009).

23. Iwami, K., Ishii, M., Kuramochi, Y., Ida, K. & Umeda, N. Ultrasmall radial polarizer array based on patterned plasmonic nanoslits. *Appl. Phys. Lett.* **101**, 161119 (2012).

24. Sonntag, M. D., Klingsporn, J., Zrimsek, A., Sharma, B., Ruvuna, L., & Duyne, R. Molecular plasmonics for nanoscale spectroscopy. *Chem. Soc. Rev.* **43**, 1230–1247 (2014).

25. Gordon, R., Sinton, D., Brolo, A. G. & Kavanagh, K. L. Plasmonic sensors based on nano-holes: technology and integration. in *Micro (MEMS) and Nanotechnologies for Space, Defense, and Security II* **6959**, 695913 (International Society for Optics and Photonics, 2008).

26. Herzog, J. B., Knight, M., Li, Y., Evans, K., Halas, N., & Natelson, D. Dark Plasmons in Hot Spot Generation and Polarization in Interelectrode Nanoscale Junctions. *Nano Lett.* **13**, 1359–1364 (2013).

27. Zheng, B. Y., Wang, Y., Nordlander, P. & Halas, N. J. Color-Selective and CMOS-Compatible Photodetection Based on Aluminum Plasmonics. *Adv. Mater.* **26**, 6318–6323 (2014).

28. Knight, M. W., Sobhani, H., Nordlander, P. & Halas, N. J. Photodetection with Active Optical Antennas. *Science* **332**, 702–704 (2011).

29. Chang, C.-C., Sharma, Y., Kim, Y., Bur, J., Shenoi, R., Krishna, S., Huang, D., & Lin, S. A Surface Plasmon Enhanced Infrared Photodetector Based on InAs Quantum Dots. *Nano Lett.* **10**, 1704–1709 (2010).

30. Ferry, V. E., Verschuuren, M., Li, H., Verhagen, E., Walters, R., Schropp, R., Atwater, H., & Polman, A. Light trapping in ultrathin plasmonic solar cells. *Opt. Express* **18**, A237–A245 (2010).

31. Pillai, S. & Green, M. A. Plasmonics for photovoltaic applications. *Sol. Energy Mater. Sol. Cells* **94**, 1481–1486 (2010).

32. Lal, N. N., Soares, B., Sinha, K., Huang, F., Mahajan, S., Bartlett, P., Greenham, N., & Baumberg, J. Enhancing solar cells with localized plasmons in nanovoids. *Opt. Express* **19**, 11256–11263 (2011).

33. Yu, R., Lin, Q., Leung, S.-F. & Fan, Z. Nanomaterials and nanostructures for efficient light absorption and photovoltaics. *Nano Energy* **1**, 57–72 (2012).

34. Massiot, I., Vandamme, N., Bardou, N., Dupuis, C., Lemaître, A., Guillemoles, J., & Collin, S. Metal Nanogrid for Broadband Multiresonant Light-Harvesting in Ultrathin GaAs Layers. *ACS Photonics* **1**, 878–884 (2014).

35. Rifat, A. A., Ahmed, R., Yetisen, A., Butt, H., Sabouri, A., Mahdiraji, A., Yun, S., & Adikan, M. Photonic crystal fiber based plasmonic sensors. *Sens. Actuators B Chem.* **243**, 311–325 (2017).

36. Kristensen, A., Yang, J., Bozhevolnyi, S., Link, S., Nordlander, P., Halas, N., & Mortensen, A. Plasmonic colour generation. *Nat. Rev. Mater.* **2**, 16088 (2017).

37. Ogawa, S., Fujisawa, D., Hata, H., Uetsuki, M., Kuboyama, T., & Kimata, M. High-performance mushroom plasmonic metamaterial absorbers for infrared polarimetric imaging. in *Infrared Technology and Applications XLIII* **10177**, 101771S (International Society for Optics and Photonics, 2017).

38. Wenger, T., Viola, G., Kinaret, J., Fogelström, M. & Tassin, P. High-sensitivity plasmonic refractive index sensing using graphene. *2D Mater.* **4**, 025103 (2017).

39. Wark, A. W., Lee, H. J., Qavi, A. J. & Corn, R. M. Nanoparticle-Enhanced Diffraction Gratings for Ultrasensitive Surface Plasmon Biosensing. *Anal. Chem.* **79**, 6697–6701 (2007).

40. Byun, K. M., Yoon, S. J., Kim, D. & Kim, S. J. Experimental study of sensitivity enhancement in surface plasmon resonance biosensors by use of periodic metallic nanowires. *Opt. Lett.* **32**, 1902–1904 (2007).

41. Dostálek, J. & Homola, J. Surface plasmon resonance sensor based on an array of diffraction gratings for highly parallelized observation of biomolecular interactions. *Sens. Actuators B Chem.* **129**, 303–310 (2008).

42. Lee, H. J., Wark, A. W. & Corn, R. M. Enhanced bioaffinity sensing using surface plasmons, surface enzyme reactions, nanoparticles and diffraction gratings. *Analyst* **133**, 596–601 (2008).

43. Daghestani, H. N. & Day, B. W. Theory and Applications of Surface Plasmon Resonance, Resonant Mirror, Resonant Waveguide Grating, and Dual Polarization Interferometry Biosensors. *Sensors* **10**, 9630–9646 (2010).

44. Janunts, N. A., Baghdasaryan, K. S., Nerkararyan, K. V. & Hecht, B. Excitation and superfocusing of surface plasmon polaritons on a silver-coated optical fiber tip. *Opt. Commun.* **253**, 118–124 (2005).

45. Lin, Y., Zou, Y., Mo, Y., Guo, J. & Lindquist, R. G. E-Beam Patterned Gold Nanodot Arrays on Optical Fiber Tips for Localized Surface Plasmon Resonance Biochemical Sensing. *Sensors* **10**, 9397–9406 (2010).

46. Verma, R. K., Sharma, A. K. & Gupta, B. D. Surface plasmon resonance based tapered fiber optic sensor with different taper profiles. *Opt. Commun.* **281**, 1486–1491 (2008).

47. Michel, D., Xiao, F. & Alameh, K. A compact, flexible fiber-optic Surface Plasmon Resonance sensor with changeable sensor chips. *Sens. Actuators B Chem.* **246**, 258–261 (2017).

48. Maier, S. A. *Plasmonics: Fundamentals and Applications*. pp. 1-75, (Springer Science & Business Media, 2007).

49. Maier, S. A. Electromagnetics of Metals. in *Plasmonics: Fundamentals and Applications* (ed. Maier, S. A.) 5–19 (Springer US, 2007). doi:10.1007/0-387-37825-1_1

50. Griffiths, D. J. & Inglefield, C. *Introduction to Electrodynamics*. *Am. J. Phys.* **73**, 574–574 (2005).

51. F, R. W. *Nonlinear Optics*. pp 589-604 (Elsevier, 2003).

52. Jackson, J. D. Classical Electrodynamics, 3rd ed. *Am. J. Phys.* **67**, 841–842 (1999).

53. Readings | Electromagnetic Energy: From Motors to Lasers | Electrical Engineering and Computer Science | MIT OpenCourseWare. Available at: https://ocw.mit.edu/courses/electrical-engineering-and-computer-science/6-007-electromagnetic-energy-from-motors-to-lasers-spring-2011/readings/. (Accessed: 13th December 2018)

54. Drude, P. Zur Elektronentheorie der Metalle. *Ann. Phys.* **306**, 566–613 (1900).

55. Sarkar, P., Panda, S., Maji, B. & Mukhopadhyay, A. K. Comparative study of Au and Ag nanoparticle to improved in absorption in plasmonic solar cell. in *2017 Devices for Integrated Circuit (DevIC)* 175–179 (2017). doi:10.1109/DEVIC.2017.8073931

56. Ru, E. L. & Etchegoin, P. *Principles of Surface-Enhanced Raman Spectroscopy: and Related Plasmonic Effects*. pp. 1-250 (Elsevier, 2008).

57. Pernice, W. H. P., Payne, F. P. & Gallagher, D. F. G. Numerical investigation of field enhancement by metal nano-particles using a hybrid FDTD-PSTD algorithm. *Opt. Express* **15**, 11433–11443 (2007).

58. (10) (PDF) Molding of Plasmonic Resonances in Metallic Nanostructures: Dependence of the Non-Linear Electric Permittivity on System Size and Temperature. *ResearchGate* Available at: https://www.researchgate.net/publication/267638767_Molding_of_Plasmonic_Resonances_in_Metallic_Nanostructures_Dependence_of_the_Non-Linear_Electric_Permittivity_on_System_Size_and_Temperature. (Accessed: 13th December 2018)

59. Zayats, A. V., Smolyaninov, I. I. & Maradudin, A. A. Nano-optics of surface plasmon polaritons. *Phys. Rep.* **408**, 131–314 (2005).

60. Karar, A. A. Surface plasmons for enhanced metal-semiconductor-metal photodetectors. (Doctoral dissertation), Edith Cowan University. Retrieved from http://ro.ecu.edu.au/cgi/viewcontent.cgi?article=1594&context=theses. pp (10-24 & 91-93).

61. Weiner, J. The physics of light transmission through subwavelength apertures and aperture arrays. *Rep. Prog. Phys.* **72**, 064401 (2009).

62. Barnes, W. L. Surface plasmon–polariton length scales: a route to sub-wavelength optics. *J. Opt. Pure Appl. Opt.* **8**, S87 (2006).

63. Popov, E. Introduction to Diffraction Gratings: Summary of Applications. in *Gratings: Theory and Numeric Applications* (ed. Popov, E.) 1.1-1.23 (AMU (PUP), 2012).

64. Rumpf, R. C. & Johnson, E. G. Modeling fabrication to accurately place GMR resonances. *Opt. Express* **15**, 3452–3464 (2007).

65. Strutt John William. On the dynamical theory of gratings. *Proc. R. Soc. Lond. Ser. Contain. Pap. Math. Phys. Character* **79**, 399–416 (1907).

66. Lord Rayleigh M. III. Note on the remarkable case of diffraction spectra described by Prof. Wood. *Lond. Edinb. Dublin Philos. Mag. J. Sci.* **14**, 60–65 (1907).

67. Kabashin, A. V., Evans, P., Pastkovsky, S., Hendren, W., Wurtz, A., Atkinson, R., Pollard, R., Podolskiy, A., & Zayats, V. Plasmonic nanorod metamaterials for biosensing. *Nat. Mater.* **8**, 867–871 (2009).

68. Homola, J. Present and future of surface plasmon resonance biosensors. *Anal. Bioanal. Chem.* **377**, 528–539 (2003).

69. Abdulhalim, I., Zourob, M. & Lakhtakia, A. Surface Plasmon Resonance for Biosensing: A Mini-Review. *Electromagnetics* **28**, 214–242 (2008).

70. Maystre, D. Theory of Wood's Anomalies. in *Plasmonics: From Basics to Advanced Topics* (eds. Enoch, S. & Bonod, N.) 39–83 (Springer Berlin Heidelberg, 2012). doi:10.1007/978-3-642-28079-5_2

71. Anker, J. N., Hall, W., Lyandres, O., Shah. N., Zhao, J., & Van Duyne, R. Biosensing with plasmonic nanosensors. in *Nanoscience and Technology* 308–319 (Co-Published with Macmillan Publishers Ltd, UK, 2009). doi:10.1142/9789814287005_0032

72. Savoia, S., Ricciardi, A., Crescitelli, A., Granata, C., Esposito, E., Galdi, V., & Cusano, A. Surface sensitivity of Rayleigh anomalies in metallic nanogratings. *Opt. Express* **21**, 23531–23542 (2013).

73. Huang, X.-R. & Peng, R.-W. General mechanism involved in subwavelength optics of conducting microstructures: charge-oscillation-induced light emission and interference. *JOSA A* **27**, 718–729 (2010).

74. Porto, J. A., García-Vidal, F. J. & Pendry, J. B. Transmission Resonances on Metallic Gratings with Very Narrow Slits. *Phys. Rev. Lett.* **83**, 2845–2848 (1999).

75. Cao, Q. & Lalanne, P. Negative Role of Surface Plasmons in the Transmission of Metallic Gratings with Very Narrow Slits. *Phys. Rev. Lett.* **88**, 057403 (2002).

76. Jiao, X., Wang, P., Tang, L., Lu, Y., Li, Q., Zhang, D., Yao, P., Ming H., & Xie, J. Fabry–Pérot-like phenomenon in the surface plasmons resonant transmission of metallic gratings with very narrow slits. *Appl. Phys. B* **80**, 301–305 (2005).

77. Beermann, J., Søndergaard, T., Novikov, S., Bozhevolnyi, S., Devaux, E., & Ebbesen, T. Field enhancement and extraordinary optical transmission by tapered periodic slits in gold films. *New J. Phys.* **13**, 063029 (2011).

78. Søndergaard, T., Bozhevolnyi, S., Novikov, S., Beermann, J., Devaux, E., & Ebbesen, T. Extraordinary optical transmission with tapered slits: effect of higher diffraction and slit resonance orders. *JOSA B* **29**, 130–137 (2012).

79. Søndergaard, T., Bozhevolnyi, S., Beermann, J., Novikov, S., Devaux, E., & Ebbesen, T. Resonant Plasmon Nanofocusing by Closed Tapered Gaps. *Nano Lett.* **10**, 291–295 (2010).

80. Søndergaard, T., Bozhevolnyi, S., Novikov, S., Beermann, J., Devaux, E., & Ebbesen, T. Extraordinary Optical Transmission Enhanced by Nanofocusing. *Nano Lett.* **10**, 3123–3128 (2010).

81. Shen, H. & Maes, B. Enhanced optical transmission through tapered metallic gratings. *Appl. Phys. Lett.* **100**, 241104 (2012).

82. Argyropoulos, C., D'Aguanno, G., Mattiucci, N., Akozbek, N., Bloemer M., & Alù, A. Matching and funneling light at the plasmonic Brewster angle. *Phys. Rev. B* **85**, 024304 (2012).

83. Le, K. Q. Enhanced plasmonic Brewster transmission through metascreens by tapered slits. *J. Appl. Phys.* **115**, 033110 (2014).

84. Alù, A., D'Aguanno, G., Mattiucci, N. & Bloemer, M. J. Plasmonic Brewster Angle: Broadband Extraordinary Transmission through Optical Gratings. *Phys. Rev. Lett.* **106**, 123902 (2011).

85. Le, K. Q., Argyropoulos, C., Mattiucci N., D'Aguanno, G., Bloemer, M., & Alù, A. Broadband Brewster transmission through 2D metallic gratings. *J. Appl. Phys.* **112**, 094317 (2012).

86. Argyropoulos, C., Le, K. Q., Mattiucci, N., D'Aguanno, G. & Alù, A. Broadband absorbers and selective emitters based on plasmonic Brewster metasurfaces. *Phys. Rev. B* **87**, 205112 (2013).

87. Sze, S. M. & Ng, K. K. *Physics of Semiconductor Devices*. pp. 663-742, (John Wiley & Sons, 2006).

88. Kashyap, R. & Nemova, G. Surface Plasmon Resonance-Based Fiber and Planar Waveguide Sensors. *Journal of Sensors* (2009). doi:10.1155/2009/645162

89. Sugeta, T. & Urisu, T. WP-B2 high-gain metal—Semiconductor—Metal photodetectors for high-speed optoelectronic circuits. *IEEE Trans. Electron Devices* **26**, 1855–1856 (1979).

90. Figueroa, L. & Slayman, C. W. A novel heterostructure interdigital photodetector (HIP) with picosecond optical response. *IEEE Electron Device Lett.* **2**, 208–210 (1981).

91. Slayman, C. W. & Figueroa, L. Frequency and pulse response of a novel high-speed interdigital surface photoconductor (IDPC). *IEEE Electron Device Lett.* **2**, 112–114 (1981).

92. Wei, C. J., Klein, H.- & Beneking, H. Symmetrical Mott barrier as a fast photodetector. *Electron. Lett.* **17**, 688–690 (1981).

93. Sano, E. A device model for metal-semiconductor-metal photodetectors and its applications to optoelectronic integrated circuit simulation. *IEEE Trans. Electron Devices* **37**, 1964–1968 (1990).

94. Burm, J., Litvin, K. I., Schaff, W. J. & Eastman, L. F. Optimization of high-speed metal-semiconductor-metal photodetectors. *IEEE Photonics Technol. Lett.* **6**, 722–724 (1994).

95. Nusir, A. I., Hill, A. M., Manasreh, M. O. & Herzog, J. B. Near-infrared metal-semiconductor-metal photodetector based on semi-insulating GaAs and interdigital electrodes. *Photonics Res.* **3**, 1–4 (2015).

96. Karar, A., Tan, C. L., Alameh, K., Lee, Y. T. & Karouta, F. Metal Nano-Grating Optimization for Higher Responsivity Plasmonic-Based GaAs Metal-Semiconductor-Metal Photodetector. *J. Light. Technol.* **31**, 1088–1092 (2013).

97. Das, N., Karar, A., Tan, C., Vasiliev, M., Alameh, K., & Lee, Y. Metal-semiconductor-metal (MSM) photodetectors with plasmonic nanogratings*. *Pure Appl. Chem.* **83**, 2107–2113 (2011).

98. Tan, C. L., Lysak, V., Das, N., Karar, A., Alameh, K., & Lee, Y. Absorption enhancement of MSM photodetector structure with a plasmonic double grating structure. in *10th IEEE International Conference on Nanotechnology* 849–853 (2010). doi:10.1109/NANO.2010.5697989

99. COMSOL Multiphysics® Modeling Software. Available at: https://www.comsol.com/. (Accessed: 13th March 2019)

100. Darweesh, A. A., Bauman, S. J. & Herzog, J. B. Improved optical enhancement using double-width plasmonic gratings with nanogaps. *Photonics Res.* **4**, 173–180 (2016).

101. Guo, J., Tu, Y., Yang, L., Wang, L. & Wang, B. Design of a double grating-coupled surface plasmon color filter. in *Optical Components and Materials XIII* **9744**, 97440C (International Society for Optics and Photonics, 2016).

102. Hall, A. S., Faryad, M., Barber, G. D., Lakhtakia, A. & Mallouk, T. E. Effect of grating period on the excitation of multiple surface-plasmon-polariton waves guided by the interface of a metal grating and a photonic crystal. in *Physics, Simulation, and Photonic Engineering of Photovoltaic Devices II* **8620**, 862003 (International Society for Optics and Photonics, 2013).

103. Lin, C.-H., Hsieh, C., Tu, C., Kuo, Y., Chen, H., Shih, P., Liao, C., Kiang, Y., Yang, C., Lai. C., He, G., Yeh, J., & Hsu. T. Efficiency improvement of a vertical light-emitting diode through surface plasmon coupling and grating scattering. *Opt. Express* **22**, A842–A856 (2014).

104. Xiong, X. H., Zhan, L. M. & Ke, X. Effects of Grating Slant Angle on Surface Plasmon Resonance and its Applications for Sensors. *Applied Mechanics and Materials* (2014). doi:10.4028/www.scientific.net/AMM.536-537.342

105. Liu, F. & Zhang, X. Fano coupling between Rayleigh anomaly and localized surface plasmon resonance for sensor applications. *Biosens. Bioelectron.* **68**, 719–725 (2015).

106. Darweesh, A. A., Bauman, S. J., Brawley, Z. T. & Herzog, J. B. Improved optical enhancement in binary plasmonic gratings with nanogap spacing. in *Nanoengineering: Fabrication, Properties, Optics, and Devices XIII* **9927**, 99270Z (International Society for Optics and Photonics, 2016).

107. Prodan, E., Radloff, C., Halas, N. J. & Nordlander, P. A Hybridization Model for the Plasmon Response of Complex Nanostructures. *Science* **302**, 419–422 (2003).

108. Nordlander, P., Oubre, C., Prodan, E., Li, K. & Stockman, M. I. Plasmon Hybridization in Nanoparticle Dimers. *Nano Lett.* **4**, 899–903 (2004).

109. Brandl, D. W., Oubre, C. & Nordlander, P. Plasmon hybridization in nanoshell dimers. *J. Chem. Phys.* **123**, 024701 (2005).

110. Ward, D. R., Hüser, F., Pauly, F., Cuevas, J. C. & Natelson, D. Optical rectification and field enhancement in a plasmonic nanogap. *Nat. Nanotechnol.* **5**, 732–736 (2010).

111. García-Martín, A., Ward, D. R., Natelson, D. & Cuevas, J. C. Field enhancement in subnanometer metallic gaps. *Phys. Rev. B* **83**, 193404 (2011).

112. Kawawaki, T., Takahashi, Y. & Tatsuma, T. Enhancement of Dye-Sensitized Photocurrents by Gold Nanoparticles: Effects of Plasmon Coupling. *J. Phys. Chem. C* **117**, 5901–5907 (2013).

113. Sukharev, M. & Nitzan, A. Plasmon transmission through excitonic subwavelength gaps. *J. Chem. Phys.* **144**, 144703 (2016).

114. Brawley, Z. T., Bauman, S., Darweesh, A., Debu, D., Tork Ladani, F., & Herzog, J. Plasmonic Au Array SERS Substrate with Optimized Thin Film Oxide Substrate Layer. *Materials* **11**, 942 (2018).

115. Bauman, S. J., Brawley, Z. T., Darweesh, A. A. & Herzog, J. B. Substrate Oxide Layer Thickness Optimization for a Dual-Width Plasmonic Grating for Surface-Enhanced Raman Spectroscopy (SERS) Biosensor Applications. *Sensors* **17**, 1530 (2017).

116. Darweesh, A. A., Bauman, S. J., Debu, D. T. & Herzog, J. B. The Role of Rayleigh-Wood Anomalies and Surface Plasmons in Optical Enhancement for Nano-Gratings. *Nanomaterials* **8**, 809 (2018).

117. Darweesh, A. A., Bauman, S. J., Brawley, Z., Herzog, J. B. & Herzog, J. B. Dual-width Plasmonic Nanogap Gratings electrodes for GaAs Metal-Semiconductor-Metal Photodetectors Enhancement. in *Frontiers in Optics 2017 (2017), paper FM4A.3* FM4A.3 (Optical Society of America, 2017). doi:10.1364/FIO.2017.FM4A.3

118. Brawley, Z. T., Bauman, S., Abbey, G., Darweesh, A., Nusir, A., Manasreh, O., & Herzog, J. Modeling and optimization of Au-GaAs plasmonic nanoslit array structures for enhanced near-infrared photodetector applications. *J. Nanophotonics* **11**, 016017 (2017).

119. Debu, D. T., Ghosh, P. K., French, D. & Herzog, J. B. Surface plasmon damping effects due to Ti adhesion layer in individual gold nanodisks. *Opt. Mater. Express* **7**, 73–84 (2017).

120. Torrance, K. E. & Sparrow, E. M. Theory for Off-Specular Reflection From Roughened Surfaces*. *JOSA* **57**, 1105–1114 (1967).

121. Darweesh, A. A., Bauman, S. J., Herzog, J. B. Impact of Tapered Nano-Slits Grating on The Optical Enhancement of Photo-Sensing Devices. in *Conference on Lasers and Electro-Optics (2018), paper AF3M.4* AF3M.4 (Optical Society of America, 2018). doi:10.1364/CLEO_AT.2018.AF3M.4

122. Johnson, P. B. & Christy, R. W. Optical Constants of the Noble Metals. *Phys. Rev. B* **6**, 4370–4379 (1972).

123. Darweesh, A. A., Bauman, S., French, D., Nusir, A., Manasreh, O., & Herzog, J. Current Density Contribution to Plasmonic Enhancement Effects in Metal–Semiconductor–Metal Photodetectors. *J. Light. Technol.* **36**, 2430–2434 (2018).

124. Palik, E. Handbook of Optical Constants of Solids, 1st ed.; Academic Press: pp. 286–297, Orlando, FL, USA, 1985.

APPENDIX A:

DESCRIPTION OF RESEARCH FOR POPULAR PUBLICATION

Improving devices that can interact with light, such as solar cells, cameras, displays, computers, photodetectors and sensors, are a very vital step for the next generation of nano-technology. These devices contain nanomaterials that convert the interaction into optical or electrical signals; they play a main role to develop and protect our daily lives. By enhancing the above mentioned devices, new diseases can be prevented or diagnosed. In addition, these devices can reduce, detect, and facilitate a large number of problems that our planet is suffering. For example, pollution (soil, water, and air) is the main problem that people face nowadays; it can be treated by these devices. So, improving these types of devices can reduce the cost as well and make them widely available.

We have improved nanostructures that can be used to enhance the performance of several devices, such as plasmonic photovoltaics, bio-sensors, surface-enhanced Raman spectroscopy, and photodetectors. These nanostructures can enhance optical response of these devices by manipulating their size and surrounding media. Computer models were built and used to determine the optical response by changing the period of nanogratings (gap space and wire-widths).

Primarily, light can strongly interact with materials, especially metals (gold, silver etc.). This interaction makes the electrons of the metals fluctuate very rapidly. The fluctuated electrons can generate light, which in turn interacts with the incident light and produces so-called surface plasmon waves. This phenomenon can be utilized for light sensing and detection devices. Grating is one of the approaches used to generate this phenomenon; it is periodic metallic

structures built on different materials, such as semiconductors.

The results of this research showed that the gap space with dual-width structures (different wire-widths) of the period can enhance the efficiency of plasmonic devices. Smaller gap space can strength metal-light interaction. Experimentally, our lab was capable of fabricating a very small gap space (8 nm) by using a specific technique called nano-masking. Plus, an incident wave angle and a taper sidewall angle of the nanostructures can significantly increase the efficiency of these devices. A huge effort is still dedicated to plasmonically developing and enhancing light sensing devices due to their importance in industry, agriculture, and medicine.

APPENDIX B:

EXECUTIVE SUMMARY OF NEWLY CREATED INTELLECTUAL PROPERTY

Two points that should be considered as new intellectual property items during this research work.

1. Dual-width plasmonic nanograting and grid structures.
2. The use of engineered nanograting structures for optimized metal-semiconductor-metal at specific incident wavelengths.

APPENDIX C:

POTENTIAL PATENT AND COMMERCIALIZATION ASPECTS OF LISTED INTELLECTUAL PROPERTY ITEMS

The potential likelihood of receiving a patent and having commercial value for this work are discussed.

C.1 Patentability of Intellectual Property (Could Each Item be Patented)

Two items were considered for patenting:

1. One of the two key results of this research is the dual-width structures. Since the theoretical results showed the importance of these structures for nanograting applications, these novel structures could be fabricated, using nano-masking technique and pursued as patentable technology.
2. The same could be stated for the combination between the single wavelength detection technique and the optimized metal-semiconductor-metal photodetectors. In addition, the unique results showed that a smaller period (gap space and wire-width) of the nanograting could significantly increase the efficiency of the photodetection.

C.2 Commercialization Prospects (Should Each Item Be Patented)

This dissertation focuses on the simulation method to obtain the results. It has used a novel method to determine the calculations numerically.

Two items listed were considered to be/or not patented.

1. The theoretical results show that novel dual-width structures can produce more enhancement compared with single-width structures. Therefore, the novel structures should be patented for potential commercial applications.
2. The theoretical results show that the combination of the single wavelength detection technique and the optimized metal-semiconductor-metal photodetectors with a small period (gap space and wire-width) can produce more enhancement as well. Therefore, this combination should be patented for potential commercial applications.

C.3 Possible Prior Disclosure of IP

No intellectual property from this work can now be patented. It has been publicly discussed in several journal articles, conference proceeding articles, and public presentations. The novelty of dual-width structures and single wavelength detection technique for metal-semiconductor-metal photodetectors were discussed. These journal and proceedings articles were published more than one year ago so no patents can be filed. Appendix G contains a list of the publications

APPENDIX D:

BROADER IMPACT OF RESEARCH

D.1 Applicability of Research Methods to Other Problems

The obtained results can be utilized not only to enhance metal-semiconductor-metal photodetectors, but also to improve other applications, such as solar cells, biosensors, surface enhanced Raman spectroscopy (SERS), and other photo sensing devices. For example, a huge amount of investment and effort are dedicated to enhance solar cells. Surface plasmons can play a central role to improve the performance and increase the efficiency of these devices and reduce the cost as well. In addition, developing surface enhanced Raman spectroscopy technique could make a breakthrough in biosensing devices. The results could serve optoelectronic devices, thermoplasmonic heating devices, and new display technology and applications.

D.2 Impact of Research Results on U.S. and Global Society

Much potential impact on U.S. and global society can be realized from this work. Enhancing light by nanostructures can benefit biosensors, solar cells, communication systems, and optical computers and systems. In addition, enhancing optical sensing devices can benefit medical diagnostics, forensics, weapon and car bomb detection, food safety, squandered energy, biomedical imaging, security, military applications, environmental monitoring and etc.

D.3 Impact of Research Results on the Environment

Since the majority of this research is modeling and simulation, the results of this work

will not affect the environment. Furthermore, using the simulations can predict the optimized nanostructures, which in turn reduce the number of experiments that can be conducted in the lab.

To illustrate, the results can benefit not only the photodetector applications, but also solar cells. The solar cells can be plasmoniclly enhanced by utilizing metallic nanostructures to boost the efficiency of the cells and to reduce the cost as well. In addition, enhancing the efficiency of solar cells can reduce the pollution of power plants; hence, the solar cells would be a great choice to generate electricity as an alternative renewable energy source.

APPENDIX E:

MICROSOFT PROJECT FOR PHD MICROEP DEGREE PLAN

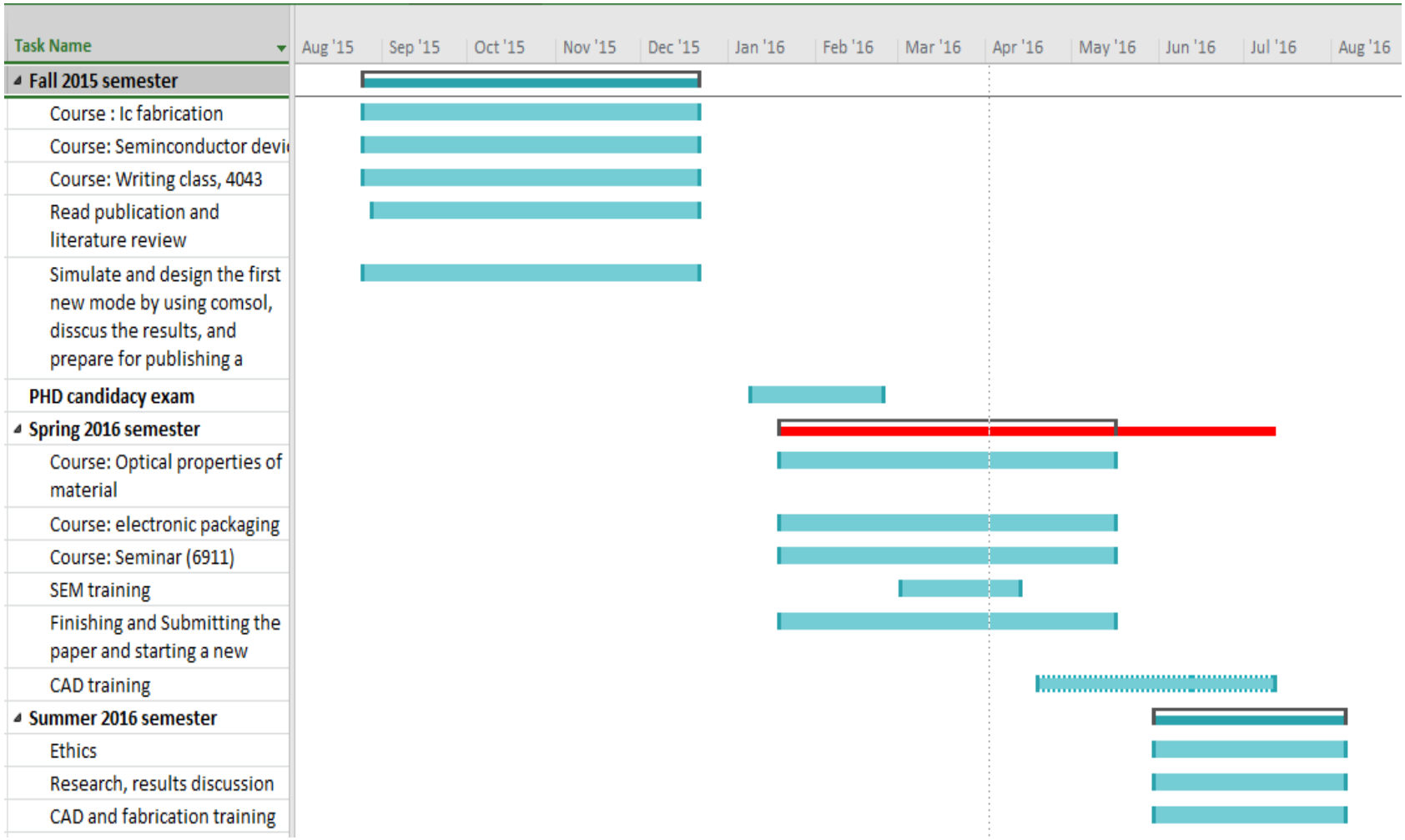
Task Name
Aug '15
Sep '15
Oct '15
Nov '15
Dec '15
Jan '16
Feb '16
Mar '16
Apr '16
May '16
Jun '16
Jul '16
Aug '16
Fall 2015 semester
Course : Ic fabrication
Course: Seminconductor devi
Course: Writing class, 4043
Read publication and literature review
Simulate and design the first new mode by using comsol, disscus the results, and prepare for publishing a
PHD candidacy exam
Spring 2016 semester
Course: Optical properties of material
Course: electronic packaging
Course: Seminar (6911)
SEM training
Finishing and Submitting the paper and starting a new
CAD training
Summer 2016 semester
Ethics
Research, results discussion
CAD and fabrication training

Task Name	Duration
Fall 2016 semester	**86 days**
Orginize the results and prepare to submit the second	85 days
Course: 1	85 days
Course: management and leadership	85 days
CAD and fabrication training	85 days
Spie conference attending(San Diego)	6 days
PHD research proposal exam	64 days
Spring 2017 semester	**85 days**
Course: EMERGING TECHNOLOGIES	85 days
Course: 2	85 days
Simulation and fabrication research	85 days
Summer 2017 course	**50 days**
Organize the results for Preparing to new papers	50 days

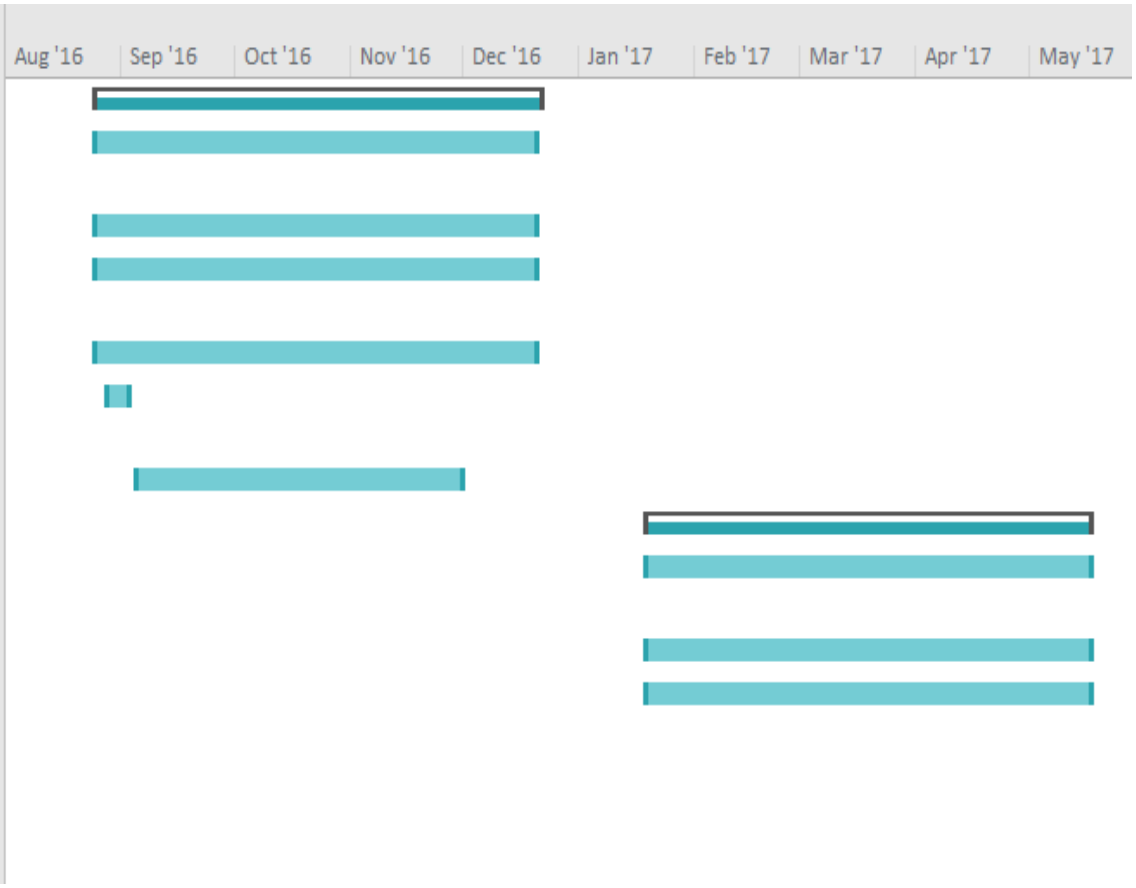

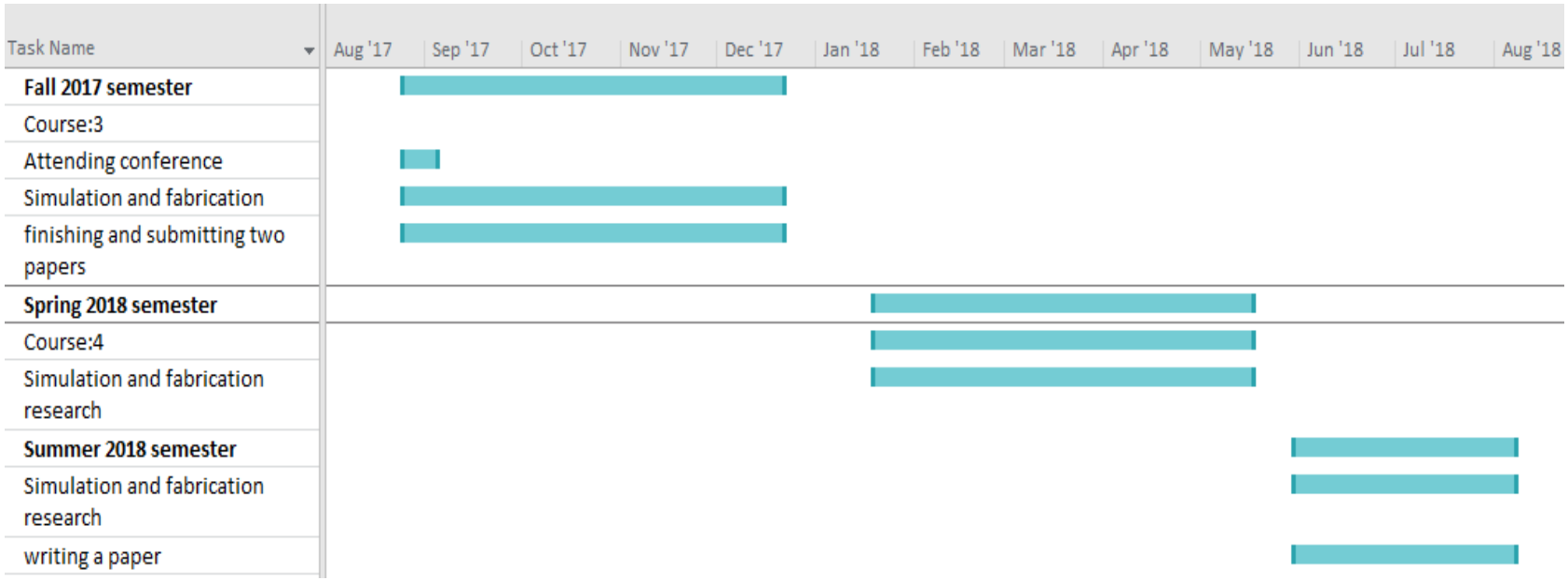
Task Name
Aug '17
Sep '17
Oct '17
Nov '17
Dec '17
Jan '18
Feb '18
Mar '18
Apr '18
May '18
Jun '18
Jul '18
Aug '18
Fall 2017 semester
Course:3
Attending conference
Simulation and fabrication
finishing and submitting two papers
Spring 2018 semester
Course:4
Simulation and fabrication research
Summer 2018 semester
Simulation and fabrication research
writing a paper

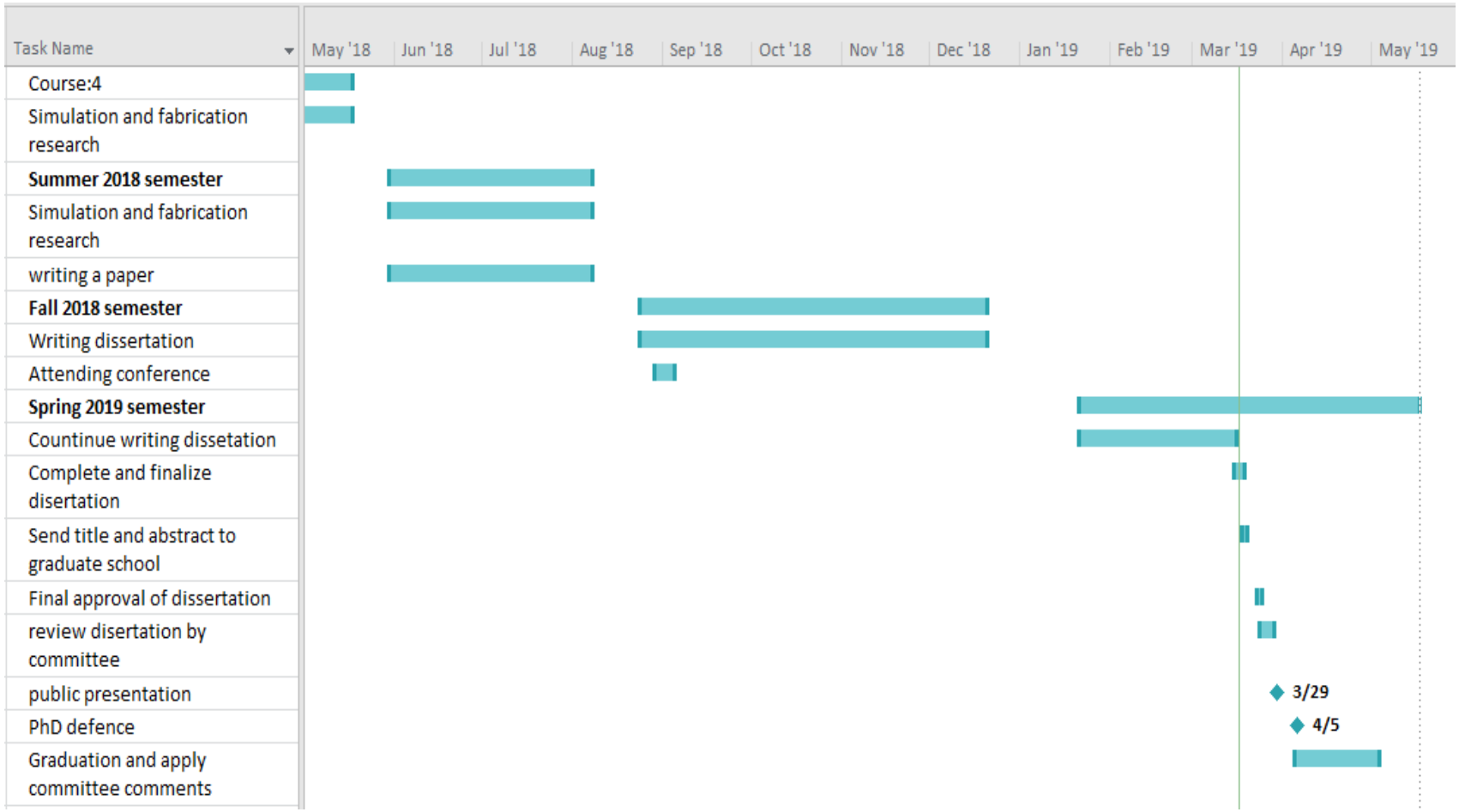
Task Name
May '18
Jun '18
Jul '18
Aug '18
Sep '18
Oct '18
Nov '18
Dec '18
Jan '19
Feb '19
Mar '19
Apr '19
May '19
Course:4
Simulation and fabrication research
Summer 2018 semester
Simulation and fabrication research
writing a paper
Fall 2018 semester
Writing dissertation
Attending conference
Spring 2019 semester
Countinue writing dissetation
Complete and finalize disertation
Send title and abstract to graduate school
Final approval of dissertation
review disertation by committee
public presentation
PhD defence
Graduation and apply committee comments
3/29
4/5

APPENDIX F:

IDENTIFICATION OF ALL SOFTWARE USED IN RESEARCH AND DISSERTATION GENERATION

Computer #1:

Model Number: Surface Pro 4 DESKTOP-8GPSS7K
Serial Number: 074405160453
Location: N/A
Owner: Ahmad Darweesh

Software #1:

Name: Microsoft Office 2013
Owner: University of Arkansas Fulbright College of Arts and Sciences

Software #2:

Name: Nanopattern Generation System (NPGS) v9 Office Installation
Owner: University of Arkansas Institute for Nanoscience and Engineering

Software #3:

Name: DesignCAD 2000LT with NPGS
Owner: University of Arkansas Institute for Nanoscience and Engineering

Software #4:

Name: Adobe Reader XI v11.0.01
Owner: Ahmad Darweesh (freeware)

Software #5:

Name: Zotero 4.0.21.2
Owner: Ahmad Darweesh (freeware)

Software #6:

Name: Skype
Owner: Ahmad Darweesh (freeware)

Software #7:

Name: TeamViewer 11
Owner: Ahmad Darweesh (freeware)

Computer #2:

Model Number: ASUS Essentio Series X18-82071
Serial Number: 150290C00700
Location: PHYS 106

Owner: Herzog Lab

Software #1:
Name: COMSOL Multiphysics
Owner: Herzog Lab (individual computer license)

Software #2:
Name: COMSOL Multiphysics
Owner: University of Arkansas Microelectronics-Photonics Graduate Program

Software #3:
Name: Nanopattern Generation System (NPGS) v9 Office Installation
Owner: University of Arkansas Institute for Nanoscience and Engineering

Software #4:
Name: DesignCAD 2000LT with NPGS
Owner: University of Arkansas Institute for Nanoscience and Engineering

Software #5:
Name: Microsoft Office 2013
Owner: University of Arkansas Fulbright College of Arts and Sciences

Software #6:
Name: MATLAB R2014a (Version 8.3)
Owner: University of Arkansas Department of Physics

Computer #3:
Model Number: N/A (Custom built)
Serial Number: N/A (Custom built)
Location: PHYS 106
Owner: Herzog Lab

Software #1:
Name: COMSOL Multiphysics
Owner: Herzog Lab (individual computer license)

Software #2:
Name: COMSOL Multiphysics
Owner: University of Arkansas Microelectronics-Photonics Graduate Program

Software #3:
Name: Nanopattern Generation System (NPGS) v9 Office Installation
Owner: University of Arkansas Institute for Nanoscience and Engineering

Software #4:
Name: DesignCAD 2000LT with NPGS

Owner: University of Arkansas Institute for Nanoscience and Engineering

Software #5:
Name: Microsoft Office 2013
Owner: University of Arkansas Fulbright College of Arts and Sciences

Software #6:
Name: MATLAB R2014a (Version 8.3)
Owner: University of Arkansas Department of Physics

Computer #4:
Model Number: Dell 3615KL – 04W – B86
Serial Number: 8XRZL51
Location: Nano Room 125
Owner: University of Arkansas Institute for Nanoscience and Engineering

Software #1:
Name: Nanopattern Generation System (NPGS) v9 Microscope Installation
Owner: University of Arkansas Institute for Nanoscience and Engineering

Software #2:
Name: DesignCAD 2000LT with NPGS
Owner: University of Arkansas Institute for Nanoscience and Engineering

Computer #5: Accessed University of Arkansas VLab General Access Computing Lab
Model Number: N/A
Serial Number: N/A
Location: VLab General Access Computing Lab
Owner University of Arkansas IT Services

Software #1:
Name: Adobe Photoshop v?
Owner: University of Arkansas IT Services

Computer #6:
Model Number: Dell Precision T5610
Serial Number: BJKQM02
Location: N/A
Owner: Herzog Lab

Software #1:
Name: Microsoft Office 2016
Owner: University of Arkansas Fulbright College of Arts and Sciences

Software #2:

Name: TeamViewer 13
Owner: Herzog Lab (freeware)

Software #3:
Name: Skype
Owner: Herzog Lab (freeware)

Software #4:
Name: MATLAB 2018a
Owner: Ahmad Darweesh (purchased student license)

Software #5:
Name: COMSOL Multiphysics 5.3a
Owner: Herzog Lab (purchased individual computer license)

Computer #7:
Model Number: HP OMEN 870-224
Serial Number: 4CE709190Q
Location: PHYS 106
Owner: Herzog Lab

Software #1:
Name: LightField version 5 (Princeton Instruments)
Owner: Herzog Lab

Software #2:
Name: AmScope camera software
Owner: Herzog Lab

Software #3:
Name: Arduino GUI
Owner: Herzog Lab (freeware)

Software #4:
Name: DesignCAD 2000LT with NPGS
Owner: University of Arkansas Institute for Nanoscience and Engineering

Software #5:
Name: Microsoft Office 2016
Owner: University of Arkansas Fulbright College of Arts and Sciences

Software #6:
Name: MATLAB R2014a (Version 8.3)
Owner: University of Arkansas Department of Physics

APPENDIX G:

ALL PUBLICATIONS PUBLISHED, SUBMITTED, AND PLANNED

JOURNAL ARTICLES:

- **A. A. Darweesh**, S. J. Bauman, D. T. Debu, J. B. Herzog, "The Role of Rayleigh-Wood Anomalies and Surface Plasmons in Optical Enhancement for Nano-Gratings", 8 (10), 809, Nanomaterials, (2018).
- C. M. Klenke, Z. T. Brawley, S. J. Bauman, **A. A. Darweesh**, D. T. Debu, J. B. Herzog, "Dataset for SERS Plasmonic Array: Width, Spacing, and Thin Film Oxide Thickness Optimization", 3 (3), 37, Data, (2018).
- Z. T. Brawley, S. J. Bauman, **A. A. Darweesh**, D. T. Debu, F. Tork Ladani, J. B. Herzog, "Plasmonic Au Array SERS Substrate with Optimized Thin Film Oxide Substrate Layer", 11 (6), 942, Materials, (2018).
- **A. A. Darweesh**, S. J. Bauman, D. French, A. Nusir, O. Manasreh, J. B. Herzog, "Current Density Contribution to Plasmonic Enhancement Effects in Metal-Semiconductor-Metal Photodetectors", 36 (12), 2430-2434, Journal of Lightwave Technology, (2018).
- S. J. Bauman, **A. A. Darweesh**, D. T. Debu, J. B. Herzog, "Fabrication and Analysis of Metallic Nanoslit Structures: Advancements in the Nanomasking Method", 17 (1), 013501, JM3 (2018).
- S. J. Bauman, Z. T. Brawley, **A. A. Darweesh**, J. B. Herzog, "Substrate Oxide Layer Thickness Optimization for a Dual-Width Plasmonic Grating for Surface-Enhanced Raman Spectroscopy (SERS) Biosensor Applications", 17 (7), 1530, Sensors, (2017).
- Z. T. Brawley, S. J. Bauman, G. P. Abbey†, **A. A. Darweesh**, A. I. Nusir, O. Manasreh, and J. B. Herzog, "Modeling and optimization of Au-GaAs plasmonic nanoslit array structures for enhanced near-infrared photodetector applications", 11 (1), 016017, Journal of Nanophotonics, (2017).
- **A. A. Darweesh**, S. J. Bauman, and J. B. Herzog, "Improved optical enhancement using double-width plasmonic gratings with nanogaps", 4 (5), 173-180, Photonics Research, (2016).

CONFERENCE PUBLICATIONS:

- **A. A. Darweesh**, S. J. Bauman, D. Debu, J.B. Herzog. "Investigating Rayleigh-Wood anomalies and surface plasmon resonances in optical and electrical enhancements for nano-grating structures and devices," *Bulletin of the American Physical Society, APS March Meeting 2019*, (March 2019)

- **A. A. Darweesh**, S. J. Bauman, J. B. Herzog, "Impact of Tapered Nano-Slits Grating on The Optical Enhancement of Photo-Sensing Devices", CLEO: Applications and Technology, AF3M. 4 (2018).
- **A. A. Darweesh**, S. J. Bauman, Z. Brawley, J. B. Herzog, "Dual-width Plasmonic Nanogap Gratings electrodes for GaAs Metal-Semiconductor-Metal Photodetectors Enhancement", Frontiers in Optics, FM4A 3 (2017).
- **A. A. Darweesh**, S. J. Bauman, Z. T. Brawley, J. B. Herzog, "Improved optical enhancement in binary plasmonic gratings with nanogap spacing", Proc. SPIE 9927 0Z, (2016).
- S. J. Bauman, **A. Darweesh**, J. B. Herzog, "Dual-width plasmonic gratings with sub-10 nm gaps for biosensor applications", Proc. SPIE 9927 09, (2016).
- D. A. French, S. J. Bauman, **A. Darweesh**, D. Debu, P. K. Ghosh, J. B. Herzog, "Plasmonic resonance shift for various nanodevice geometries", Proc. SPIE 9836 2X, (2016).
- S. J. Bauman, **A. A. Darweesh**, J. B. Herzog, "Surface-enhanced Raman spectroscopy substrate fabricated via nanomasking technique for biological sensor applications", Proc. SPIE 9759 1I, (2016).

In Preparation & Planned:

- **Ahmad A. Darweesh**, Stephen J. Bauman, Desalegn T. Debu, Meredith Magee, Miles H. Furr, and Joseph B. Herzog, “Taper and incident wave angles effects on plasmonic metal-semiconductor-metal photodetector enhancements” Journal of the Optical Society of America B (submitted March, 2019).
- S. J. Bauman, **A. Darweesh**, D. Debu, and J. B. Herzog, “Engineering large-area plasmonic enhancement via nanogap grid structures” (In preparation)
- D. Debu, **A. Darweesh**, and J. B. Herzog, “Broad optical range near field Raman enhancement from plasmonic heterodimer particle” (In preparation)

APPENDIX H:

COMSOL GUIDE AND DIRECTIONS

- Creating a new physics interface

Here is the basic modeling workflow in COMSOL Multiphysics. To set up and solve a simulation, it requires a standard single workflow. This means that the simulation steps of building a model from scratch are independent of the type of the problem that is considered. In other words, these simulation steps can be used to design and build the desired model and no matter the type of problem that the designers are trying to solve. These steps are: setting up the model environment, creating the geometric objects, specifying the material properties, defining physics boundary conditions, creating the mesh, running the simulation, and post-processing the final results. It is too difficult to explain everything in the COMSOL Multiphysics software, but the dissertation includes only the commands that were used to conduct and run the models of this work. The entire results, for example, in this dissertation came from 2D models, so it is unexpected to include 3D model design procedure.

When the COMSOL software is opened, two options for setting up the desired model will appear in a new window, one of which can be used to create a new model, Figure H.1 (a). The first option is called “model wizard”. In this option, one can specify and include the spatial dimension physics and the desired studies. The second option is called the “blank model”. In this option, one can start and build a new empty model and then determine the desired studies. In this dissertation, the first option was utilized to design the model and conduct the results. After selecting the model wizard option, a new window that is called “Select Space Dimension” will appear. In this window, one space dimension of different types should be taken to determine the

type of the space that will be used in the model.

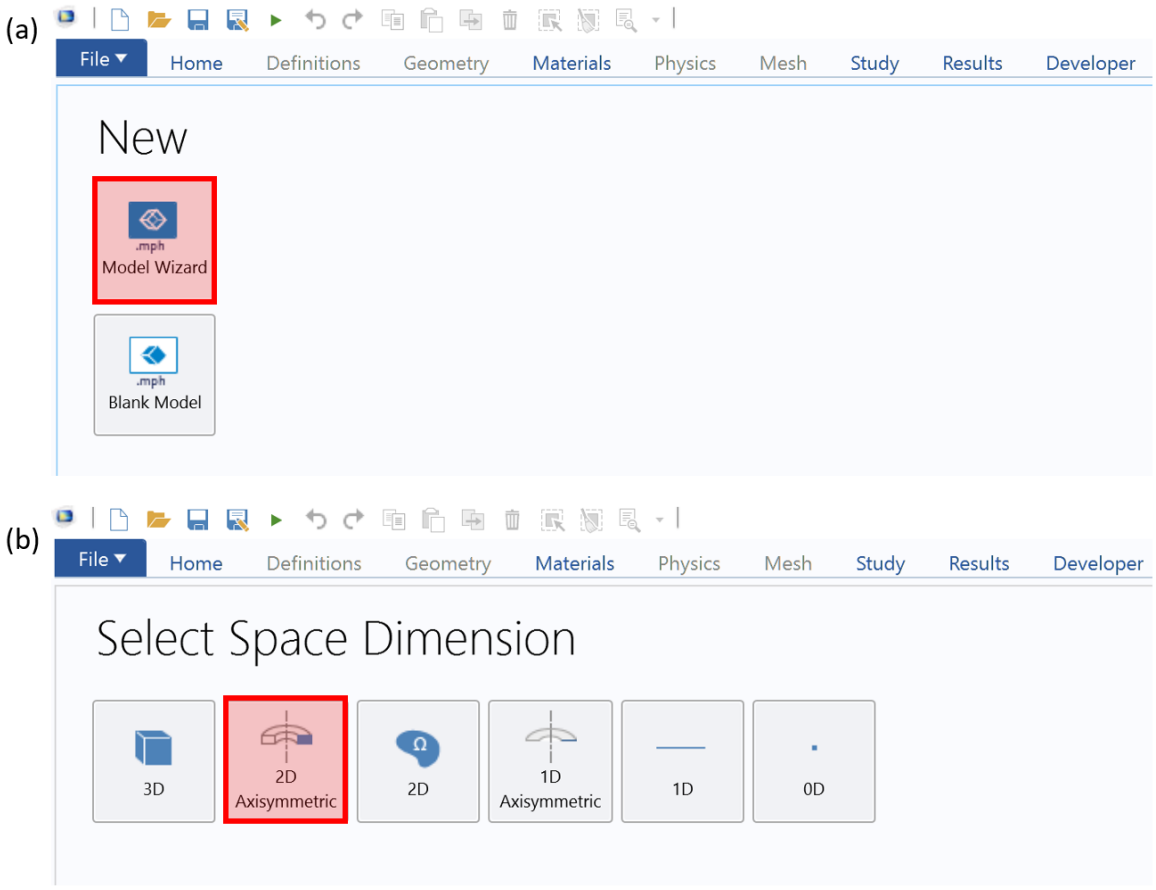

Figure H.1. First two options of creating a new model.

For example, there are 3D, 2D axisymmetric, 2D, 1D axisymmetric, 1D, and 0D dimensions. The space dimension in this dissertation work was 2D axisymmetric, Figure H.1 (b). After selecting 2D axisymmetric, a new window with several types of physics appears. This window helps out the user to select the desired physics that should be included in the simulation. It is possible to add more than one physics and create any combination of physics. In this dissertation, for example, two physics, AC/DC and Radio Frequency, were selected to obtain the final results. Under the AC/DC module, there are a bunch of interfaces such as Electric current (shell), Electrostatic, and Electrical Circuit. Electric Current interface was used in this work

because the desired calculations include the current distribution of the proposed device.

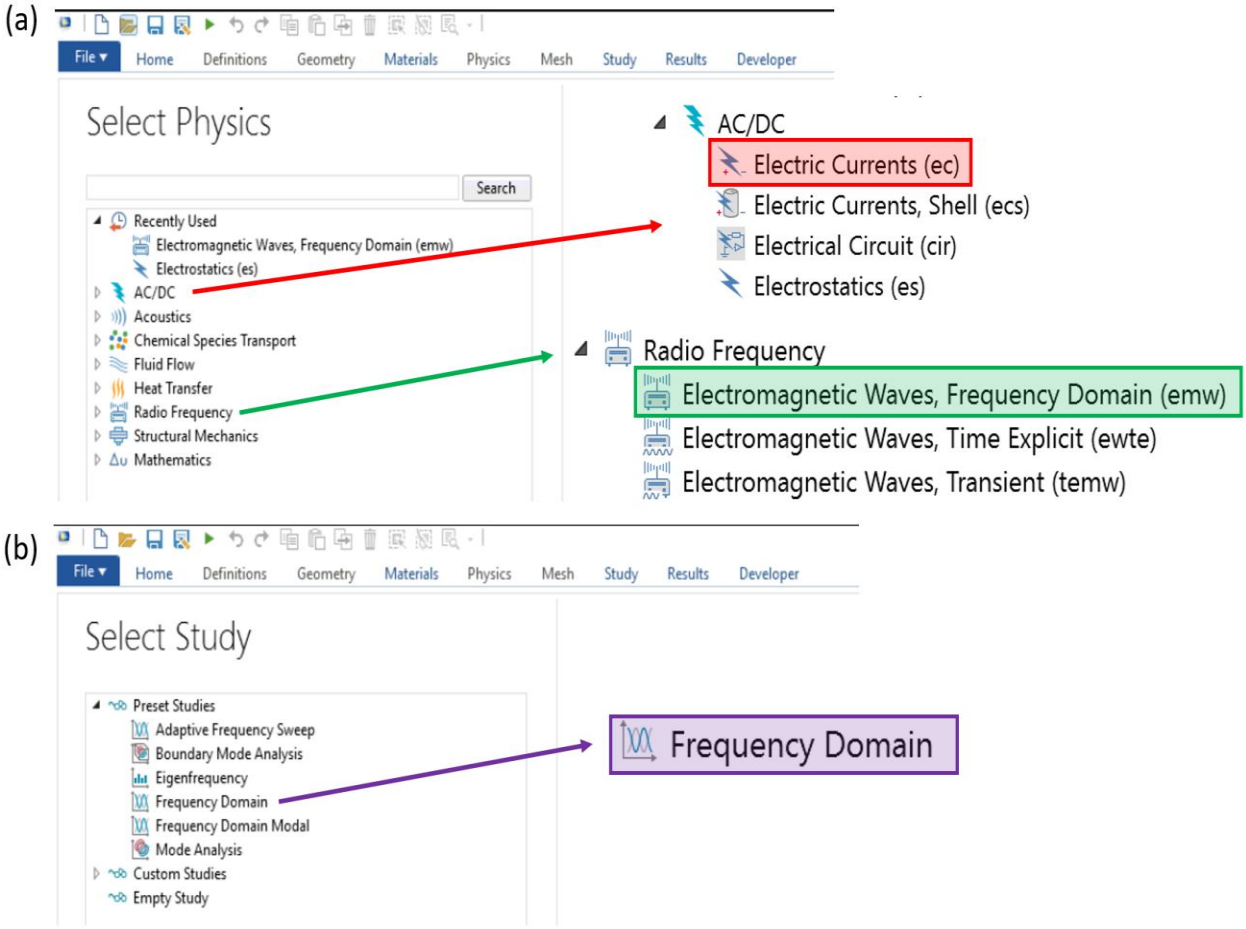

Figure H.2. Select physics and study windows.

Under the Radio Frequency module, on the other hand, several interfaces can be used for different applications; however, the Electromagnetic Wave, Frequency Domain interface was used to conduct the work, Figure H.2 (a). After choosing the space dimension and the physics, the next step is selecting the “Study” from the “Select study” window. Based on the selected physics, the study can be determined. From the “Select Study” window, Figure H.2 (b), “Frequency Domain” was conducted to be in the simulation because this study can be used to compute the response of a linear model subjected to harmonic excitation for one frequency or more.

- Controlling the structure geometry

Figure H.3 shows the COMSOL desktop, which can be divided into five main windows.

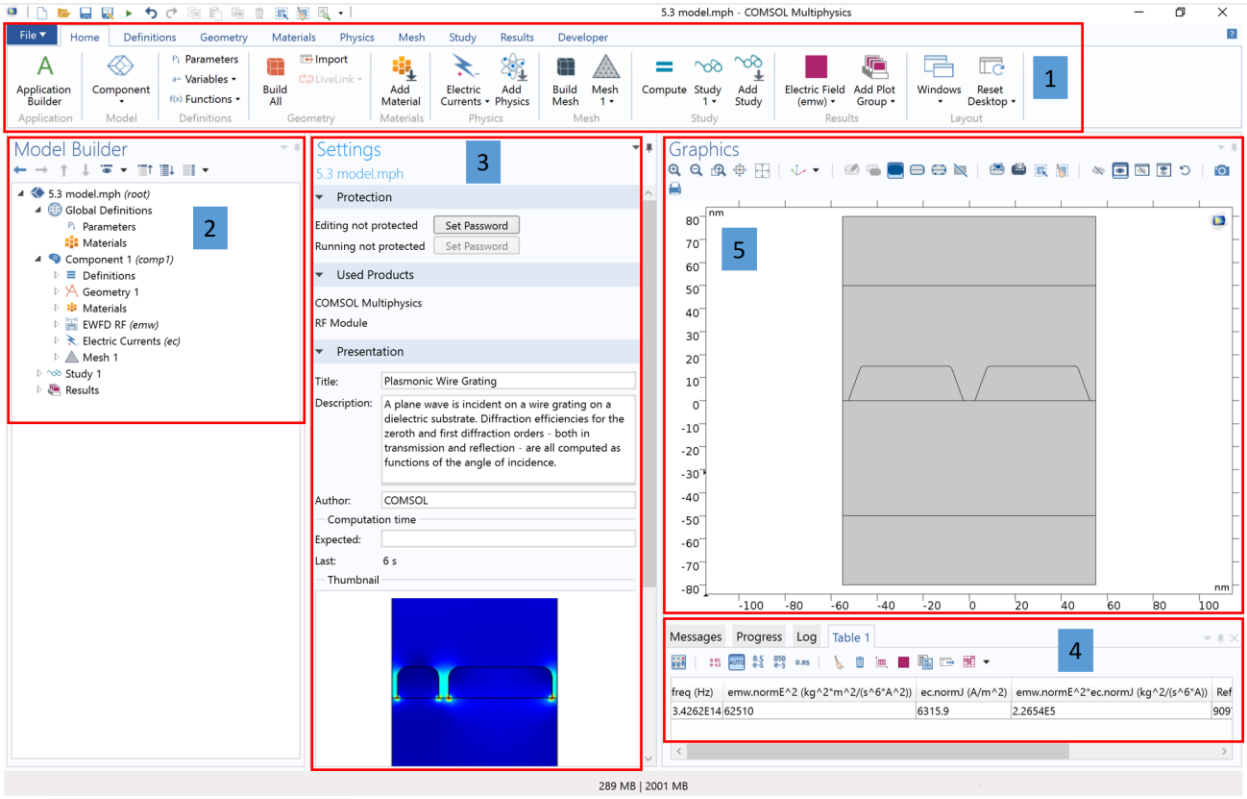

Figure H.3. COMSOL Multiphysics desktop.

Window 1 is called the “ribbon bar”. This window contains the steps to complete the desired model, which are called “model tree”, such as definitions, geometry, materials, mesh, study, and results. Window 2 is called the “Model Builder” window that houses the same options in window 1, Figure H.4 However, reaching the commands from this window will be faster and easier. Window 3 is called the “Setting” window. This window provides different options that can ease the model steps. The next one is called the “message progress log” window. This window shows the progress of the model during the run and gives some output results such as data tables. The last window is called the “Graphics” window. The output can be presented as

plots or maps in this window. This dissertation work follows the logic sequence of the workflow steps that appear in the Model Builder window, Figure H.4 Now, the first step to build any model is defining any constants, parameters, variables or functions that are used as initial values to run the model. Figure H.5 shows the parameters setting window that contains some constants, variables and functions.

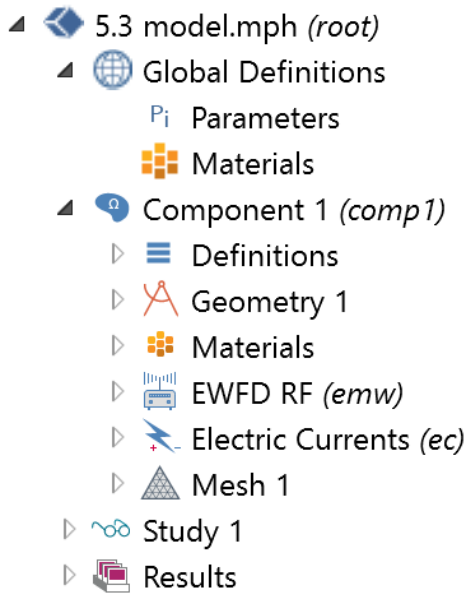

Figure H.4. Model builder window.

Two main options can be used to create the desired geometry. First, the COMSOL Multiphysics drawing tools or operations that are located in the ribbon bar. Second, the external geometry files that were designed in AutoCAD and other software and can be imported into COMSOL. However, the models that were used in this work were designed by the COMSOL tools. COMSOL Multiphysics contains a huge number of tools that can be used to create a 2D geometry for the desired model; it contains several common built-in primitive geometry objects, such as circles, ellipses, rectangles and polygons, Figure H.6 (a). By hitting the right click of the mouse on the Geometry icon, a long list of options that include the geometry objects will appear.

All these shapes or objects can be modified by the “Setting” window that allows the user or the builder to control the dimensions and positioning of the objects.

Settings

Parameters

Parameters

Name	Expression	Value	Description
wirewidth1	50	50	left wire
wirewidth2	50	50	right wire
wirethickness	15	15	wire thickness
thetawall	20[deg]	0.34907 rad	wall angle
alpha	0[deg]	0 rad	Angle of incidence
gapspace	5	5	gap space
period	50	50	w1+w2+g
spaceheight	GaAsthickness	50	Air height
GaAsthickness	50	50	Substrate height
TopBoxHeight	wirethickness+25	40	Box arrond wires
spacewidth	wirewidth1+2*gapspace+wirewidth2	110	Model Width
BottomBoxHeight	40	40	Box under wires
X1	wirethickness*tan(thetawall)	5.4596	wire1 edge distance
X2	X1	5.4596	wire2 edge distance
lambda0	875[nm]	8.75E-7 m	Vacuum wavelength
B1	wirewidth1-2*X1	39.081	wire1 middle part
B2	wirewidth2-2*X2	39.081	wire2 middle part
Vb	5[V]	5 V	Bias voltage
junctiondepth	1	1	Model Depth (default 1 m)
k0	2*pi/lambda0	7.1808E6 1/m	incident wavenumber
Irradiance	0.5*8.85e-12[m^-3*kg^-1*s^4*A^2]*c_const*...	0.0013266 W/...	Power per unit area due...
KiGaAs	0.074	0.074	Refractive index, GaAs
nGaAs	3.645	3.645	Refractive index, GaAs
active_area	junctiondepth[m]*spacewidth[nm]	1.1E-7 m^2	Surface area in x/z plane
inputpower	Irradiance*active_area	1.4592E-10 W	Used in defining the fiel...
beta	asin(na*sin(alpha)/nGaAs)	0 rad	Refraction angle
f0	c_const/lambda0	3.4262E14 1/s	Frequency
w0	2*pi[rad]*f0	2.1527E15 rad/s	Radial Frequency of inci...
na	1	1	Refractive index, air
wirewidth2withperiod	period-wirewidth1-2*gapspace	-10	In case sweeping with pe...

Figure H.5. Parameters setting window.

In this dissertation, for example, the design that was used is shown in Figure H.6 (c). It consists of four rectangles: superstrate, substrate, PML top and PML down, a “Fillet” and two

polygons, W_1 and W_2, Figure H.6 (b). After hitting the "Build Selected" or "Build all Objects" bottom (Figure H.7), the desired shapes or objects will appear in the "Graphics" window, Figure H.6 (c). The purpose of using polygons as nanowires instead of rectangles is because their sidewalls are easy to control, which it is impossible to do in the case of rectangles. In addition, the Fillet is used to create rounded top edges of the polygons.

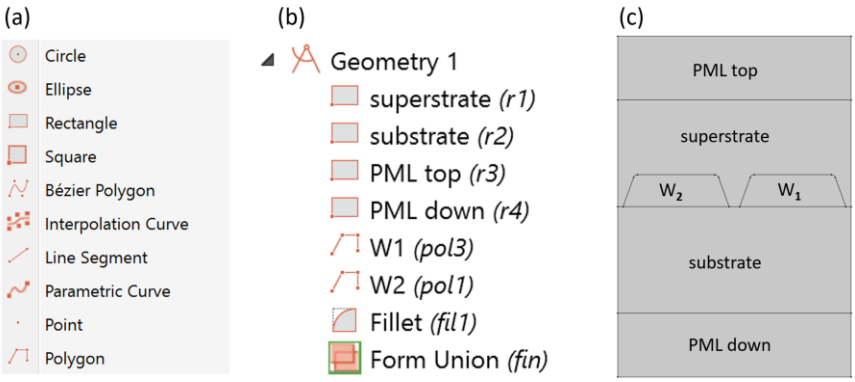

Figure H.6. Geometry shapes and structures in COMSOL.

An example of a rectangle "Setting" window is shown in Figure H.7.

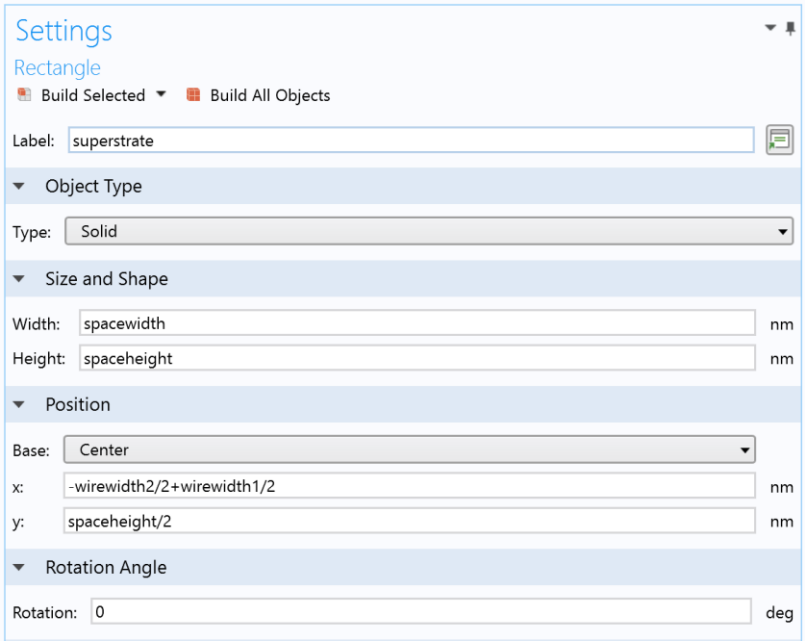

Figure H.7. Superstrate Setting window.

It shows the object type, width, height, position and rotation angle. It is possible to put the desired number directly in each slot or keep it variable in the slot and control it from the parameters window.

- Controlling the materials

After creating and designing the desired geometry model, the next step in the workflow is to specify the material properties. Two main sources of material properties can be used to conduct this step. The first source is called “built-in material”. In addition to the built-in material, COMSOL contains a huge material library that exceeds 2500 materials. The other source is called “Blank Material”.

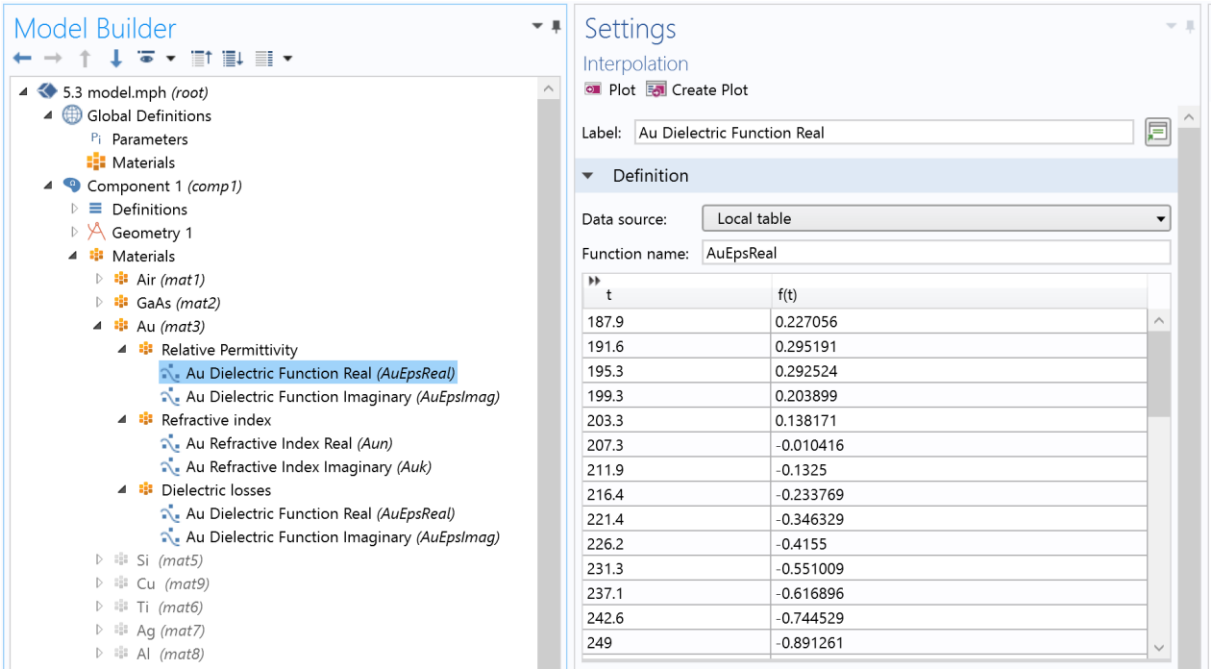

Figure H.8. Optical properties table of gold.

If someone needs a material that is not contained in the library, has different properties, or updated properties, one can create a specific material from scratch. In this dissertation work,

for example, data has been taken from experimental results and set up as new material properties. The Johnson and Christy handbook, which provides the optical properties of materials (frequency-dependent), is used to simulate the models in this work.[122,124] The optical properties can be defined as a function of a dielectric constant or refractive index (real and imaginary parts), Figure H.8. The optical properties in this work for a particular material were set up as interpolation tables. This technique allows simulating any value of incident light frequency within the experimental data range. Three materials: air, gallium arsenide (GaAs), and gold (Au) were used to run the models, Figure H.9. The figure in (a) shows some active (Air, GaAs, and Au) and inactive (Si, Cu, Ti …) materials. The figure in (b) shows the model structure with domain numbers and each domain and their corresponding materials. For example, domains 1 and 2 were defined as GaAs material in the simulation; domains 3 and 4 were air; domains 5 and 6 were gold. In addition, one can replace any materials in the list by deactivating unwanted materials and activing the desired ones.

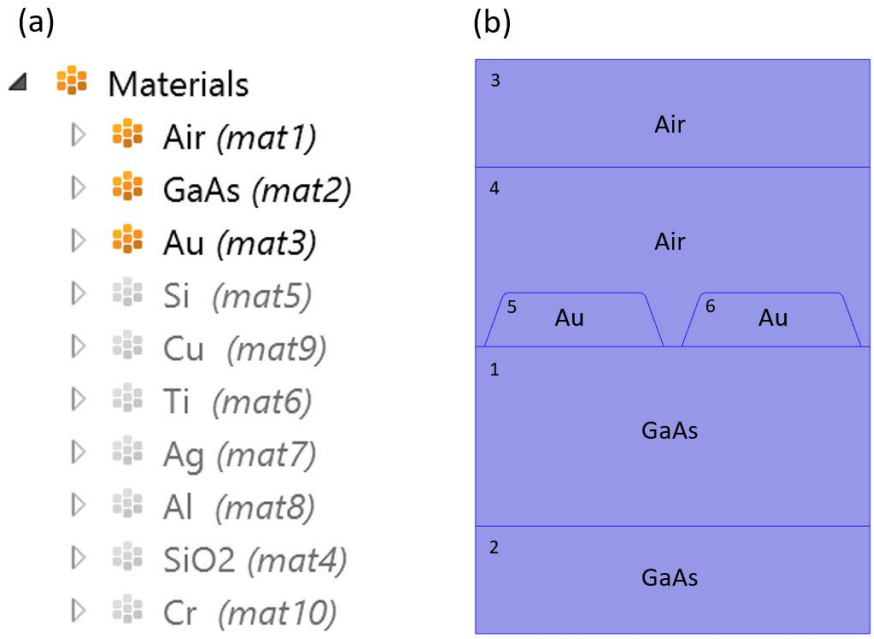

Figure H.9. “Materials” and structure domains.

- Controlling the physics interface

After specifying the materials, the next step is defining the physics of the 2D nanograting problem. This problem contains two configurations: physics for the Electromagnetic Wave Frequency Domain (EWFD), Figure H.10, and Electric Current, Figure H.11, interfaces.

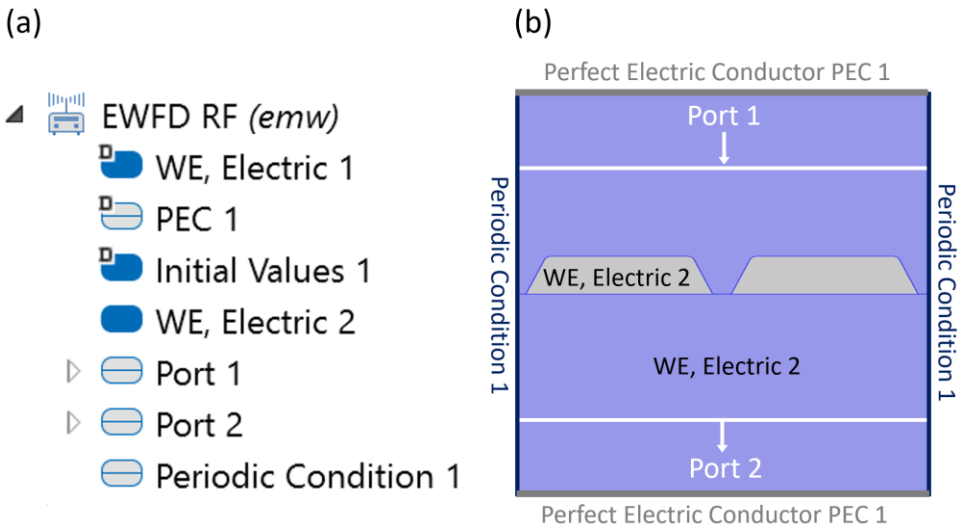

Figure H.10. Electromagnetic Wave Frequency Domain (EWFD) interface.

The Electromagnetic Wave Frequency Domain (EWFD) interface contains several nodes, listed in Figure H.10 (a), which were used to control the interface. Since the gold was used as a solid metal in the simulation, a wave equation node “WE, Electric 2” was created. This node governs the time-harmonic and eigenfrequency problems and the gold properties, such as the electric displacement field (as a function of relative permittivity), magnetic field and conduction current. However, the other wave equation node “WE, Electric 1” was created to govern the electric displacement field (as a function of refractive index) for the other materials (air and GaAs). At the very top of the air boundaries and very bottom of the GaAs boundaries, perfect electric conductor nodes “PEC 1” boundary conditions were set up to make the tangential component of the electric field equal to zero. The initial values node “Initial Values 1” was used

to add an initial value to the electric field. Two port nodes “Port 1 and Port 2” were set up on the top of the superstrate and the bottom of the substrate. These ports are used to calculate reflection, transmission, and absorption of the model. In addition, they are used to determine the positions of entering and exiting the electromagnetic energy in the model. The last node is called “Periodic Condition 1”. This node was set up on the left and right sides of the model to make an infinite horizontal array.

The second interface that was used in this dissertation is “Electric Currents”. This interface contains several nodes as well, two of which (Initial Values 1 and Periodic Condition 1) were explained in the EWFD interface, Figure H.11 (a).

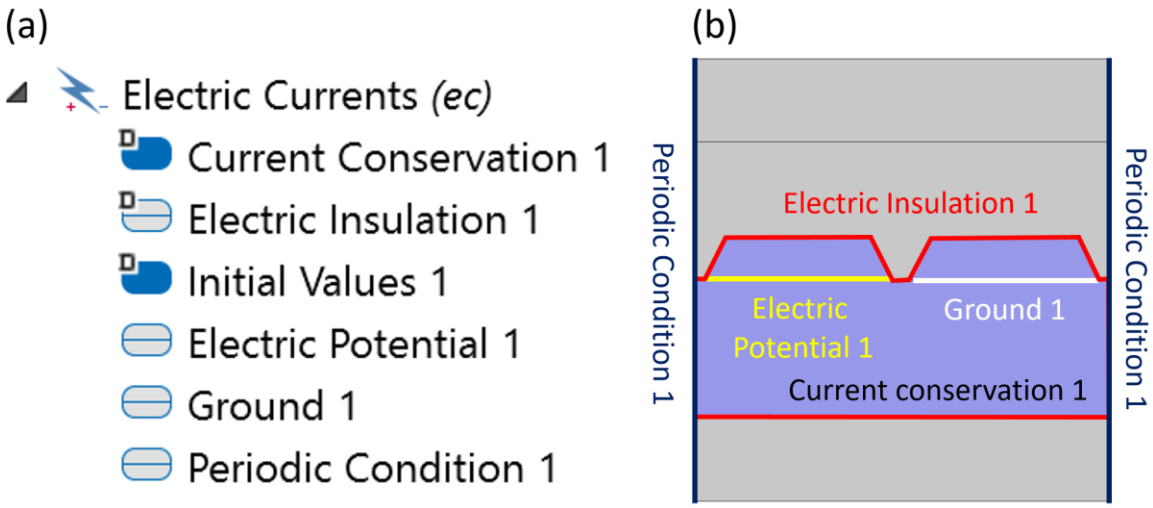

Figure H.11. Electric current interface.

However, the current conservation node was set up to govern the electrical potential and conductivity, the constitutive relation and the relative permittivity of the displacement current. The next node is called “Electric Insulation 1” that is used to add the electric insulation as a boundary condition, represented by the red line in Figure H.11 (b). This means no electric current will flow out of these boundaries. The last two nodes in the list of the electric current

nodes are “Electric Potential 1 and Ground 1”. Since the device contains applied potential difference, it is important to add electric potential as a boundary condition at one electrode. The “Ground 1” node provides zero potential on the other electrode as a boundary condition as well.

- Controlling the mesh

The next step in the workflow is the mesh, which is used to break up the model space into small sizes that serve as points of calculation. Since the proposed models in this work are 2D, four default types of mesh nodes: Free Triangular, Free Quad, Mapped and Boundary Layers, are contained in COMSOL. The usage of mesh node type depends on the structure surfaces. For example, if the model structure contains only straight parallel lines or surfaces such as squares and rectangles, it is preferred to use the Mapped mesh node. However, if the structure consists of circles or curved surfaces, it is preferred to use the Free Triangular or Free Quad mesh node, Figure H.12 (b).

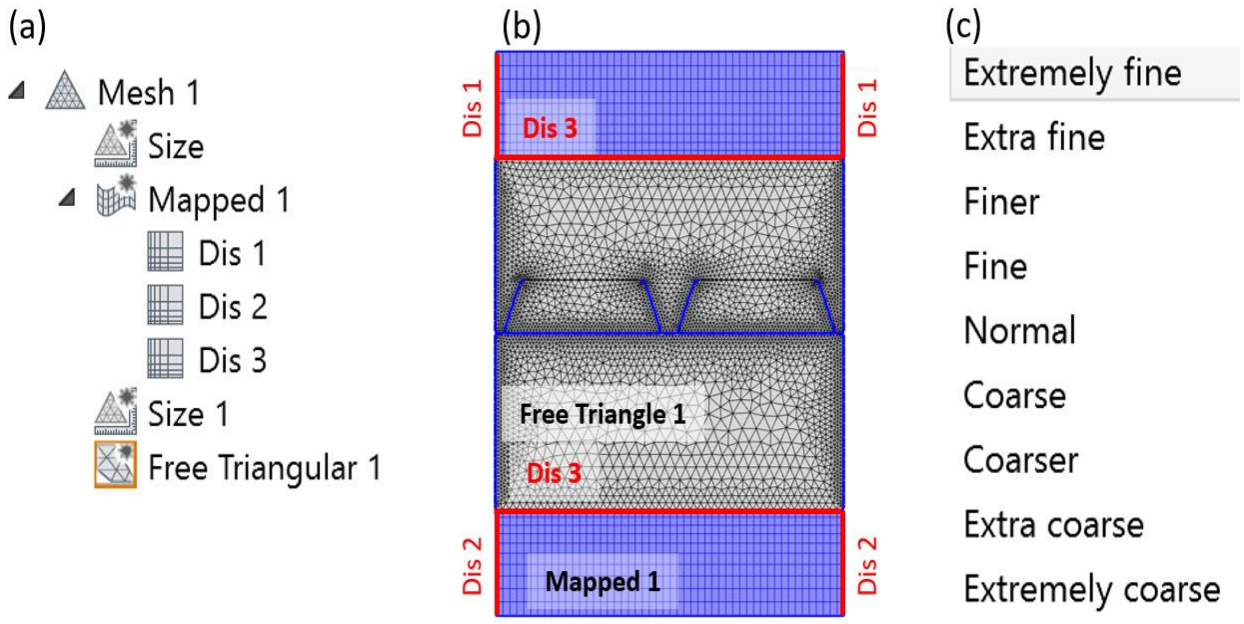

Figure H.12. Mesh map of the proposed model

This strategy helps the user to break up the curved surfaces neatly into many mesh points. As a result, a more precise calculation can be obtained. The mesh setting window allows the user to grow the mesh at a specific rate; it contains different default element sizes such as “Extremely fine, Finer, Normal and Coarser,” Figure H.12 (c). This feature allows the user to break up the interest or near curved surfaces into extremely fine mesh points and coarser mesh points at distances farther from the points of interest to reduce computation time. The other mesh node that used in this work is called distribution “Dis 1, 2 and 3”, Figure H.12 (a). This node is used to specify the number of mesh points along an edge.

- Controlling the study

Before running the simulation model file, the last step, which is called the “Study” node should be conducted. This node holds some other nodes such as study type and the solvers for dependent variables that define how to solve a model. This means the user can use this node to sweep a specific parameter or parameters. These parameters are added automatically in the “Parameter name” list when they are defined in the parameters table window, Figure H.5. For example, Figure H.13 (a) shows several parameters that were added by the user. “Alpha”, one of these parameters, is enabled or active and the others such as “wire width 1”, “Theta” and etc. are disabled. When the COMSOL file is run, it will solve the problem according to the variable “Alpha”. Figure H.13 (b) shows the setting window of the parametric sweep “Alpha”. The setting window includes parameter value list, which allows the user to set up the sweep from a minimum value to a maximum value with a step size. The unit of the parameter should be defined in the parameter section. It is possible to sweep one parameter or more at the same time. After running the file, the solutions are stored in the solver configurations.

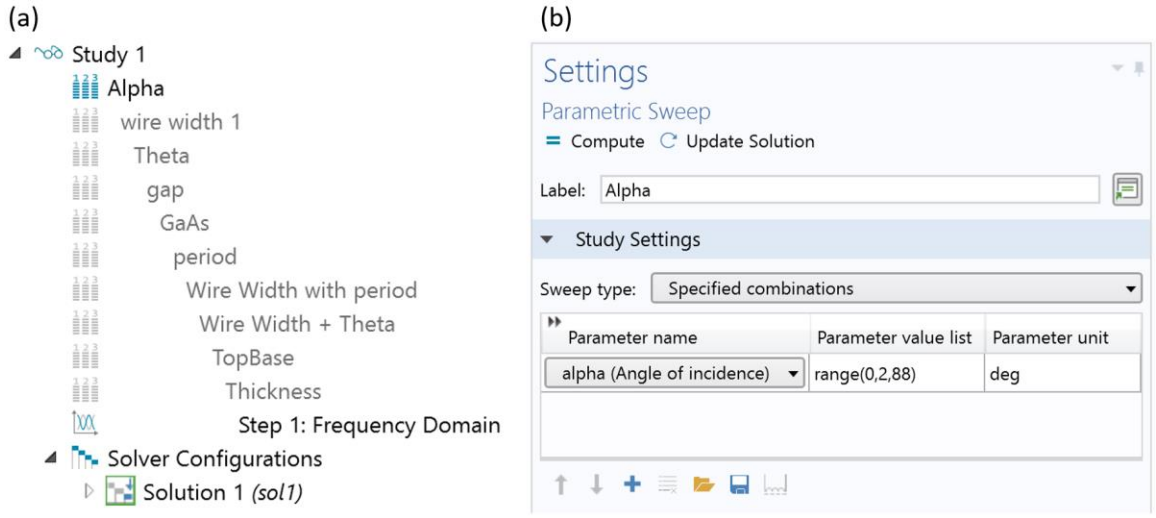

Figure H.13. Study node and parametric sweep setting windows.

- Controlling the results

After setting up all previous nodes, now one can run the simulation to obtain the results. All the previous nodes (definitions, geometry, materials, physics interfaces, mesh, and study) are considered as input data in COMSOL. However, the "Results" node represents the output data collection that results from the simulations in COMSOL. Different forms of output data can be represented in the "Results" node such as tables, color maps, and animations, Figure H.14 (a). A variety of plot configurations such as "3D Plot Group, 2D Plot Group, 1D Plot Group, Polar Plot Group, Smith Plot Group, GIF Movie, AVI Movie, and Flash Movie" are included in this node. In addition, the output data can be exported as a Text or Excel file. This technique has been used in this work to create 2D or 3D graphics via Excel or MATLAB. For example, Figure H.14 (b) shows a 2D color map of an electric field distribution. The "Results" node contains a so-called "Derived Values" section. In this section, the values of electric field and current density, for example, were integrated and computed by using the average, maximum, or minimum of the simulation results.

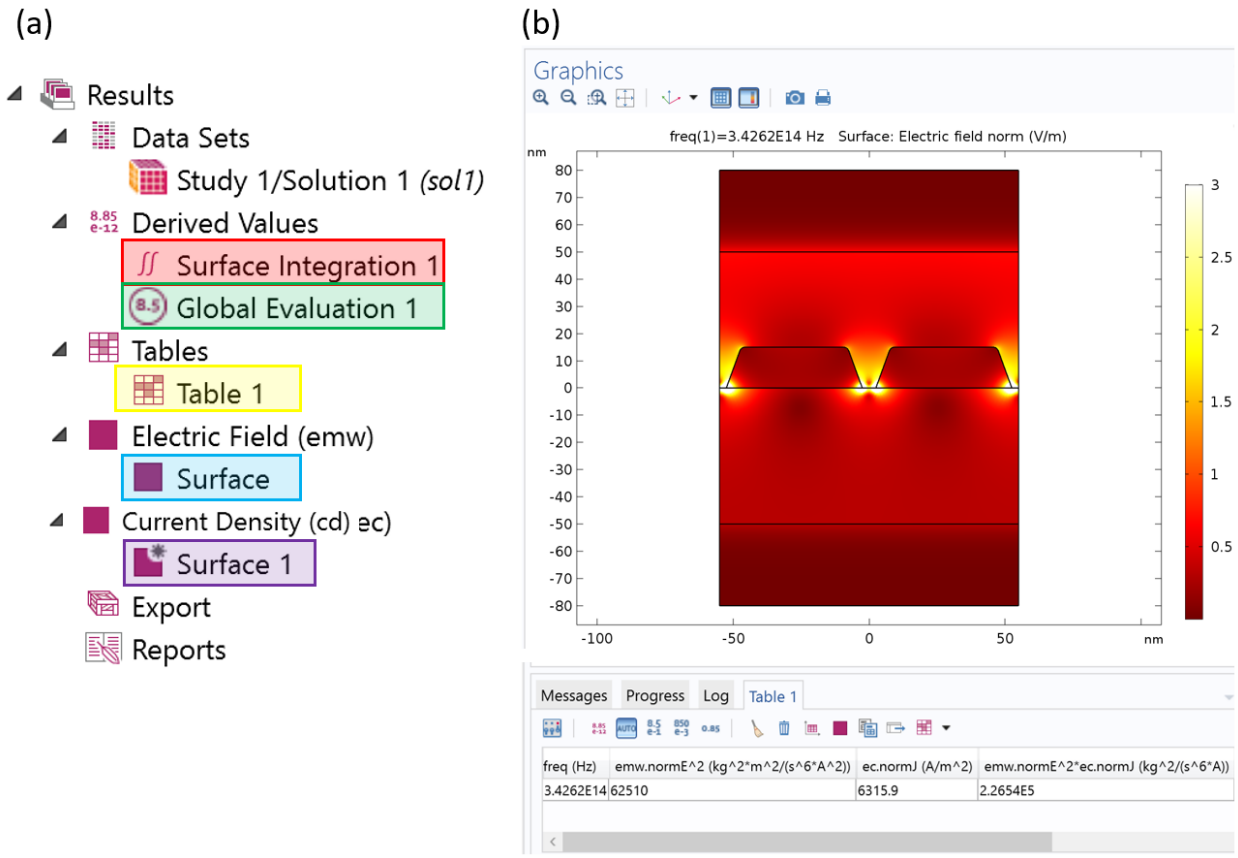

Figure H.14. Results node and the output color map.